STUDY OF PARTICLE RETENTION IN ULTRASONICALLY ENHANCED SEPARATION PROCESSES

by

MICHAEL TIMOTHY GROSSNER

Submitted in partial fulfillment

for the degree Doctor of Philosophy

Dissertation Advisor: Donald L. Feke

Department of Chemical Engineering

CASE WESTERN RESERVE UNIVERSITY

May, 2003

ProQuest Information and Learning Company
300 North Zeeb Road
P.O. Box 1346
Ann Arbor, MI 48106-1346

CASE WESTERN RESERVE UNIVERSITY

SCHOOL OF GRADUATE STUDIES

We hereby approve the thesis/dissertation of

Michael Timothy Grossner

candidate for the Ph.D. degree *.

(signed) _____
(chair of the committee)

_____

_____

_____

_____

_____

(date) _____

*We also certify that written approval has been obtained for any proprietary material contained therein.

I grant to Case Western Reserve University the right to use this work, irrespective of any copyright, for the University's own purposes without cost to the University or to its students, agents and employees. I further agree that the University may reproduce and provide single copies of the work, in any format other than in or from microforms, to the public for the cost of reproduction.

(sign)

Table of Contents

List of Tables viii

List of Figures ix

Acknowledgements xiii

Abstract xiv

1 Introduction 1

1.1 Ultrasonically Enhanced Separation 1

1.2 Research Goals 2

1.3 This Document 3

2 Ultrasonic Waves and Acoustic Forces 4

2.1 Acoustic Pressure Waves 4

2.2 Standing Waves 5

2.3 Acoustic Force on a Sphere 5

3 Previous Work in Ultrasonic Processing 7

3.1 Research at Case Western Reserve University 7

3.1.1 Particle manipulation 7

3.1.2 Particle Separation Using Porous Media 8

3.2 Other Separation Techniques and Applications 10

3.2.1 Gravity Driven Settling 10

3.2.2 Biological Applications 10

4 Single-Fiber Model 12

4.1 Introduction 12

4.2 Coordinate System 12
4.3 General Force Balance 13
4.4 Hydrodynamic Drag Force 14
4.4.1 Drag on a Sphere in Stokes Flow 14
4.4.2 Lamb's Approximate Solution to Creep Flow around a Cylinder 14
4.5 Primary Acoustic Force 15
4.5.1 General Equations 15
4.5.2 Acoustic Velocity Potential Around a Cylinder 16
4.5.3 Acoustic Force Derivation 19
4.6 Equations of Trajectory Motion 21
5 Single-Fiber Model Results 24
5.1 Particle Capture Plots 24
5.2 Capture Window 29
6 Single-Fiber Experiments 33
6.1 Introduction 33
6.2 Equipment 33
6.2.1 Acoustic Separation System 33
6.2.2 Video Imaging System 37
6.3 Procedure 38
6.4 Particle Trajectory Analysis 40
6.4.1 Particle Tracking 40
6.4.2 Cross-Correlation Vector Plots 43

7 Comparison of Experimental Data and Trajectory Model Results 45
7.1 Introduction 45
7.2 Particle Trajectories 46
7.2.1 Model Parameters 46
7.2.2 Comparison Metric 47
7.2.3 Experimental and Model Results 48
7.3 Cross-Correlation Plots 69
7.4 Discussion of Error 75
8 Integrated Model 77
8.1 Introduction 77
8.2 Derivation of the Separator Equations 78
8.2.1 Coordinate System and Important Parameters 78
8.2.2 Conservation Equation 78
8.2.3 Rate Equation 80
8.3 Solution Method 83
8.4 Results 85
8.4.1 Set 1: Gupta and Feke [2] 85
8.4.2 Set 2: Grabenstetter [43] 93
9 Summary and Conclusions 97
9.1 Summary 97
9.2 Future Work 100
9.2.1 Single-Fiber Model and Experiment 100

9.2.2 Integrated Model 100

9.2.3 Other Ideas 101

Appendix 102

MATLAB Code for Single-Fiber Model 102

MATLAB Code for Integrated Model 122

References 125

Bibliography 128

List of Tables

Table 5.1: Typical physical properties of the filtration experiment..... 25

Table 7.1: Physical properties of the single-fiber experiment. 47

Table 7.2: Parameters and results of experimental-model comparisons. The starting position is the value of y (i.e., the vertical distance from the axis of the wire) in the plot at the initial point of the experimentally measured particle trajectory. Both *Gk* and area are dimensionless..... 61

Table 8.1: Parameters of an experiment by Gupta [2]. 86

Table 8.2: Breakthrough time comparison..... 92

Table 8.3: Parameters of an experiment by Grabenstetter [43]. 93

List of Figures

Figure 3.1: A schematic of the separation chamber 8

Figure 4.1: Coordinate system and orientation of cylinder, incident acoustic wave, and fluid flow for trajectory analysis 13

Figure 5.1: Model simulation results. The circle is the cross section of a single mesh element, the direction of suspension flow is from left to right, and the ultrasonic wave resonates between the top and bottom with the nodal plane of the incident field intersecting the visual plane at 90°. The unit of length in all results is the radius of the cylinder (0.1 mm). Arrows indicate the direction of particle motion at a grid point; the solid lines are particle trajectories. The dashed line is the position of the pressure node. No sound field is present in (a). A sound field with a pressure node at the cylinder center is present in (b). The results in (c) show a magnified view of (b); note the position along the node near the fiber where a particle will be suspended in the liquid by a balance of acoustic and drag forces. With the pressure nodes away from the filter element, particle capture may still occur as shown in (d)..... 27

Figure 5.2: With no flow, one can visualize only acoustic forces in (a). The simulation resulting in (b) is identical to (c) except that the acoustic energy is doubled in (c), allowing more particles to be collected. At a flow angle 45° to the plane wave, particles still tend to flow toward the filter element (d). 28

Figure 5.3: The width of the capture window as a function of *Gk* for three different positions of the pressure node of the acoustic plane wave 30

Figure 5.4: With only a small change in *Gk*, from 1.85 (a) to 1.9 (b), the width of the capture window more than doubles. The large effect is due to many trajectories combining into one stream of particles that flows by the filter element in the former and is captured in the latter..... 32

Figure 6.1: An expanded view of the chamber assembly. 35

Figure 6.2: A schematic of the experimental setup..... 36

Figure 6.3: A typical experimental image before (a) and after (b) segmentation. These images are negative of actual images to aid visualization in print. The disc in the center of the images is the wire (in which the

axis is coming out of the page) and the small black blobs are particle images. 41

Figure 7.1: Without acoustic forces, the model predicts a particle trajectory (green) that closely matches experimental data (red). The circle in the center of the plot is a cross-section of the wire, the units of the plot are dimensionless, scaled to the radius of the wire. 51

Figure 7.2: Another particle trajectory in the absence of acoustic forces. The particle in this plot travels in a path farther from the wire than the one in Figure 7.1. 52

Figure 7.3: A plot of an experimentally measured particle trajectory (red dots) along with a simulated one (green line). The blue lines indicate the pressure nodes of the incident plane wave and the circle in the center is the cross-section of the wire. The units of the plot are dimensionless, scaled to the radius of the wire (1 radius = 0.3 mm). For ease in identification, the experimental trajectory shown here is referred to in the text as trajectory A. The simulated particle path follows close to the experimental one in this case, but is not predicted to collide with the cylinder. In the experiment, the particle does indeed collide with and stick to the wire, but in the trajectory analyses, the last few particle positions were not recorded due to particle clumping occurring at that point on the wire. The area between the two trajectories is 0.71..... 53

Figure 7.4: Another experimentally determined particle trajectory, referred to as B in the text, shown with a simulated one. Again, in this case the particle collides with the wire in the experiment, but according to the model, should flow around it. The area between the two trajectories is 0.62.54

Figure 7.5: This experimental trajectory, referred to as C in the text, remains 4 to five radii from the wire. The simulated trajectory in this case has less curvature than the experimental path. The area between the two trajectories is 9.07. 55

Figure 7.6: When only the acoustic wave reflected from the cylinder is used for acoustic force calculations, the simulated particle trajectory, more closely matches the curvature of A (from Figure 7.3). More importantly, the particle is now predicted to collide with the wire. The area between the two trajectories is now slightly larger compared to Figure 7.3, at1.16. 56

Figure 7.7: This plot shows the experimental trajectory B from Figure 7.4 along with simulation results where only the reflected wave is considered. As in the case for A, here the trajectory is predicted to collide with the wire,

but the area between the two trajectories is slightly larger than in Figure 7.4, at 1.14. 57

Figure 7.8: Trajectory C from Figure 7.5 is again depicted, along with simulation results that do not consider the incident plane wave in the acoustic forces. The curvature of the model trajectory is more pronounced in this case (and thus more similar to the experiment than Figure 7.5), but does not closely track the experimental model trajectory. The area between the two trajectories is 9.63. 58

Figure 7.9: An improved fit for trajectory A was found by increasing *Gk* from 0.81 to 1.10, which decreased the area between trajectories to 1.00. 62

Figure 7.10: An improved fit for trajectory B was found by increasing *Gk* from 0.81 to 1.04, which decreased the area between trajectories to 0.46. 63

Figure 7.11: An improved fit for trajectory C was found by decreasing *Gk* from 0.81 to 0.29, which decreased the area between trajectories to 1.72 (from 9.63 in Figure 7.8). 64

Figure 7.12: An additional trajectory (referred to as D in the text) from the same experiment as A and B, but in this case the particle is farther from the wire. The area between the model and the experimental paths for this case of $Gk = 0.81$ is 11.0. 65

Figure 7.13: Trajectory D is shown again with a best fit of $Gk = 0.065$, decreased significantly from the original parameter value. The area between the trajectories is 5.38. 66

Figure 7.14: This experimental trajectory (E) was taken from the same experiment as C, but passes close to the wire. This is the no-parameter-adjustment fit, with $Gk = 0.81$. The area between the trajectories is 1.69. 67

Figure 7.15: Increasing the Gor'kov number to 1.30 for the simulated trajectory decreases the area between it and experimental trajectory E to 1.42.. 68

Figure 7.16: Cross-correlation of experimental video produced the red vector field plotted here; the green vector field is the particle velocity vector field predicted by the model using the original parameters from Table 7.1. Each arrow represents the particle velocity at a particular point (the base of the arrow).The vectors are normalized in order to increase visibility. 72

Figure 7.17: Here, the same experimental results shown in Figure 7.16 are plotted along with results calculated with no acoustic field. The model vectors

here have a gentler slope than in Figure 7.16 and follow the experimental particle flows more closely. 73

Figure 7.18: Cross-correlation from a different experiment with same conditions as the results in Figure 7.16. The experimental vector field shown here is nearly identical to the one shown in Figure 7.16. 74

Figure 8.1: A schematic depicting the coordinate system for the overall model. The suspension flows in from the left at $x = 0$ and exits the chamber at $x =$ L; $y = N/N_T$ is the normalized buildup of particles with $y = 1$ indicating a full mesh. The time variable is t. 79

Figure 8.2: A three-dimensional plot of the normalized buildup of particles inside the chamber as predicted by the integrated model. When N/N_T reaches a value of 1, that portion of the chamber is full. The length of this chamber is 70 mm. 87

Figure 8.3: The normalized concentration at the separator exit for a flow rate of 30 mL/min and an inlet concentration of 0.5 wt%. Other conditions of the experiment are listed in Table 8.1. The red circles are experimental data [2] and the green line is the output of the integrated model. Without any parameter adjustments, breakthrough time is predicted quite well, but the actual concentration does not drop as significantly as the simulation calculates. 88

Figure 8.4: The normalized concentration at the separator exit for a flow rate of 60 mL/min and an inlet concentration of 0.5 wt%. Other conditions of the experiment are listed in Table 8.1. In this case, the experimental output concentrations (red) are again slightly higher than expected from model predictions (green). 89

Figure 8.5: The normalized concentration at the separator exit for a flow rate of 30 mL/min and an inlet concentration of 1.0 wt%. Other conditions of the experiment are listed in Table 8.1. Again, the model predicts a lower concentration (green) than the experiment (red), but the breakthrough time is appropriately scaled from Figure 8.3. 90

Figure 8.6: The normalized concentration at the exit of the separator is shown for both the integrated model (green) and the experiment (red) with conditions shown in Table 8.3 [43]. 95

Figure 8.7: Decreasing the maximum concentration of trapped particles inside the acoustic chamber from 15 volume % to 5 volume % gives a model prediction (green) that predicts a rise in concentration more similar to the experiment (red) than Figure 8.6. 96

Acknowledgements

I would like to thank my advisor, Prof. Donald Feke; without his guidance and inventive problem-solving, this dissertation could not have been accomplished. My wife deserves the most appreciation; Colleen has supported me thoroughly and endured my abnormal work hours—especially toward the end. My family has also stood behind me during my time as a graduate student.

I also thank my colleagues at CSU and CWRU, Prof. Joanne Belovich, Zhaowei Wang, Paul Grabenstetter, David Rusinko, and Gautam Pangu, who were always ready with suggestions and solutions at group meetings. Some of my research depended on the efforts of previous students, especially David Rusinko, Sanjay Gupta, and Alan Penrod. Their excellent work at CWRU has been very useful and will continue to be so for future graduate students. My Ph.D. committee also deserves thanks for taking their time to carefully review my dissertation.

Distractions from research and coursework gave me a better perspective and were always welcome from my friends, Ben, Lisa, Jon, Robin, Scott, Dan, Ram Maddalena, Dave, and Cari. The wonderful support of Dean Lenore Kola, the Office of Graduate Studies, and the Graduate Student Senate allowed me to pursue opportunities in service of CWRU. I would especially like to thank Maddalena, Juilee, and Angela, who helped initiate the Preparing Future Faculty Program; I know that it will live on in our legacy.

Study of Particle Retention in Ultrasonically Enhanced Separation Processes

Abstract

by

MICHAEL TIMOTHY GROSSNER

A method for the capture of small particles (1-100 μm in diameter) from a continuously flowing suspension has recently been reported. This technique relies on an acoustic wave resonating in a rectangular chamber filled with a high-porosity mesh. Particles are retained in this chamber via a complex interaction between the acoustic field and the porous mesh. Although the mesh has a pore size two orders of magnitude larger than the particle diameter, collection efficiencies of 90% have been measured. Two mathematical models have been developed and tested in order to understand experimentally observed phenomena and to predict filtration performance.

First, by examining a small region (a single collection element) of the porous mesh, a single-fiber model was derived from acoustic and transport theory. The model calculates particle flow trajectories based on a force balance between acoustic and drag effects. Adjustments of the angle between flow and acoustic field were studied, along with the position of the incident nodal plane with respect to the fiber. Several experimental events were duplicated using the single-fiber model, such as

focusing of particles near an element of the mesh and levitation of particles within pores.

An experimental chamber incorporating a steel wire was designed to validate this model by examining actual particle paths; images of 54 μm diameter polystyrene particles were recorded using a digital video camera focused on an area of 6 mm x 6 mm surrounding the 0.6 mm diameter wire. Particle tracking and cross-correlation analysis provided particle trajectories and particle flow fields. Without fitting any model parameters, the trajectories matched well; when only waves reflected from the filter element were included in the calculation, the single-fiber model was able to predict particle capture properly. Adjusting the effect of acoustic forces on the particle to better fit the trajectories showed that the applied acoustic field may not necessarily be uniform, as assumed in the model.

The single-fiber analysis formed the basis of modeling the overall performance of the particle filtration system with an integrated model. This overall model was tested with previous experimental work and was able to properly predict breakthrough times of filtration trials. Effects of flow rate and feed concentration on breakthrough time were predicted as well.

1 Introduction

1.1 Ultrasonically Enhanced Separation

A significant number of chemical processes require separation of a solid phase from a continuous liquid phase, either to purify a fluid or to obtain a solid product. One source estimates 70% of all industrial chemical processes involve a finely dispersed phase [1]. Also, fluid phases entrained with biological cells have become more prevalent as biotechnology has evolved. A conventional technique applied to a fluid-particle (or fluid-cell) suspension is physical screening. Other common methods, such as sedimentation and centrifugation, involve the application of a gravitational field to achieve separation.

The idea of applying an external field to affect particle trajectories is not restrained to gravitational forces. Particles with an electrostatic charge may be separated using electric fields, and magnetically susceptible particles can likewise be clarified from a fluid phase. Recently, the application of acoustic fields on suspensions of small particles has been the focus of much research.

Like the buoyancy force utilized in gravitational separation, the force on a particle in an acoustic field is related to the density difference between the particle and the surrounding fluid. However, the acoustic force is also dependent on the difference in the speed of sound within the solid particle and that of the contiguous liquid.

The separation technique studied here relies not only on an applied acoustic field but also the presence of a porous mesh. This mesh contains pores that are

generally one to two orders of magnitude greater than the particle diameter, so physical screening without an acoustic field is not significant. With the application of an ultrasonic field, however, separation efficiencies up to 90% may be realized [2]. This signifies that 90% of the particles from a fluid suspension are retained with a single pass through an experimental chamber.

1.2 Research Goals

There are two main objectives to this work. Of most importance is to gain an understanding of the phenomena involved in the separation process. This includes answering basic questions, such as *how* the particles are held inside a chamber containing a resonant ultrasonic field. Along with this, determining the affect of varying process variables is important. With an understanding of the process, performance prediction is the secondary goal, allowing the optimization of process parameters to produce the best results.

In order to analyze what is happening inside the chamber, the phenomena near a small portion (a single fiber) of the porous mesh were examined. This technique is a standard approach to model a complex system. Using established acoustic theory, the forces acting on particles flowing around a fiber of the porous mesh were modeled in order to project particle paths. Experiments involving a single "wire" were designed to test model results. From the microscopic model, an integrated model was formed, incorporating the entire mesh. The integrated model was designed to predict the performance of the entire system.

1.3 This Document

The next chapter gives essential theory, covering ultrasonic waves and the forces acting on small particles. Chapter 3 reviews previous work in ultrasonic processing of fluids, including research at Case Western Reserve University. The derivation of the single-fiber model and results from that model are presented in Chapters 4 and 5, respectively. Chapter 6 describes the experiments involved in testing the single-fiber model, with comparisons shown in Chapter 7. The model of the entire chamber is derived in Chapter 8, followed by comparisons to actual chamber performance. Finally, conclusions are presented in Chapter 9, with some directions for future work.

2 Ultrasonic Waves and Acoustic Forces

2.1 Acoustic Pressure Waves

Sound waves are periodic (spatial and temporal) variations of pressure in the medium through which the sound is propagating. Waves traveling through a fluid are longitudinal, i.e., the local motion of the fluid is in the same direction as the propagation of the wave. These waves are compressional; small elements of fluid are compressed and stretched in the direction of wave travel—not causing net motion of the fluid. A planar wave traveling in the x direction is described by the following differential equation, where P is the local pressure and c the speed of sound in the medium [3].

$$\frac{\partial^2 P}{\partial t^2} = c^2 \frac{\partial^2 P}{\partial x^2} \tag{2.1}$$

This equation can be rewritten in terms of the velocity potential, Φ.

$$\frac{\partial^2 \Phi}{\partial t^2} = c^2 \frac{\partial^2 \Phi}{\partial x^2} \tag{2.2}$$

The relationship between pressure and velocity potential is

$$P = -\rho_f \frac{\partial \Phi}{\partial t}, \tag{2.3}$$

where ρ_f is the density of the fluid. If the wave is traveling in the $+x$ direction with an angular frequency ω, a solution to Eq. (2.2) is

$$\Phi = A e^{-i\omega t} e^{ikx}, \tag{2.4}$$

where k is the wavenumber, defined as ω / c, and A is the amplitude [3].

2.2 Standing Waves

In an enclosed medium, a traveling wave may reflect upon itself and form a standing wave. The equation for a standing wave is simply the addition of two waves traveling in opposite directions, each described using Eq. (2.4).

$$\Phi = Ae^{-i\omega t}\left(e^{ikx} + e^{-ikx}\right) \tag{2.5}$$

The amplitude of the sound wave in most physical systems is reduced due to absorbed and transmitted sound at boundaries and attenuation within the medium.

2.3 Acoustic Force on a Sphere

A particle immersed in a fluid subjected to a sound wave will experience hydrodynamic forces due to the pressure fluctuations of the wave. In a simple planar standing wave described in Eq. (2.5), the force on a particle due to the acoustic field was derived by Yosioka and Kawasima [4].

$$F_{ac} = 4\pi R_p^{\,3} k E_{ac} F \sin(2kx) \tag{2.6}$$

Here R_p is the radius of the particle and E_{ac} is the acoustic energy density. The acoustic energy density is related to the amplitude of the velocity potential wave function by the following formula.

$$E_{ac} = \frac{\rho_f k^2 A^2}{2} \tag{2.7}$$

The acoustic contrast factor, F, is dependent on the ratio of particle density to fluid density, Λ, and the ratio of sound speeds within the particle and within the fluid, σ.

$$F = \frac{1}{3}\left(\frac{5\Lambda - 2}{1+2\Lambda} - \frac{1}{\sigma^2\Lambda}\right) \quad with \quad \Lambda = \frac{\rho_p}{\rho_f}, \quad \sigma = \frac{c_p}{c_f} \tag{2.8}$$

This factor shows the effect of density difference *and* compressibility (directly related to sound speed) difference. Theoretically, an acoustic separation of a dispersed phase can be effective with a particle and fluid having identical densities, making the technique described in this paper well suited for biological separations, where cells may contain mostly fluid. In practice, this allows unique separation methods to be envisioned that no longer require a large density difference between phases. Some applications involving acoustic manipulation of small particles are given in the next chapter.

3 Previous Work in Ultrasonic Processing

3.1 Research at Case Western Reserve University

3.1.1 Particle manipulation

In 1988, motivated by a need for processing techniques for micron scale particles, Tolt and Feke [5] studied the response of small (80-90 μm diameter) fluidized alumina particles when subjected to resonant, ultrasonic plane waves. In one experiment, as the suspension flowed through a glass cylinder in a direction perpendicular to a standing wave, particles became trapped at the pressure nodal planes. Linear fluid flow rates of up to 0.7 mm/s were not sufficient to disrupt the planar zones of alumina particles. Subsequent work by Tolt and Feke [6,7] involved the design and examination of a separation device based on the glass cylinder.

Since the acoustic force on a spherical particle varies with size of the sphere, a fractionation device that uses sound waves can be envisioned; Mandralis and Feke [8,9] designed such a device. The objective in that research was to separate suspensions into narrow size distribution components. In that case, the flow was parallel to the acoustic plane wave. Oscillation of the flow direction and synchronization with the ultrasonic field allowed particle collection on two sides of a chamber—large particles on one side and small ones on the other. Additional research by Mandralis and others [10,11,12] achieved a fractionation using precisely spaced flow splitters in an acoustically activated chamber. Suspension extracted from points between the spacers had different particle size distribution.

3.1.2 Particle Separation Using Porous Media

The separation process studied in this dissertation was originally developed by Gupta and Feke in 1997 [13,2]. A suspension of micron-scale particles (typically 5-80 μm) was pumped through a rectangular chamber. Two parallel walls of this chamber were a piezoelectric transducer and a glass plate reflector. The interior of the chamber consisted of a highly porous (typically 0.95 void fraction) polyester foam with 10-30 pores per inch. A schematic of the unit is shown in Figure 3.1. When a standing ultrasonic wave was produced in the chamber, particles became entrapped in the mesh, resulting in a product stream with a significantly lower particle concentration. With no active sound field, the particles flowed through the chamber with the fluid.

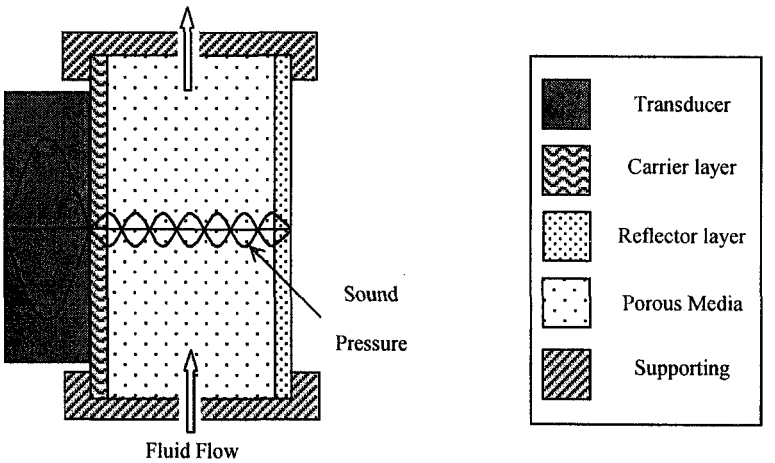

Figure 3.1: A schematic of the separation chamber

The chamber height (along the flow length) was 7 cm; its width was 3.5 cm. The gap between the transducer and reflector could be varied, but was close to 1 cm. These dimensions give a linear flow speed of 1.2 mm/s for a typical pumping speed of 25 mL/min.

An important experimental observation noted was a sharp particle concentration profile. The front of this zone began near the inlet and moved toward the outlet as the media became saturated. Depending on operating parameters, this saturation occurred 5 to 10 minutes (10 to 20 residence times) after the ultrasonic field was activated. The collection was obvious; particles formed clumps and dendrites next to the polyester mesh. In some cases, particles were observed to be held in the void space within a pore as fluid flowed through the chamber [2].

Subsequent research involving the method described above focused on improving the technique. In 1998, Hill [14] studied multi-pass flow through the chamber and noticed an increase in performance. The effect of pore size and sound wavelength was studied by Fine [15]. This work showed that for maximum performance, the pore diameter should be greater than the wavelength of the applied ultrasonic standing wave. It has also been shown that the technique can be applied to the clarification of oil droplet emulsions [16].

3.2 Other Separation Techniques and Applications

3.2.1 Gravity Driven Settling

Flocculation of particulate matter and subsequent sedimentation is common in municipal wastewater treatment facilities [17]. In small scale experiments, acoustic forces have been used to increase flocculation in order to create larger clumps of particles, thus increasing sedimentation [18,19]. This method, effective for dense particles, relies on large density differences between the particulate phase and the continuous phase, and can be quite a slow process, with settling velocities of 2 - 6 feet per hour (0.17 - 0.51 mm/s) [17].

3.2.2 Biological Applications

As mentioned in section 2.3, ultrasonic separation methods lend themselves well to biological systems. Viability studies of plant cells, yeast cells, and erythrocytes have been performed and it has been concluded that cellular viability depends on the acoustic energy density, the exposure time, and the mechanical properties of the cell, determined by age [20,21,22]. It is noted in two of these studies [20,21] that the agglomeration of cells within the pressure nodal planes minimized damaging effects due to the ultrasound.

Most cell separation studies using ultrasound fall into the category of gravity driven settling [23,24,25]. These techniques use resonant ultrasonic fields to clump cells together in order to increase sedimentation rates to around 0.15 mm/s [25]. A

few filtering methods use a physical flow splitter, using ultrasound to force cells to one exit stream, while clarified fluid flows through another [26].

Another use for ultrasound in cellular applications is in the area of micromanipulation. Yasuda et al. have studied the potential use of ultrasound to handle biomaterials in a micro-chamber, erythrocytes were mixed with a dye for sample preparation [27].

Besides plant and animal cell separation and manipulation, ultrasound may be used for medicine-related processing. Researchers at Cardiff University have developed a commercial device that uses ultrasound to increase the performance of a laboratory test for meningitis [28]. Also at Cardiff, whole blood has been clarified to plasma with an ultrasonic mechanism [29].

4 Single-Fiber Model

4.1 Introduction

In order to understand the operation and experimental observations of the ultrasonically aided separation method described in 3.1.2, a mathematical model was created that attempts to predict the motion of particles in response to the acoustic and flow forces present within the mesh. If proven successful, such a model can form the foundation for optimization of the device design and selection of process parameters.

Since the geometry of the mesh is complex, the standard modeling practice of studying the region surrounding one element of the filter media is adopted. Here the mesh is pictured as an assembly of cylinders.

4.2 Coordinate System

The model intends to provide the two-dimensional trajectories of particles in the vicinity of one mesh element, assumed to be an infinite circular cylinder. The axis of the cylinder fiber is perpendicular both to the upstream flow direction and to the direction of the incident ultrasonic plane wave. The angle between the directions of the approach flow and the acoustic field, however, is arbitrary. Figure 4.1 defines the coordinate systems used for the trajectory calculations. The fluid flow is described using Cartesian (x, y) coordinates, with the approach flow always in the $+x$ direction. The polar angle ϕ measured from the $+x$ direction is used to describe the hydrodynamic flow field. The acoustic field is described using (x', y')

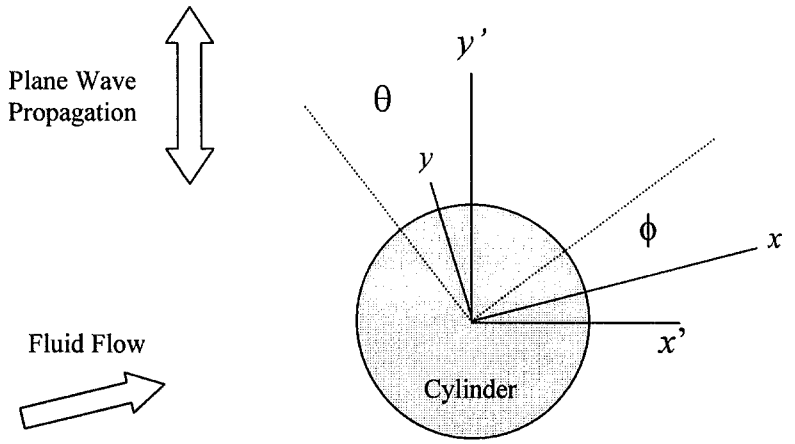

Figure 4.1: Coordinate system and orientation of cylinder, incident acoustic wave, and fluid flow for trajectory analysis

coordinates, with the incident acoustic field propagating in the y'-direction. The polar angle θ is measured from the $+y$'-direction.

4.3 General Force Balance

Several assumptions are adopted for the derivation of the particle trajectory equations: (1) creeping flow around the cylinder, i.e., $Re_c < 1$; (2) the flow field is unaffected by the presence of the particles; (3) gravitational effects are negligible; (4) the particle concentration is dilute so that there are no interparticle hydrodynamic or acoustic interactions; (5) the mass of particles is small enough that inertia is negligible; (6) secondary acoustic forces are ignored; and (7) the fluid flows at steady state. Given these assumptions, the overall force balance on a particle gives

$$\mathbf{F}_{ac} + \mathbf{F}_{D} = \mathbf{0}, \tag{4.1}$$

where $\mathbf{F}_{ac}$ is the primary acoustic force and $\mathbf{F}_{D}$ is the hydrodynamic drag force.

4.4 Hydrodynamic Drag Force

4.4.1 Drag on a Sphere in Stokes Flow

The drag force acting on a sphere under creeping flow conditions is given by

$$\mathbf{F}_{\mathrm{D}} = 6\pi\mu\left(\mathbf{u}_{\mathrm{f}} - \mathbf{u}_{\mathrm{p}}\right)R_p, \tag{4.2}$$

where μ is the fluid viscosity, $\mathbf{u}_{\mathrm{f}}$ is the fluid velocity, $\mathbf{u}_{\mathrm{p}}$ is the particle velocity, and R_p is the radius of the spherical particle. This solution is accurate for Reynolds numbers less than 0.1 and is accurate to 5% for Reynolds numbers up to one [30].

4.4.2 Lamb's Approximate Solution to Creep Flow around a Cylinder

Lamb provides a solution for creeping flow around an infinite cylinder in Cartesian coordinates [31]. The x and y velocities (u_{fx} and u_{fy}, respectively) of the flow are

$$\begin{aligned} u_{fx} &= \frac{1}{2}C\left[\gamma - \frac{1}{2} + \ln\frac{1}{2}\kappa r + \frac{1}{2}\left(r^2 - R_c^{\,2}\right)\frac{\partial^2}{\partial x^2}\ln\frac{r}{R_c}\right] + U_f \\ u_{fy} &= \frac{1}{4}C\left[\left(r^2 - R_c^{\,2}\right)\frac{\partial^2}{\partial x \partial y}\ln\frac{r}{R_c}\right] \end{aligned}, \tag{4.3}$$

where γ is Euler's number ($\gamma = 0.5772$ [32]), R_c is the cylinder radius, and r is the radial coordinate. The parameters C and κ are defined by

$$C = \frac{2U_f}{\frac{1}{2} - \gamma - \ln\frac{1}{2}\kappa a} \quad \text{and} \quad \kappa = \frac{U_f \rho}{2\mu}. \tag{4.4}$$

From the relationship between the Cartesian and cylindrical coordinates, it can readily be shown that

$$\frac{\partial^2}{\partial x^2}\ln r = -\frac{\cos 2\phi}{r^2} \tag{4.5}$$

and

$$\frac{\partial^2}{\partial x \partial y}\ln r = -\frac{\sin 2\phi}{r^2}. \tag{4.6}$$

Substituting Eqs. (4.4), (4.5), and (4.6) into Eq. (4.3) the flow velocity becomes

$$u_{fx} = U_f \frac{\ln\frac{r}{R_c} - 0.5\left(1 - R_c^2/r^2\right)\cos 2\phi}{2.002 - \ln \mathrm{Re}_c} \tag{4.7}$$

and

$$u_{fy} = \frac{-0.5U_f\left(1 - R_c^2/r^2\right)\sin 2\phi}{2.002 - \ln \mathrm{Re}_c}. \tag{4.8}$$

4.5 Primary Acoustic Force

4.5.1 General Equations

The results of Gor'kov [33], corrected by Barmatz and Collas [34], are used to determine the primary acoustic force. The primary acoustic force is given by the negative gradient of the acoustic potential U,

$$\mathbf{F}_{ac} = -\nabla U, \tag{4.9}$$

where

$$U = 2\pi R_p^3 \rho_f \left(\frac{\langle P^2 \rangle}{3\rho_f^2 c_f^2} f_1 - \frac{\langle V^2 \rangle}{2} f_2 \right). \tag{4.10}$$

Here c_f is the longitudinal sound speed in the fluid, P and V the local pressure and velocity in the fluid at the location of the particle, and $\langle\ \rangle$ denotes a time average. The factors f_1 and f_2 are given by

$$f_1 = 1 - \frac{c_f^2 \rho_f}{c_p^2 \rho_p} \quad \text{and} \quad f_2 = 2\left(\frac{\rho_p - \rho_f}{2\rho_p + \rho_f} \right), \tag{4.11}$$

where ρ_p is the particle density and c_p is the longitudinal sound speed in the particle. The factors have allowable ranges of $-\infty < f_1 \leq 1$ and $-2 \leq f_2 \leq 1$.

The local pressure and velocity can be written from the real portion of the velocity potential Φ,

$$\begin{aligned} P &= \mathrm{Re}\left(-\rho_f \frac{\partial \Phi}{\partial t} \right) \\ \mathbf{V} &= \mathrm{Re}\left(\nabla \Phi \right) \end{aligned} \tag{4.12}$$

4.5.2 Acoustic Velocity Potential Around a Cylinder

Hasegawa et al. have developed a velocity potential for a plane progressive wave incident upon a cylinder [35]. The velocity potential of an incident plane standing wave (essentially Eq. (2.5) written in cylindrical coordinates) is represented by

$$\Phi_i = A \exp(i\omega t) \sum_{n=0}^{\infty} \varepsilon_n (-i)^n \delta_n J_n(kr) \cos(n\theta), \tag{4.13}$$

where the term δ_n transforms Hasegawa's expression for progressive waves into a standing wave using the functions

$$\varepsilon_n = \begin{cases} 1 & \text{for } n = 0 \\ 2 & \text{for } n = 1,2,3... \end{cases} \quad \text{and} \quad \delta_n = e^{-ikh} + (-1)^n e^{ikh}. \tag{4.14}$$

Here θ is the angle relative to the direction of propagation of the acoustic field, r is the radial coordinate, A is the amplitude of the potential, h is the distance between the nodal plane and the axis of the cylinder, ω the radial frequency, and k the wavenumber. J_n is the cylindrical Bessel function of the first kind and order n. Making the simplifications

$$B_n = \varepsilon_n (-i)^n \delta_n \quad \text{and} \quad v = kr, \tag{4.15}$$

Eq. (4.13) can be rewritten as

$$\Phi_i = A \exp(i\omega t) \sum_{n=0}^{\infty} B_n J_n(v) \cos(n\theta). \tag{4.16}$$

The scattered field potential is written as

$$\Phi_s = A \exp(i\omega t) \sum_{n=0}^{\infty} B_n d_n H_n^{(2)}(v) \cos(n\theta), \tag{4.17}$$

with

$$H_n^{(2)}(v) = J_n(v) - iY_n(v), \tag{4.18}$$

where $Y_n(v)$ is the cylindrical Bessel function of the second kind and order n. The coefficients d_n are given by Faran [36] and are recast by Hasegawa et al. with algebraic errors [35]. The corrected coefficients are presented here for convenience.

$$d_n = -\frac{F_n J_n(x) - xJ_n'(x)}{F_n H_n^{(2)}(x) - xH_n'^{(2)}(x)}, \tag{4.19}$$

where

$$F_n = \frac{\rho_f x_2^2}{2\rho_c} \frac{(\hat{A}_n - \hat{B}_n)}{(\hat{C}_n - \hat{D}_n)} \tag{4.20}$$

with

$$\begin{aligned}
\hat{A}_n &= -\frac{x_1 J_n'(x_1)}{J_n(x_1) - x_1 J_n'(x_1)} \\
\hat{B}_n &= \frac{2n^2 J_n(x_2)}{n^2 J_n(x_2) - x_2 J_n'(x_2) + x_2^2 J_n''(x_2)} \\
\hat{C}_n &= -\frac{\left(\frac{x_2^2}{2} - x_1^2\right)\left(J_n(x_1) - J_n''(x_1)\right)}{J_n(x_1) - x_1 J_n'(x_1)} \\
\hat{D}_n &= \frac{2n^2\left(J_n(x_2) - x_2 J_n'(x_2)\right)}{n^2 J_n(x_2) - x_2 J_n'(x_2) + x_2^2 J_n''(x_2)}
\end{aligned} \tag{4.21}$$

Here ρ_c is the density of the cylinder and x, x_1, and x_2 are given by

$$x = kR_c, \quad x_1 = \frac{\omega R_c}{c_1}, \quad \text{and} \quad x_2 = \frac{\omega R_c}{c_2}, \tag{4.22}$$

with c_1 and c_2 the velocities of longitudinal and shear waves in the cylinder material, respectively. Writing the velocity potential as the sum of the incident and scattered parts, the combined field potential is

$$\Phi = A\exp(i\omega t)\sum_{n=0}^{\infty} B_n\left[J_n(v) + d_n H_n^{(2)}(v)\right]\cos(n\theta). \tag{4.23}$$

4.5.3 Acoustic Force Derivation

Because the solution requires the real component of the potential function, Φ will be rearranged to facilitate the separation into the complex coordinates. With the definition

$$d_n = a_n + ib_n, \tag{4.24}$$

where a_n and b_n are the real and imaginary components of d_n, respectively, and using Eq. (4.18), the right hand portion of Eq. (4.23)can be arranged to

$$\begin{aligned}
&\cos n\theta\left(J_n(v) + d_n H_n^{(2)}(v)\right) \\
&= \cos n\theta\left(J_n(v) + (a_n + ib_n)(J_n(v) - iY_n(v))\right) \\
&= \cos n\theta\left[(1+a_n)J_n(v) + b_n Y_n(v) + i\left(b_n J_n(v) - a_n Y_n(v)\right)\right]
\end{aligned} \tag{4.25}$$

Defining

$$\begin{aligned}
S_n &= \cos n\theta\left[(1+a_n)J_n(v) + b_n Y_n(v)\right] \\
T_n &= \cos n\theta\left[b_n J_n(v) - a_n Y_n(v)\right]
\end{aligned}, \tag{4.26}$$

Eq. (4.23) can be written as

$$\Phi = A\exp(i\omega t)\sum_{n=0}^{\infty} B_n(S_n + iT_n). \tag{4.27}$$

Note that S_n and T_n are real provided $v > 0$ (since the coordinate system is cylindrical, $v = kr$ is always greater than zero and this is satisfied). Also note that B_n is real for all n (this may be proved by showing that B_n is real for even and odd n separately). With the additional definition of

$$\begin{aligned} W &= \sum_{n=0}^{\infty} B_n S_n \\ X &= \sum_{n=0}^{\infty} B_n T_n \end{aligned}, \tag{4.28}$$

the velocity potential can be written as

$$\Phi = A\exp(i\omega t)(W + iX), \tag{4.29}$$

where W and X are real functions of v and θ. From Eq. (4.12),

$$P = \mathrm{Re}\left(-i\omega\rho_f A\exp(i\omega t)(W + iX)\right), \tag{4.30}$$

or

$$P = \omega\rho_f A(W\sin\omega t + X\cos\omega t). \tag{4.31}$$

The time-averaged square of pressure is

$$\left\langle P^2\right\rangle = \frac{(W^2 + X^2)\omega^2\rho_f^2 A^2}{2}. \tag{4.32}$$

The expression for the velocity is similarly found to be

$$\begin{aligned} \mathbf{V} &= \mathrm{Re}\left[A\exp(i\omega t)\left(\frac{\partial W}{\partial r} + i\frac{\partial X}{\partial r}\right)\tilde{\mathbf{e}}_r + A\exp(i\omega t)\left(\frac{1}{r}\frac{\partial W}{\partial\theta} + i\frac{1}{r}\frac{\partial X}{\partial\theta}\right)\tilde{\mathbf{e}}_\theta\right] \\ &= A\left[\left(\frac{\partial W}{\partial r}\cos\omega t - \frac{\partial X}{\partial r}\sin\omega t\right)\tilde{\mathbf{e}}_r + \left(\frac{1}{r}\frac{\partial W}{\partial\theta}\cos\omega t - \frac{1}{r}\frac{\partial X}{\partial\theta}\sin\omega t\right)\tilde{\mathbf{e}}_\theta\right] \end{aligned}, \tag{4.33}$$

where $\tilde{\mathbf{e}}_r$ and $\tilde{\mathbf{e}}_\theta$ are the unit vectors in cylindrical coordinates. From this result,

$$\begin{aligned} \left\langle V^2\right\rangle &= \frac{A^2}{2}\left[\left(\frac{\partial W}{\partial r}\right)^2 + \left(\frac{\partial X}{\partial r}\right)^2 + \frac{1}{r^2}\left(\frac{\partial W}{\partial\theta}\right)^2 + \frac{1}{r^2}\left(\frac{\partial X}{\partial\theta}\right)^2\right] \\ &= \frac{k^2A^2}{2}\left[\left(\frac{\partial W}{\partial v}\right)^2 + \left(\frac{\partial X}{\partial v}\right)^2 + \frac{1}{v^2}\left(\frac{\partial W}{\partial\theta}\right)^2 + \frac{1}{v^2}\left(\frac{\partial X}{\partial\theta}\right)^2\right] \end{aligned}. \tag{4.34}$$

With the definitions

$$P^* = \left(W^2 + X^2\right) \quad \text{and}$$
$$\mathrm{V}^* = \left[\left(\frac{\partial W}{\partial v}\right)^2 + \left(\frac{\partial X}{\partial v}\right)^2 + \frac{1}{v^2}\left(\frac{\partial W}{\partial \theta}\right)^2 + \frac{1}{v^2}\left(\frac{\partial X}{\partial \theta}\right)^2\right] \tag{4.35}$$

the equation for the acoustic potential (Eq. (4.10)) can be written as

$$U = 2\pi R_p^3 k^2 A^2 \rho_f \left(\frac{P^*}{6} f_1 - \frac{V^*}{4} f_2\right). \tag{4.36}$$

A dimensionless potential U^* is defined as

$$U^* = \frac{U}{4\pi R_p^3 E_{ac}} = \left(\frac{P^*}{6} f_1 - \frac{V^*}{4} f_2\right). \tag{4.37}$$

For the given coordinate system

$$F_{ac,x'} = -F_{ac,r}\sin\theta - F_{ac,\theta}\cos\theta \quad \text{and}$$
$$F_{ac,y'} = F_{ac,r}\cos\theta - F_{ac,\theta}\sin\theta, \tag{4.38}$$

when Eqs. (4.9), (4.37), and (4.38) are combined, the acoustic forces in the x' and y' directions are represented by

$$F_{ac,x'} = 4\pi R_p^3 E_{ac} k \left[\frac{\partial U^*}{dv}\sin\theta + \frac{1}{v}\frac{\partial U^*}{d\theta}\cos\theta\right] \tag{4.39}$$

$$F_{ac,y'} = -4\pi R_p^3 E_{ac} k \left[\frac{\partial U^*}{dv}\cos\theta - \frac{1}{v}\frac{\partial U^*}{d\theta}\sin\theta\right]. \tag{4.40}$$

4.6 Equations of Trajectory Motion

Once the angle between the approach flow and the incident acoustic field is chosen, it is possible to combine the acoustic force expression, Eqs. (4.39) and (4.40),

with the hydrodynamic drag expressions, Eq. (4.2) with Eqs. (4.7) and (4.8), to determine the trajectory of the particles according to

$$\mathbf{u_p} = \mathbf{u_f} + \frac{\mathbf{F_{ac}}}{6\pi\mu R_p}. \tag{4.41}$$

For ease in computation and representation of results, the equations of particle motion are cast in terms of dimensionless variables.

$$\frac{dx_p^*}{dt^*} = \frac{2Gk}{3}\left[\frac{\partial U^*}{dv}\sin\theta + \frac{1}{v}\frac{\partial U^*}{d\theta}\cos\theta\right] + \frac{\ln r^* - 0.5\left(1-1/r^{*2}\right)\cos 2\phi}{2.002 - \ln Re_c} \tag{4.42}$$

$$\frac{dy_p^*}{dt^*} = -\frac{2Gk}{3}\left[\frac{\partial U^*}{dv}\cos\theta - \frac{1}{v}\frac{\partial U^*}{d\theta}\sin\theta\right] - 0.5\frac{\left(1-1/r^{*2}\right)\sin 2\phi}{2.002 - \ln Re_c} \tag{4.43}$$

The dimensionless variables (indicated by *) are defined by

$$x_p^* = \frac{x_p}{R_c}, \quad y_p^* = \frac{y_p}{R_c}, \quad r^* = \frac{r}{R_c}, \quad \text{and} \quad t^* = \frac{U_f t}{R_c}. \tag{4.44}$$

The variables x_p and y_p represent the coordinates of the particle while r and ν ($=kr$, where k is the wave number of the acoustic field) also denote the distance from the center of the cylinder. The Gor'kov number,

$$Gk = \frac{R_p^2 k E_{ac}}{\mu U_f}, \tag{4.45}$$

represents the ratio of acoustic forces to hydrodynamic drag forces on the particles while the Reynolds number based on the cylinder diameter,

$$Re_c = \frac{2U_f R_c \rho_f}{\mu}, \tag{4.46}$$

characterizes the flow strength. The radius of the particle and the cylinder (filter element) are R_p and R_c, respectively. The fluid velocity far upstream is U_f; the fluid has viscosity μ and density ρ_f. The acoustic energy density is E_{ac} and U^* is the dimensionless acoustic potential, which depends on the position of the cylinder relative to the incident acoustic field.

5 Single-Fiber Model Results

5.1 Particle Capture Plots

Given the system of equations derived in the previous chapter, Eqs. (4.42) and (4.43), the particle motion can be computed at each point in space, and these motions can be integrated to predict particle trajectories in the vicinity of the cylinder. A simple substitution method is used to solve the set of differential equations to obtain these trajectories. Stopping conditions include a particle impinging upon the fiber element, leaving the selected area of interest, or levitating at a point in space.

Although the model allows for all variables to be adjusted, the results presented here show only the effect of varied cylinder positions (with respect to the incident acoustic field), angle of the fluid flow, and intensity of the acoustic field. The physical parameters used in the model, chosen to match those in typical experiments, are listed in the following table. These parameters result in a Re_c of 0.1.

With no acoustic forces, the particles merely trace the motion of the fluid around the cylinder, as shown in Figure 5.1(a). This figure shows both local and integrated particle trajectories. The circle in the center of the plot is the cross-section of the cylinder. The field of arrows in the background is the direction of particle motion if the particle was located at the position corresponding to the tail of the arrow. The solid curves indicate the paths particles will follow if placed at the upstream end (the left edge) of the curve.

Table 5.1: Typical physical properties of the filtration experiment

Acoustic field	
Energy density (E_{ac})	0.5 J/m^3
Frequency ($\omega/2\pi$)	1 MHz
Fluid: pure water	
Bulk velocity (U_f)	0.5 mm/s
viscosity (μ)	0.001 kg/m s
density (ρ_f)	1000 kg/m^3
longitudinal sound speed (c_f)	1480 m/s
Filter element: polyester	
radius (R_c)	0.1 mm
density (ρ_c)	1230 kg/m^3
longitudinal sound speed (c_1)	2430 m/s
shear sound speed (c_2)	1200 m/s
Particles: polystyrene	
Radius (R_p)	10 μm
Density (ρ_p)	1050 kg/m^3

When including the effects of the ultrasonic field, particles are shown to collide with the cylinder (Figure 5.1 (b)) where they are presumed to stick upon contact. This simulation case has a pressure node of the incident standing wave placed directly at the center of the cylinder. Since the particles have properties that result in motion toward the pressure nodes of the acoustic field, this configuration is advantageous for particle collection.

Figure 5.1(c) shows a magnified region of Figure 5.1(b). Here the two particle capture methods mentioned in the previous section can be visualized. At a spot just upstream of the cylinder, particles are trapped, levitated in the fluid by a

combination of acoustic and drag forces. The other capture scheme is shown as particles are impinged on the surface of the cylinder.

In contrast, one might expect that locating the cylinder on an acoustic antinode would be detrimental to particle capture since particles would migrate away from the antinode. However, Figure 5.1(d) shows that particles will continue to be captured even in this case. This result stems from the interaction between the incident and the waves reflected from the cylinder, which actually attracts particles to the filter element at some locations. In order to better visualize the effect of the overall acoustic field, Figure 5.2(a) presents the results when the flow speed is set to zero. Note that the acoustic field alone does direct particles to certain locations on the cylinder, even though the cylinder is positioned at the antinode of the incident field.

When the cylinder is positioned off of both acoustic nodes and antinodes of the incident field, a more complicated trajectory pattern results (see Figure 5.2(b)). In this particular case, there are four distinct spots on the cylinder surface to which particles from a range of origination points are attracted. This focusing is frequently seen in the model results and explains the experimentally observed formation of particle dendrites that have been observed in experiments [37].

Figure 5.2(d) shows that particles entering with a flow angle of 45° with respect to the incident acoustic field can still be captured. Particle trajectories in this simulation are focused to the same points on the cylinder as Figure 5.2(b), again indicating that the acoustic fields are the driving force for particle retention.

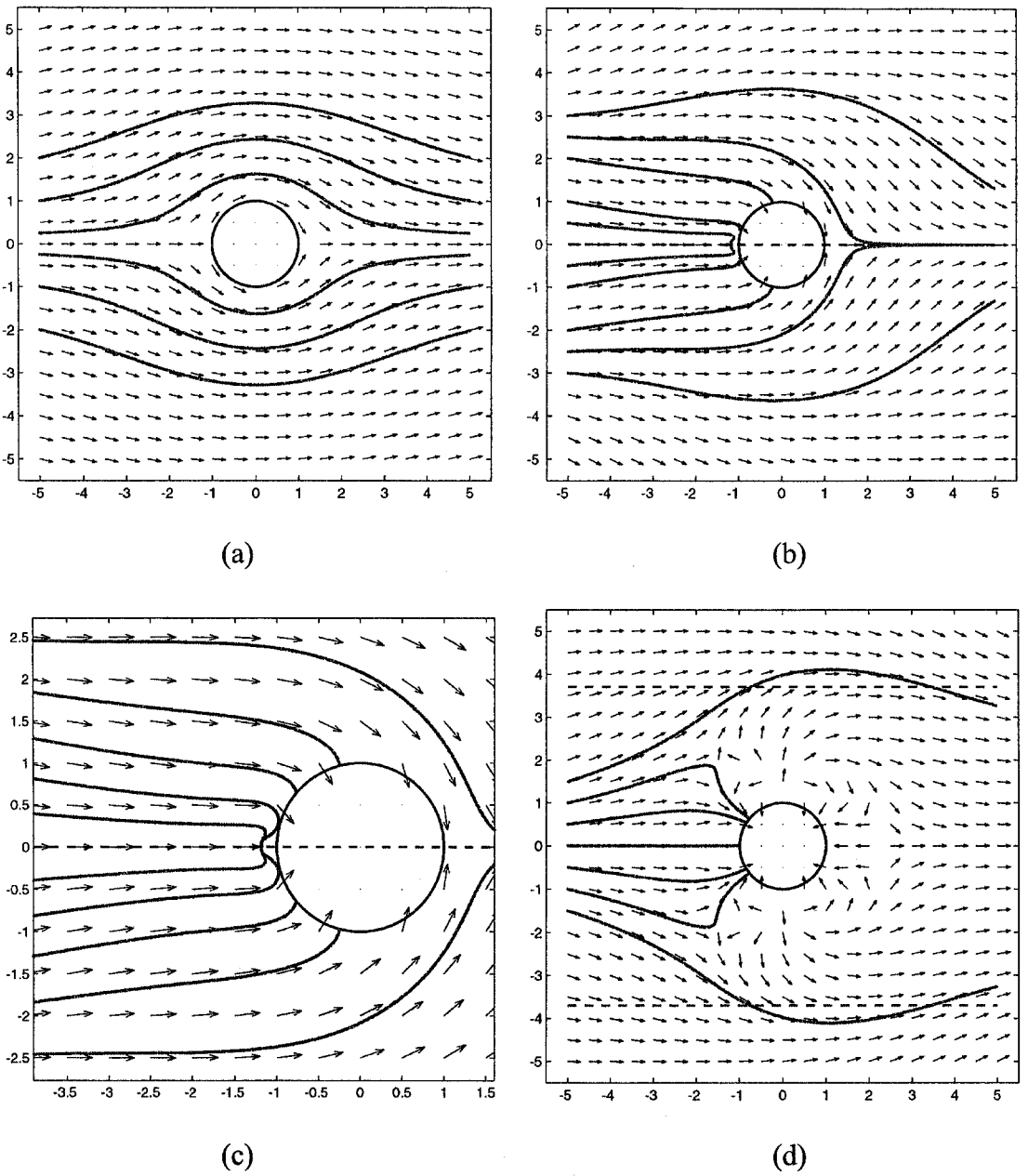

Figure 5.1: Model simulation results. The circle is the cross section of a single mesh element, the direction of suspension flow is from left to right, and the ultrasonic wave resonates between the top and bottom with the nodal plane of the incident field intersecting the visual plane at 90°. The unit of length in all results is the radius of the cylinder (0.1 mm). Arrows indicate the direction of particle motion at a grid point; the solid lines are particle trajectories. The dashed line is the position of the pressure node. No sound field is present in (a). A sound field with a pressure node at the cylinder center is present in (b). The results in (c) show a magnified view of (b); note the position along the node near the fiber where a particle will be suspended in the liquid by a balance of acoustic and drag forces. With the pressure nodes away from the filter element, particle capture may still occur as shown in (d).

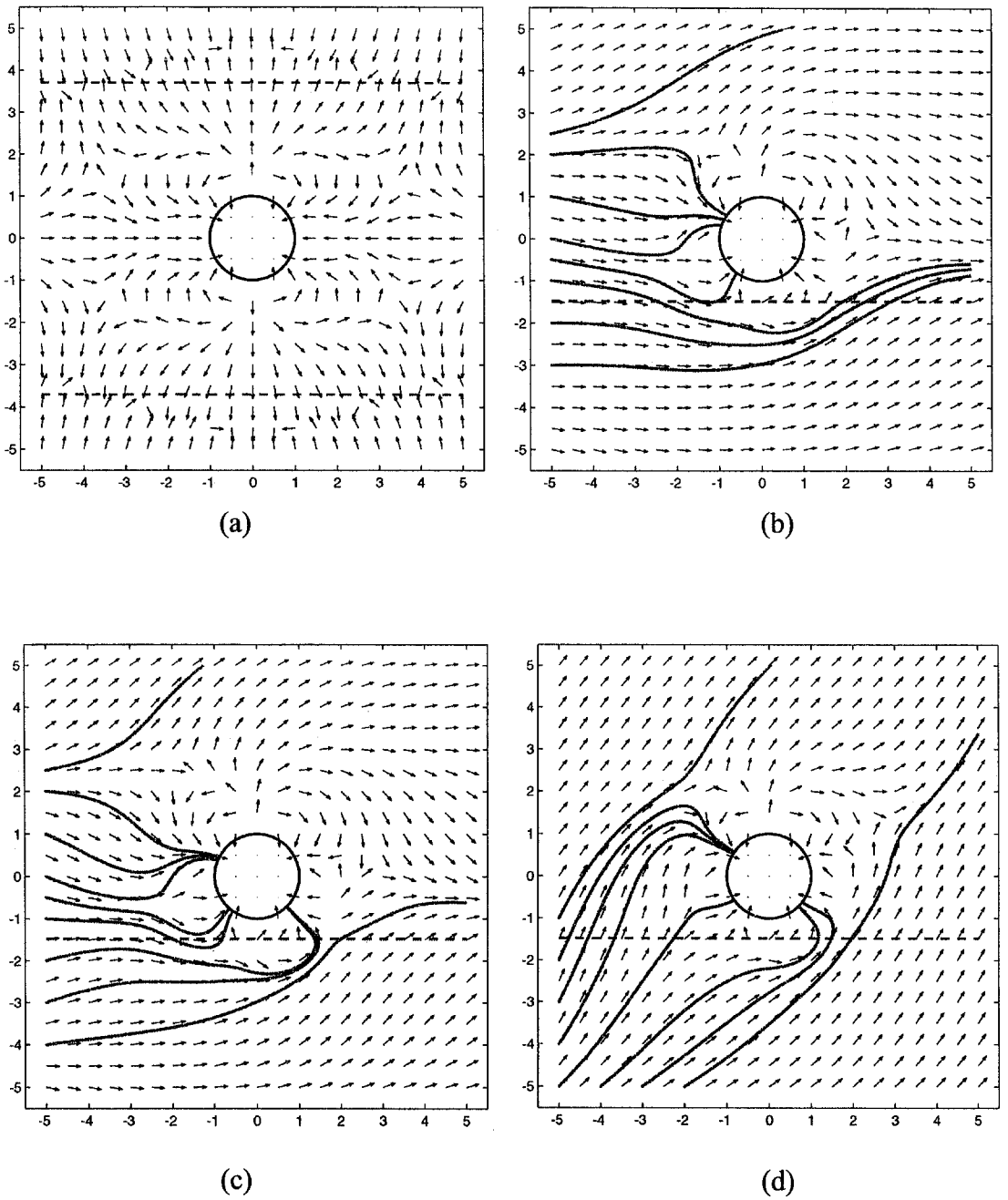

Figure 5.2: With no flow, one can visualize only acoustic forces in (a). The simulation resulting in (b) is identical to (c) except that the acoustic energy is doubled in (c), allowing more particles to be collected. At a flow angle 45° to the plane wave, particles still tend to flow toward the filter element (d).

5.2 Capture Window

In order to compare the effectiveness of the filter element, it is beneficial to devise a metric for evaluating capture performance. Consider a cross-sectional area perpendicular to the bulk flow direction and upstream from the filter element. There exists a "capture window" in this plane through which all particles that eventually collide with the cylinder pass. The width of the capture window can be used as a measure of the capture efficiency under different experimental conditions. For example, the width of the capture window in the case of Figure 5.2(b) is about three cylinder radii for an acoustic energy density of 0.5 J/m^3 (corresponding to a Gor'kov number of 0.42 for these conditions). If the acoustic energy density is doubled to 1 J/m^3 (Figure 5.2(c)), the width of capture increases to more than five radii.

Figure 5.3 shows how the width of the capture window varies with *Gk* for three different nodal positions for the case of perpendicular flow and incident acoustic field. The capture widths were calculated by evaluating particle trajectories at each set of data (*Gk*, nodal position), which corresponds to one point on the plot. The small jumps in the plot are due to imprecision in the width of the capture window, which is precise to ± 0.0625 radii.

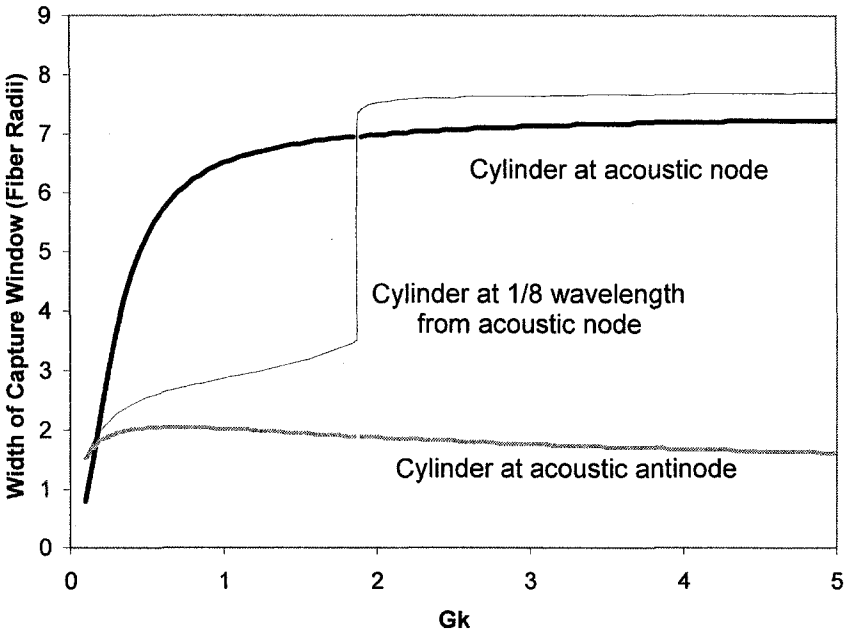

Figure 5.3: The width of the capture window as a function of *Gk* for three different positions of the pressure node of the acoustic plane wave

As seen in Figure 5.3, the performance of the filter element in each case hits a plateau before *Gk* reaches a value of 2. Increasing the acoustic energy beyond this point does not increase the width of the capture window. When the pressure antinode is at the cylinder axis, the plateau value decays slightly with *Gk* and will eventually reach zero. This effect is expected, since, as the acoustic energy is increased, particles will be forced to the pressure nodes (and away from the filter element) with greater intensity. For each of the other two cases, the capture width remains constant at large values of *Gk*.

One feature seems unusual in Figure 5.3, the large increase in capture width near Gk=1.85 for the case of the node placed 1/8 wavelength from the cylinder axis. It is useful to explain this with the visual aid of trajectory plots. Figure 5.4 shows the particle trajectories for Gk=1.85 and Gk=1.9; the capture widths are 3.4 and 7.4 fiber radii, respectively. Just below the pressure node, the particle trajectories combine into one streamline. The critical point for capture of this streamline lies between a Gk of 1.85 and 1.9.

All of the particle trajectories used for visualization and for capture window calculations begin at a position located 5 fiber radii upstream from the cylinder axis. The area of the capture window would change if the starting position of the particles were changed to be more upstream or downstream from the filter element because the force due to the incident plane wave is always present. Since the particles are believed to be well dispersed between pores in the mesh, a value of 5 radii (corresponding to 0.5 mm, in this case) was chosen, corresponding to the midpoint between to filter elements in a 25 pore per inch mesh.

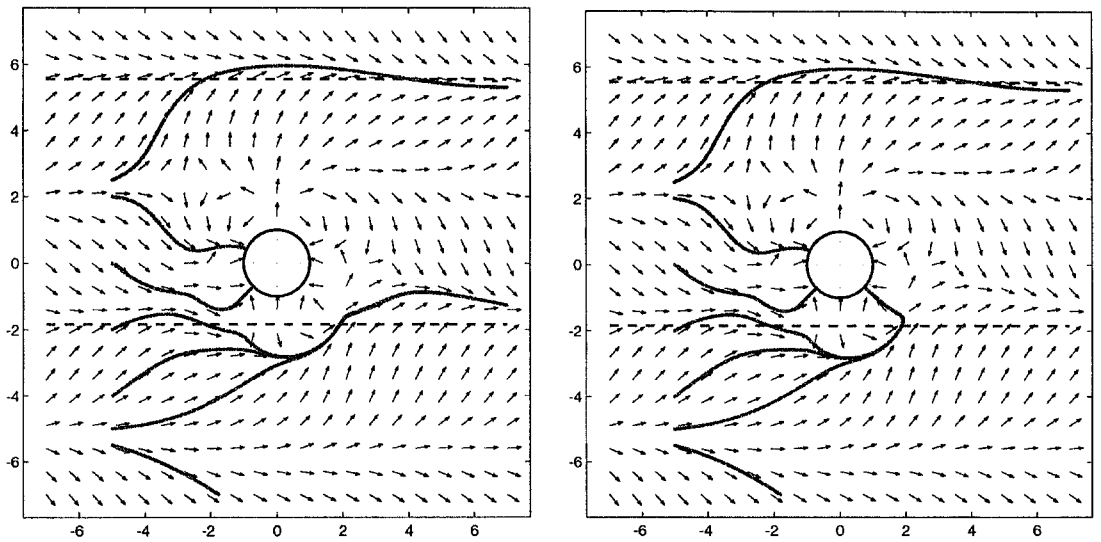

Figure 5.4: With only a small change in *Gk*, from 1.85 (a) to 1.9 (b), the width of the capture window more than doubles. The large effect is due to many trajectories combining into one stream of particles that flows by the filter element in the former and is captured in the latter.

6 Single-Fiber Experiments

6.1 Introduction

In order to determine the validity of the single-fiber model described in the preceding chapters, an experimental system was designed. Since visualization of particle trajectories around one fiber was necessary, the system included a chamber with a single wire (corresponding to the fiber in the model), a digital video camera with a computer interface, and software for image analysis. The chamber was connected to a flow system that supplied a suspension of particles through the device. To activate and control the transducer, a signal generator, power amplifier, and power meter were attached to the transducer leads. This chapter will describe the equipment used in the experiments along with the techniques used for image acquisition and analysis.

6.2 Equipment

6.2.1 Acoustic Separation System

6.2.1.1 Chamber

The basic design of the chamber was very similar to previous separation units (see Section 3.1.2). A rectangular piezoelectric transducer (PZT, Navy Type I, EDO Electro Ceramics Corporation, Model EC-64, 4.60 cm x 7.75 cm x 10.03 mm) formed one wall of the chamber, while a glass sheet (4.85 cm x 8.20 cm x 1.04 mm thick) formed the opposite wall. The main body of the chamber was acrylic. A thin silicone sheet was glued around the edges of the transducer and also around the edges of the

glass reflector. This allowed a seal to be made when two supporting aluminum pieces were clamped to the structure. Also, having the transducer and reflector suspended without a rigid attachment to the support structure reduced losses of acoustic energy. Adjustable knobs attached to the aluminum support structure were used to align the transducer and reflector; an exactly parallel configuration is ideal for optimum resonance conditions. The knobs pushed against an acrylic positioning plate, which was attached to the transducer (and reflector) with two pieces of foam. See Figure 6.1 for a schematic of the assembly.

In order to have the suspension flow around a cylinder, a stainless steel wire was fixed inside the chamber. This particular material was chosen due to its rigidity (to reduce bowing in the flow) and its availability in a small, precise diameter (0.020 in.). The wire was passed though a hole in one side of the acrylic center piece and friction fitted inside a hole drilled 2 mm into the inner wall of the other side of the center piece. This configuration enabled an unobstructed view of the wire cross-section looking into the chamber through the wall with the partially drilled hole. A small amount of silicone glue was placed at the end of the wire protruding from the acrylic to seal the hole.

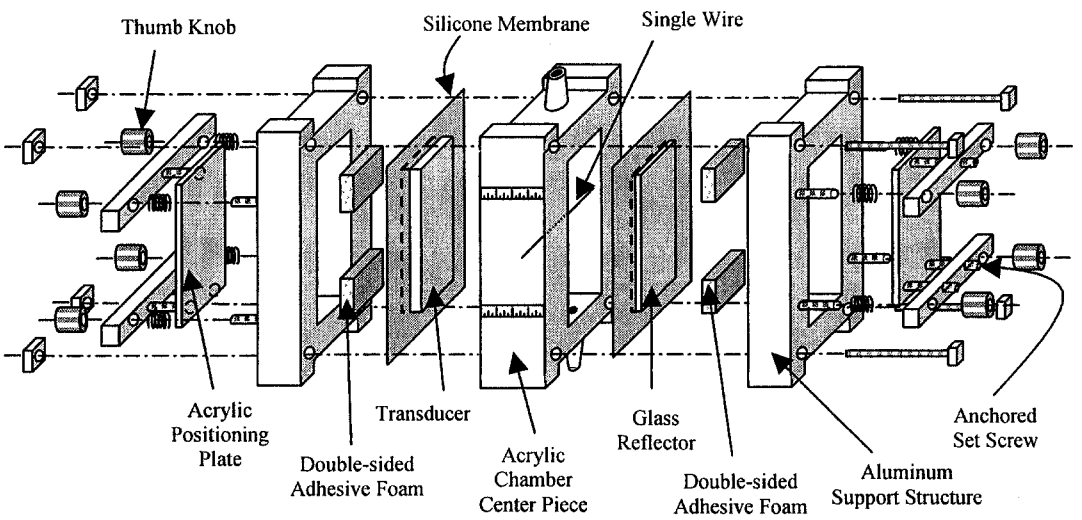

Figure 6.1: An expanded view of the chamber assembly.

6.2.1.2 Flow System

The suspension was transferred from a magnetically stirred flask to the chamber via a Masterflex peristaltic pump (model 7520-00), through ¼" diameter tubing. The flow rate was generally 30 mL/min (chosen to give close to a 1mm/s linear flow rate inside the chamber), and passed through a small volume (approximately 20 mL) hemispherical chamber in order to reduce flow oscillations. The suspension inside this chamber was stirred with a magnetic stirring bar. After passing through the pulse reducer, the suspension flowed into the acoustic device.

To produce a more uniform flow, a small piece of 10 pores per inch foam was placed just after the inlet inside the acoustic chamber. This distributed the flow more evenly through the remainder of the void space in the device (early experiments had

shown an uneven flow pattern). After the suspension passed through the chamber, it was recycled into the stirred feed flask.

6.2.1.3 Electronics

To power the transducer in the acoustic chamber, a Krohn-Hite 2100A signal generator was connected in series with a 50 dB EIN 240L RF power amplifier. A Clarke-Hess 2330 Sampling V-A-W instrument was used to measure the voltage across and current through the transducer. The chamber was operated at maximum power factor, indicating minimum power loss in the system. The power factor is the cosine of the phase difference between the applied voltage and the applied current; a value of one indicates no phase difference [38].

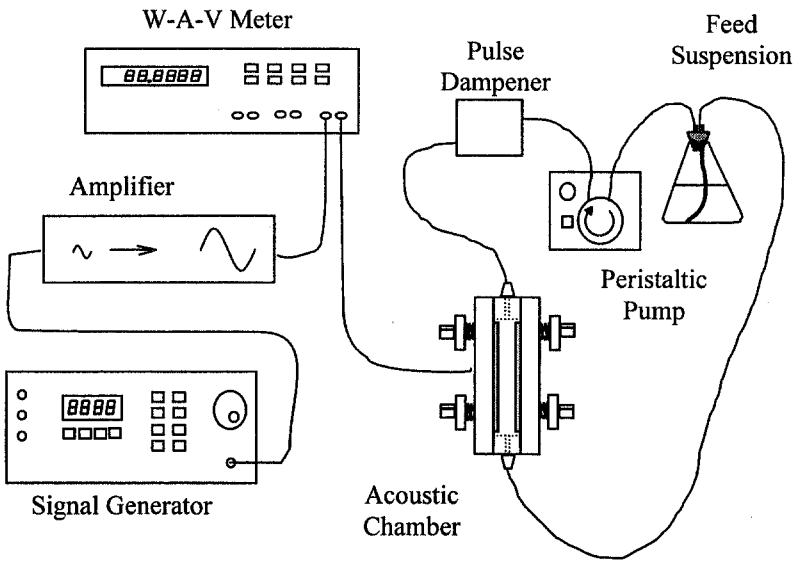

Figure 6.2: A schematic of the experimental setup

6.2.2 Video Imaging System

6.2.2.1 Camera and Illumination

Images were recorded by a 1024 x 1024, 30 fps UNIQ UP-930 digital video camera with a ½" progressive scan CCD sensor. In order to image an area of 5mm x 5mm with this camera, a Mirco Nikkor AF 60/2.8 lens was used, along with a set of spacers and a C-mount to F-mount adapter. The camera was mounted to a digitally controlled XYZ stage capable of measuring adjustments in position to 0.1 μm.

A 40 W halogen desk lamp was the illumination source for general viewing of the chamber, particularly during alignment of the transducer and reflector. For particle imaging, however, a Power Technology 532 nm 10 mW laser (model LCM-T-11 CCS) was used. The laser light passed through a 5 mm diameter, horizontally oriented glass rod, which created a vertical "light sheet" or laser plane. This plane passed through the glass reflector to illuminate a plane inside the chamber that had a normal along the wire axis. The laser needed to be cooled with a 100-mm-diameter AC fan to prevent overheating.

6.2.2.2 Video Capture Card and Software

Images from the camera were directly recorded into computer memory using an Epix Inc. PIXCI D2X interface card. The images were stored as 1024 x 1024, 10-bit grayscale tiff files. In order to capture images, a software program, XCAP Interactive Image Analysis 2.2, also supplied by Epix Inc., was run on an 800 MHz

Pentium III using Windows 2000. Besides controlling the capture and storage of the particle images, this program has tracking analysis tools that were used (see 6.4.1).

6.3 Procedure

To begin a particle tracking experiment, a 0.4 g/L suspension of polystyrene particles was produced by with 54 μm mean-diameter polystyrene particles to place in 500 mL of filtered (to 0.2 μm), deionized water. This particular concentration was chosen because it gave the best visibility of individual particles, while maximizing the total amount of visible particles in trial runs. The suspension was degassed with a simple vacuum pump in order to prevent any gas bubbles from interfering with particle visualization.

The acoustic chamber was assembled and connected to the flow system and the supporting electronics. After the fluid flow was established, a procedure was begun to align the transducer and reflector to be parallel. The distance between the transducer and glass reflector was measured and adjusted at each of the four corners using translation of the XYZ stage on which the camera was mounted. This process was continued until the measurements were within 0.1 mm of each other. A normal value for this spacing was around 9 mm. Also, the transducer and reflector were measured to be exactly vertical, to 0.1 mm, so that it was assured that the wire axis was perpendicular to the acoustic field.

Once the alignment was complete, the camera was positioned to view the wire in the center of the image; the wire axis was perpendicular to the image plane so that

the wire appeared as a disc. The laser was switched on and the camera was focused on the light plane, which shined on the midpoint of the wire length.

To find a resonant frequency, the transducer was powered with a 150 mV sine wave from the signal generator, resulting in the application of 1.6 Watts rms across the transducer electrodes. The experiments were performed at this power level because a higher level caused an unacceptable amount of buoyancy flow (see below) and lower power did not produce sufficient line-up of particles.

The frequency was varied manually from a starting point of the calculated optimum resonant frequency of the chamber [39]. Once a frequency was found that maximized the power factor, i.e. minimized the losses in the system, the power to the transducer was disconnected. A small amount of heat was generated at the transducer surface, so to minimize the impact of convective flow, the transducer was only operated for brief periods. After more than 15 seconds, fluid heated by the transducer would begin to flow upward; this buoyancy flow disrupted the steady fluid flow pattern.

Video was recorded digitally at 10 frames per second for a period of 12 seconds at a time. The linear flow rate in the chamber was near 0.5 mm/s, so images of the same particle would nominally be spaced 0.05 mm from frame to frame. This has proved to be sufficient for particle tracking analysis (see 6.4). At 2-3 seconds into the recording period, the sound field was activated. The particles responded to the acoustic field, establishing a steady trajectory pattern in less than one second. After about 6-8 seconds, depending on the power supplied to the transducer, heat

from the transducer surface caused convective flow to disrupt the flow profile. This is visualized by a swirling motion of the particles flowing with the fluid.

6.4 Particle Trajectory Analysis

6.4.1 Particle Tracking

The XCAP Interactive Image Analysis software package has the capability to track particles from frame to frame and output this positioning data. The first step is to identify individual particles in each frame. After this, adjacent frames are compared to find the particle image pairs, i.e., particle positions are analyzed to determine which image in the second frame corresponds to the same particle in the first frame. In each step of the analysis process, there are many parameters to adjust; only certain combinations of these parameters lead to proper identification of particle paths. Fine tuning the analysis is time consuming, but is essential to obtaining useful data from the video images.

When analyzing images from particle flow experiments, the first step was to identify particles on each video frame. The process of segmentation, where the image is modified to enhance particle identification, was used to aid this identification. The original image is 10-bit grayscale, but after segmentation is strictly black and white, with black as the background, and white as possible particles.

In the visual experiment, particles were brighter than the background; this served as the primary identification tool. A certain grayscale value was chosen such that anything darker was considered to be background (black) and anything lighter

was converted to white. In most cases, a sufficient value for the grayscale threshold was 60% (in terms of black intensity).

A few other techniques were used in the segmentation process. These image adjustments were applied in a sequence, beginning with erosion, removing bits of the image that were only a few white pixels. Following erosion, dilation and closing were applied; the former was used to increase the size of particle blobs present on the image and the latter filled in any holes or irregularities in the blobs. Figure 6.3 shows a typical image before and after segmentation. In order to aid visualization in print, the images are negative of those obtained in the experiment. The wire is the disc in the center of the image, while the particles are the small black blobs.

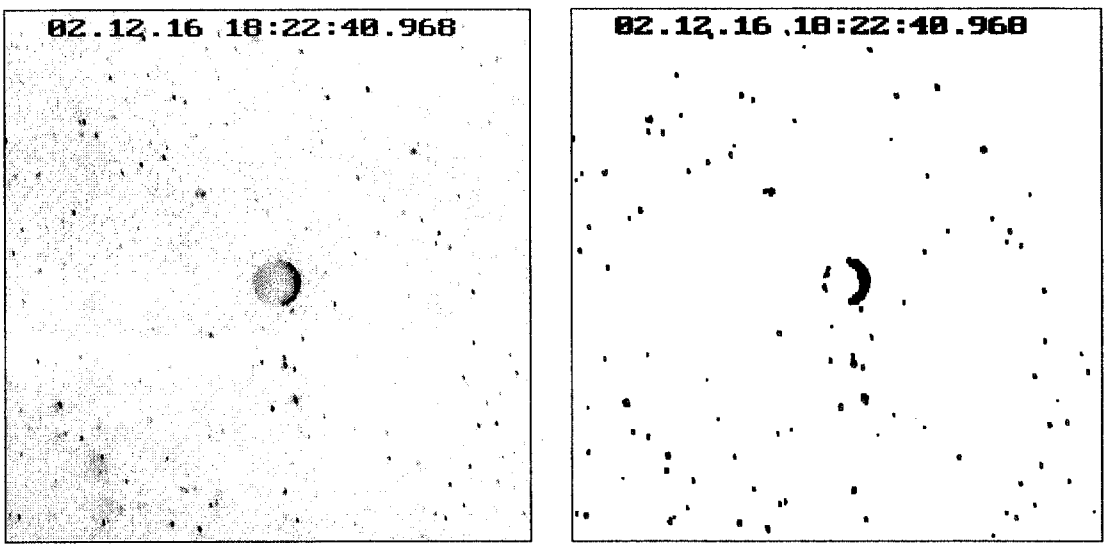

Figure 6.3: A typical experimental image before (a) and after (b) segmentation. These images are negative of actual images to aid visualization in print. The disc in the center of the images is the wire (in which the axis is coming out of the page) and the small black blobs are particle images.

The next consideration was size of the particle "blobs" on the image. Upper and lower limits for size were chosen to narrow the identification even further. For example, the wire itself may have been identified as a particle if the size restriction was not applied. These limits are manifested in terms of blob area, width, and height.

After particles were identified, the positions were recorded automatically by the XCAP software and analyzed to determine trajectories. Another set of parameters aided in this analysis, including, but not limited to, expected vector magnitude (in terms of pixels per image) and expected range of vector direction; these estimates were input into XCAP. The algorithm used fuzzy logic to track particles from image to image. These trajectories were recorded as positions of a single particle in consecutive frames. Experimental trajectory results are compared to model calculations in Section 7 of this document.

Certain limitations of this analysis, due to the experiment and the software, were immediately evident. If the particle disappears from the segmented image for any reason, the tracking information is lost. In other words, the software is limited to only produce particle trajectories if the particle is present in each and every frame that is analyzed. About 5% of the particles recorded by the software were not present on a subsequent frame.

Some physical reasons that identified particles disappeared include that the laser light sheet was blocked by the presence of the wire, creating a shadow on one side of the image where particles disappeared. So no trajectories could cross this region. Also, if a particle flows in and out of the image plane illuminated by the laser

sheet, that particle track will not be recorded. Even if the particle simply flows out of the video frame within the plane of illumination, the trajectory is abandoned. This latter case was avoided by restricting the range of images to be analyzed to be less than the typical residence time of a particle in the video sequence. But even with this restriction, multiple ranges of frames had to be chosen to find paths of additional particles.

Besides the above physical reasons, limitations of the analysis also contributed to identified-particle disappearance on subsequent frames. For example, if a particle came too close to another, the "blob" was recognized as one particle.

6.4.2 Cross-Correlation Vector Plots

Instead of tracking individual particles, the entire flow field can be analyzed at once, producing a vector field of particle velocities. This field may be averaged over a range of video images. This technique is commonly called particle image velocimetry, or PIV.

In general, PIV is used to measure fluid flow; a liquid or gas is seeded with small particles and images are analyzed in order to determine the flow field of the fluid in a given geometry. The seed particles must be small so that the particles follow the fluid. In this experiment, however, the particle vector field is the desired result. So the analysis is the same with one less constraint, i.e., the necessity to match fluid flow with particle flow. In fact, in this case, the particles are definitely *not* following the flow because of the acoustic forces present.

Vector plots of the particle velocities were created using PIVPROC, a software program written by Mark Wernet of NASA Glenn Research Center. The software analysis involved a technique where video image pairs were compared using cross-correlation. In this process, images were broken into small subregions. Each subregion was compared to the same area in the subsequent video frame to determine the average particle displacement of the subregion. The result was a velocity vector for each subregion of the video image; when these vectors were assembled, a particle velocity field for the area surrounding the wire was obtained. Vector plots of experiments are shown in Section 7.3.

7 Comparison of Experimental Data and Trajectory Model Results

7.1 Introduction

The purpose of the experiments described in Section 6 was to verify the applicability of the model presented in Section 4. There were fundamental differences, however, between the configuration for which the model was derived and the actual experimental system. These differences were necessary in order to design an experiment that allowed visualization of particle trajectories in an acoustic separations system.

One of the major differences was that of scale. The elements in the typical polyester foam used for separation experiments were one third the size of the wire that was utilized for the single-fiber experiments. Also, the particles in the single-fiber experiment were two times the size of those typically used in the filtration processes. At the same time, the sound frequency for both systems remained the same, so the relative effect of the acoustic field in each case may be dissimilar.

Another key difference between the filtration experiments and the single-fiber experiment was the composition of the fiber, polyester in the former and stainless steel in the latter. These two materials have different acoustic properties and could affect the acoustic field, and therefore the particle paths, in different ways.

With that said, qualitative comparisons between the single-fiber experiments and the model results presented in Section 5 may be made, but a direct comparison to experimental conditions requires that the parameters of the model reflect those of the single-fiber experiment. So in this section, the experimental results are discussed

along with model simulations of the relative system. Most of the comparisons here will be qualitative, based on visual observation, but a quantitative analysis is also used to show the sensitivity of some model parameters.

7.2 Particle Trajectories

7.2.1 Model Parameters

The physical parameters for the single-fiber system are shown in Table 7.1. The energy density inside the chamber was calculated using a model of a resonant ultrasonic wave traveling through a layered system [39]. This energy density model included attenuation and has been verified experimentally within a similar chamber [39]. These parameters resulted in a Re_c of 0.39, and 0.81 for the value of the Gor'kov number, *Gk*.

The approach speed of the fluid was measured by focusing the camera at a point far away from the wire and measuring particle velocities (with no active acoustic field). Also at this point, the acoustic field was activated in order to measure the position of the pressure nodal planes, assumed to be the locations where the particles were aligned.

The model used for the comparison studies in this section is identical to the one described in Section 4 with one exception. In this case gravity was added to the calculation. This adds an extra term to the force balance (Eq. (4.1)).

$$\mathbf{F}_{ac} + \mathbf{F}_D + \mathbf{F}_G = \mathbf{0} \tag{7.1}$$

The buoyancy force due to gravity, $\mathbf{F}_G$, is defined by Eq. (7.2).

$$\mathbf{F}_G = \frac{4}{3}\pi R_p^{\,3}\left(\rho_f - \rho_p\right)\mathbf{g} \tag{7.2}$$

Table 7.1: Physical properties of the single-fiber experiment.

Acoustic field	
Energy density (E_{ac})	0.27 J/m^3
Frequency ($\omega/2\pi$)	680.2 kHz
Fluid: pure water	
Bulk velocity (U_f)	0.65 mm/s
viscosity (μ)	0.001 kg/m s
density (ρ_f)	1000 kg/m^3
longitudinal sound speed (c_f)	1480 m/s
Filter element: stainless steel	
radius (R_c)	0.3 mm
density (ρ_c)	7900 kg/m^3
longitudinal sound speed (c_1)	5790 m/s
shear sound speed (c_2)	3100 m/s
Particles: polystyrene	
Radius (R_p)	27 μm
Density (ρ_p)	1050 kg/m^3

7.2.2 Comparison Metric

In order to compare an experimental particle trajectory to one simulated in the model, a simple quantitative technique was devised that involved calculation of the area between a predicted and an observed particle path. This area is calculated by integrating the absolute difference in y-direction between the predicted and observed trajectory at each experimental x value. This comparison is not sufficient to label a single fit as "good" or "bad", but gives an indication of a "better" or "worse" fit when

adjusting model parameters. When the area between the model and experimental trajectories decreases, it is assumed that the model is providing a better reproduction of the experimental system.

7.2.3 Experimental and Model Results

7.2.3.1 Particle Flow with No Acoustic Forces

To establish that the single-fiber model adequately described the flow in the absence of acoustic forces, some experimental trajectories were compared to simulated ones for this case. Plots of two such particle paths are shown in Figure 7.1 and Figure 7.2. Experimental trajectories closely matched model predictions, although the observed data seemed slightly shifted in the flow direction. This may have been due to error in the coordinate system definition for that particular particle tracking experiment. After ensuring validity for a Gor'kov number of zero, results from experiments with an active acoustic field were examined.

7.2.3.2 No Parameter Adjustments

Without fitting any of the model parameters to the experiment, sets of model trajectories and experimental trajectories subjected to an acoustic field were plotted. Three of these sets of trajectories are shown in Figure 7.3, Figure 7.4, and Figure 7.5 (with one experimentally measured particle path per plot); for identification purposes, the experimental trajectories shall be referred as A, B and C in the remainder of this chapter.

In each figure, the black circle represents the cross-section of the wire in the experiment. The blue lines indicate the pressure nodes of the incident acoustic wave. Indicating particle position in the experiment, the red dots are results from the particle trajectory analysis described in Section 6.4.1. The closely spaced green dots, which on most plots may be indiscernible from a green line, represent the calculated path of the particle using the model with the parameters listed in Table 7.1. The units in the plots are dimensionless, with distances scaled to the radius of the wire (1 radius = 0.3 mm).

Experimental trajectories A, B, and C, were chosen to show typical particle paths. In A and B, each particle, although originating at a unique location, collides with and sticks to the same point on the wire in the experiment. The path of C remains about five radii from wire throughout its appearance in the frame.

The model calculations seem to match the experimental trajectories quite well, i.e., the green line follows the same general path as the red dots in Figure 7.3, Figure 7.4, and Figure 7.5. But the curvature in each case does not compare well, the predicted paths are more flat while observed trajectories show more movement in the y-direction. Even more importantly, however, the model does not predict collision with the wire in A and B.

The model includes the incident plane wave and the acoustic wave reflected from the cylinder in the potential used to calculate the acoustic force on a particle. The program interface allows the user to select whether to calculate the forces due to

the incident wave, reflected wave, or both. The simulations described thus far have included both. Without the incident wave, the acoustic potential (Eq. (4.23)) is

$$\Phi = A\exp(i\omega t)\sum_{n=0}^{\infty} B_n d_n H_n^{(2)}(v)\cos(n\theta)\,. \tag{7.3}$$

Using only the reflected wave in the acoustic force calculation shows drastic improvement in the match between simulation and experiment in Figure 7.6, Figure 7.7, and Figure 7.8. Although not identical, the curvatures of the experiment and model more closely match in each of A, B and C. Also, (and again most importantly) A and B are predicted by the model to collide with the wire. It must be re-emphasized here that these are pure model predictions without parameter adjustment; the agreement with experimental trajectories is quite remarkable with that in mind.

The above result may signify that the reflected wave has more of an effect than the incident wave near the cylinder. Also, the rigid wire may have blocked or distorted the incident field, decreasing its effect on particle paths.

When the area between experimental and simulated trajectories is compared, another trend is shown. When both incident and reflected waves are included, A, B, and C, have areas of 0.71, 0.62, and 9.07, respectively, while excluding the incident plane wave increases each area slightly to 1.16, 1.14 and 9.63. (The range of integration for C was more than double that of A and B, which contributed to the larger calculated area in that case.) These differences in area are small, and capture prediction is considered more important; it is capture prediction that forms the basis of a more integrated model in Section 8.

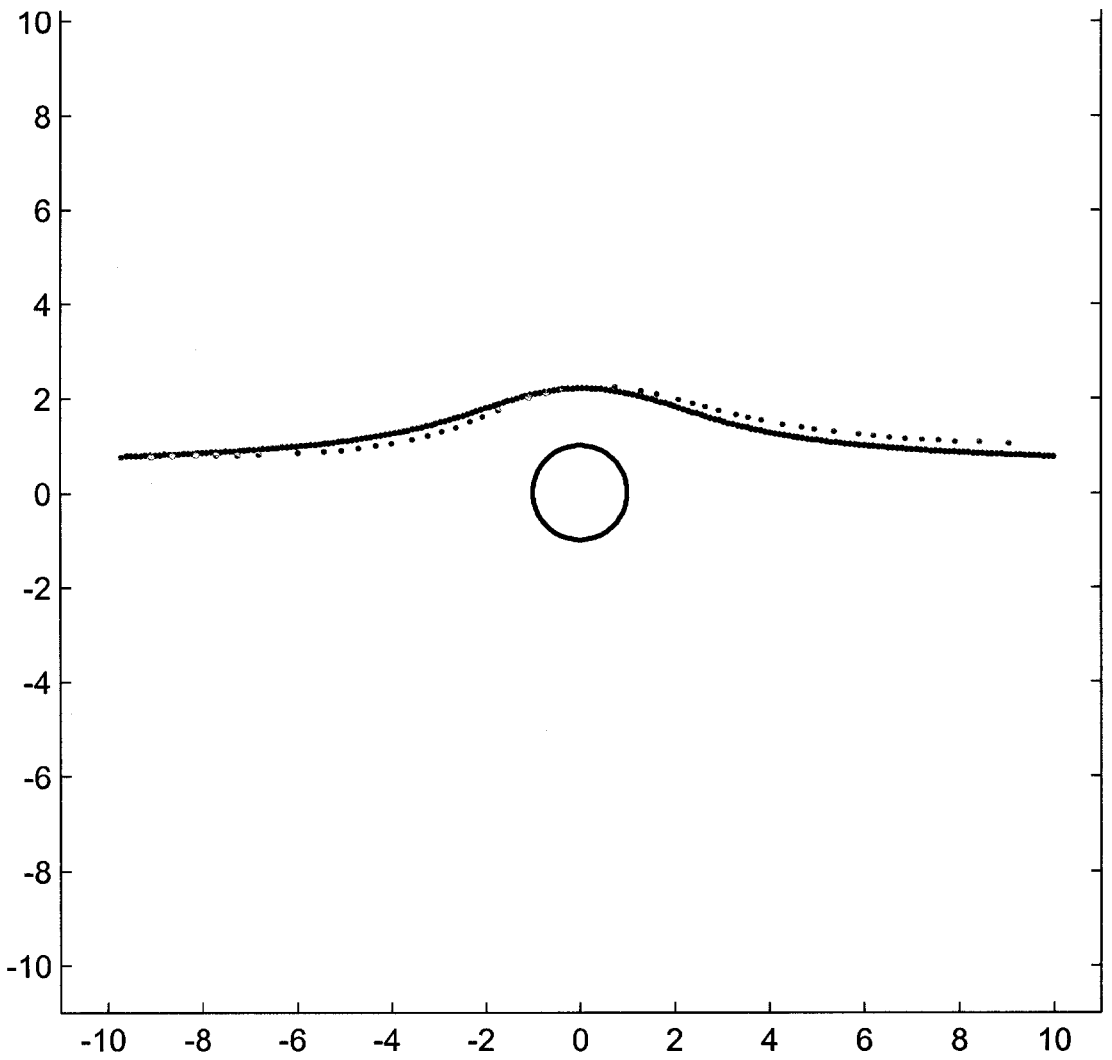

Figure 7.1: Without acoustic forces, the model predicts a particle trajectory (green) that closely matches experimental data (red). The circle in the center of the plot is a cross-section of the wire, the units of the plot are dimensionless, scaled to the radius of the wire.

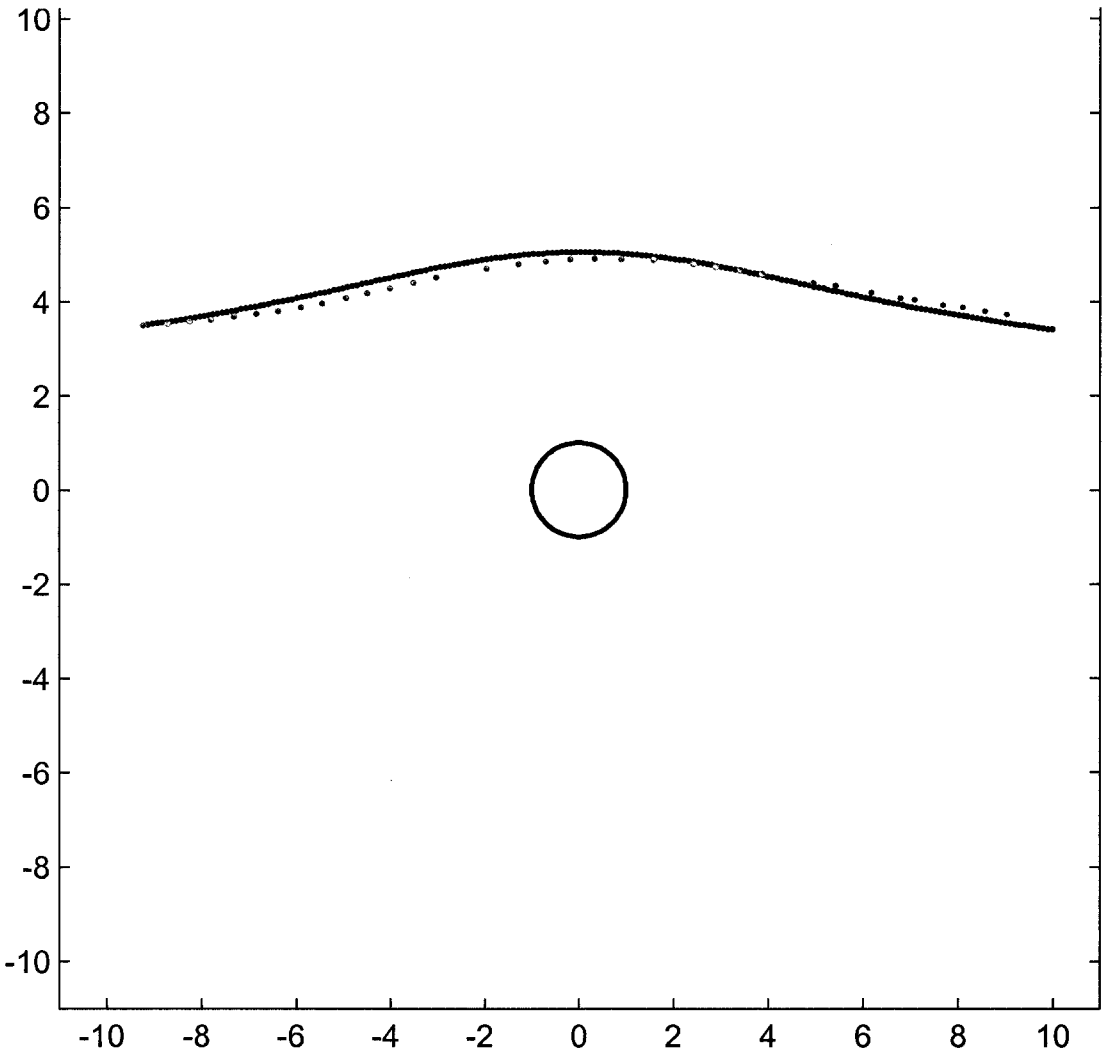

Figure 7.2: Another particle trajectory in the absence of acoustic forces. The particle in this plot travels in a path farther from the wire than the one in Figure 7.1.

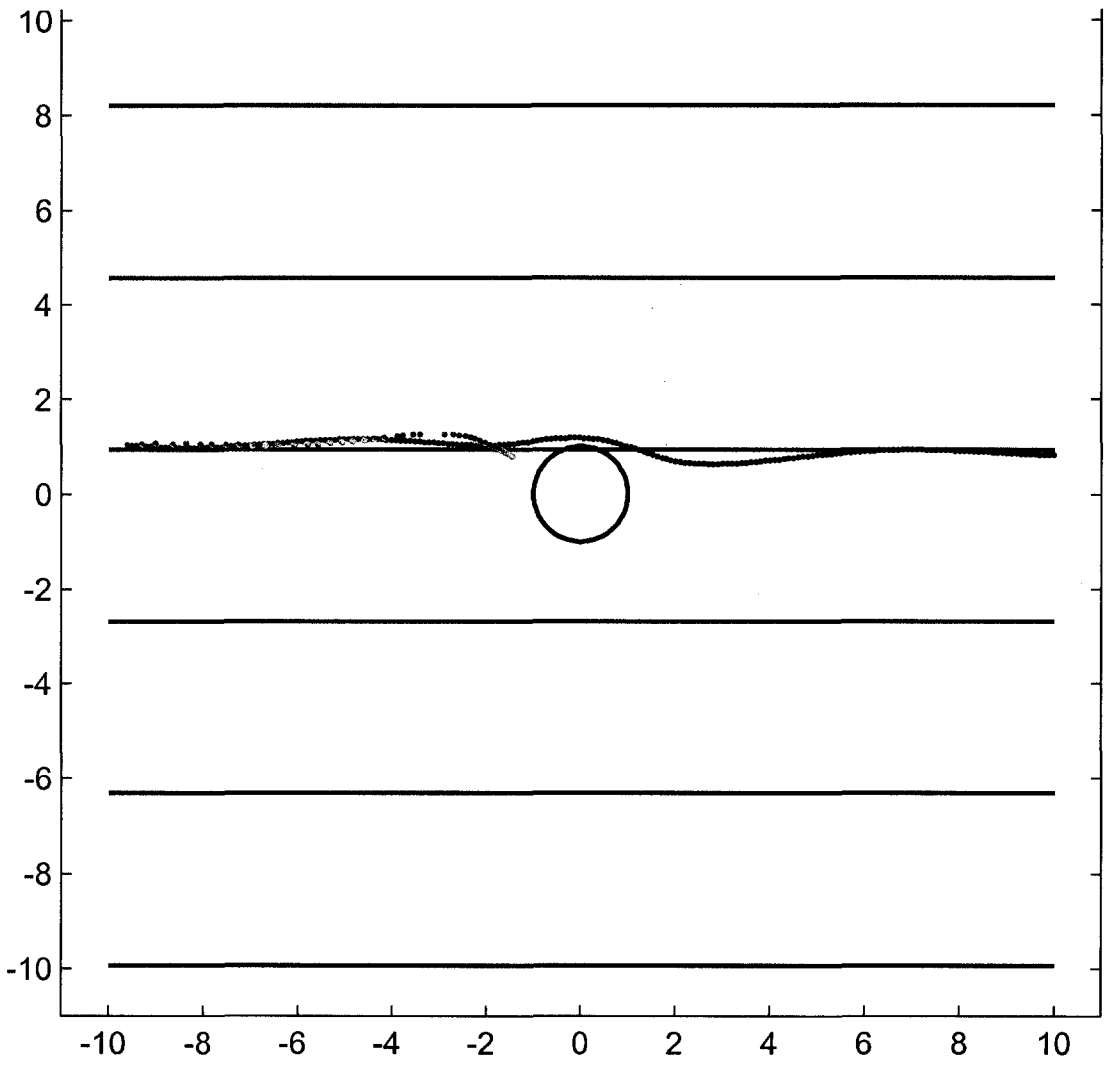

Figure 7.3: A plot of an experimentally measured particle trajectory (red dots) along with a simulated one (green line). The blue lines indicate the pressure nodes of the incident plane wave and the circle in the center is the cross-section of the wire. The units of the plot are dimensionless, scaled to the radius of the wire (1 radius = 0.3 mm). For ease in identification, the experimental trajectory shown here is referred to in the text as trajectory A. The simulated particle path follows close to the experimental one in this case, but is not predicted to collide with the cylinder. In the experiment, the particle does indeed collide with and stick to the wire, but in the trajectory analyses, the last few particle positions were not recorded due to particle clumping occurring at that point on the wire. The area between the two trajectories is 0.71.

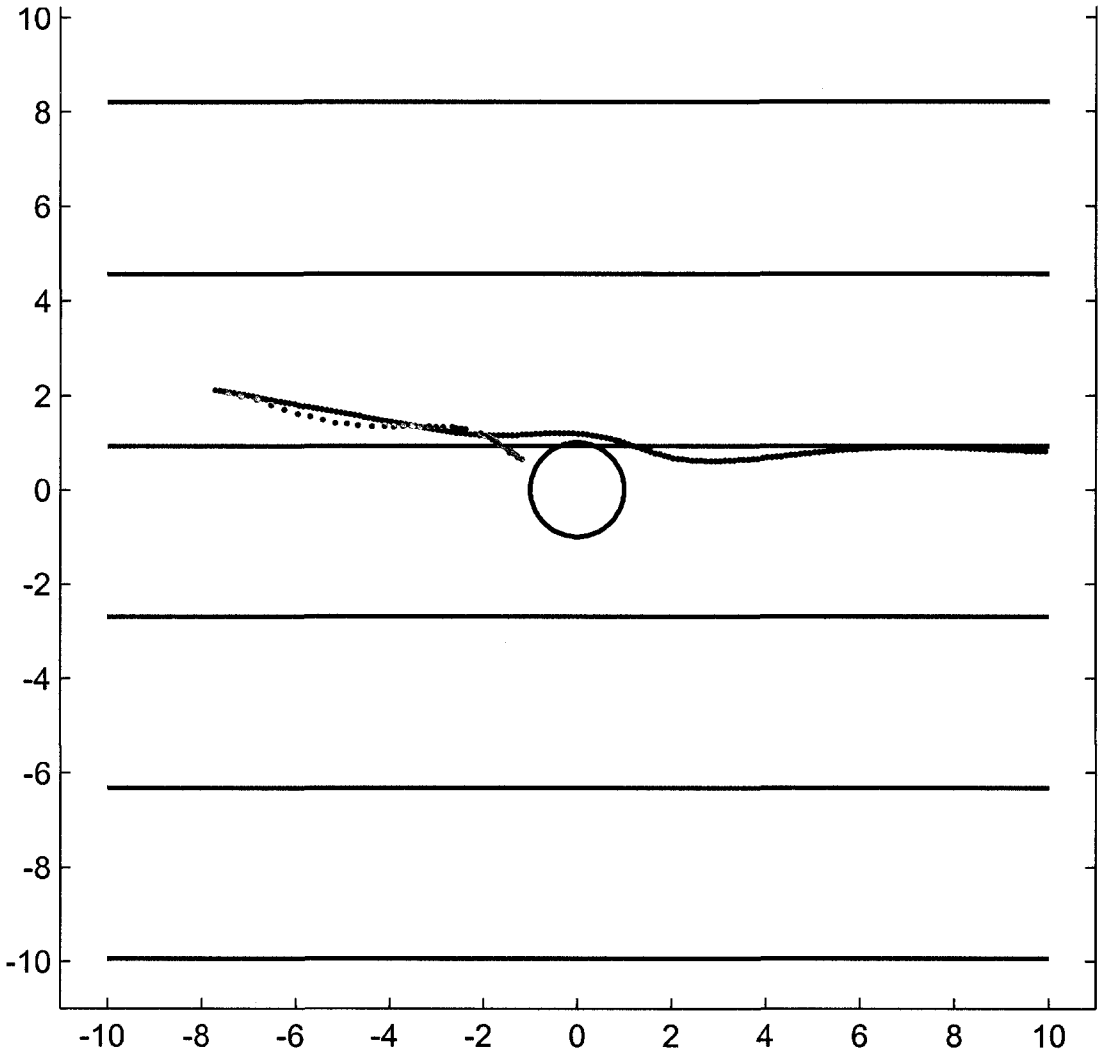

Figure 7.4: Another experimentally determined particle trajectory, referred to as B in the text, shown with a simulated one. Again, in this case the particle collides with the wire in the experiment, but according to the model, should flow around it. The area between the two trajectories is 0.62.

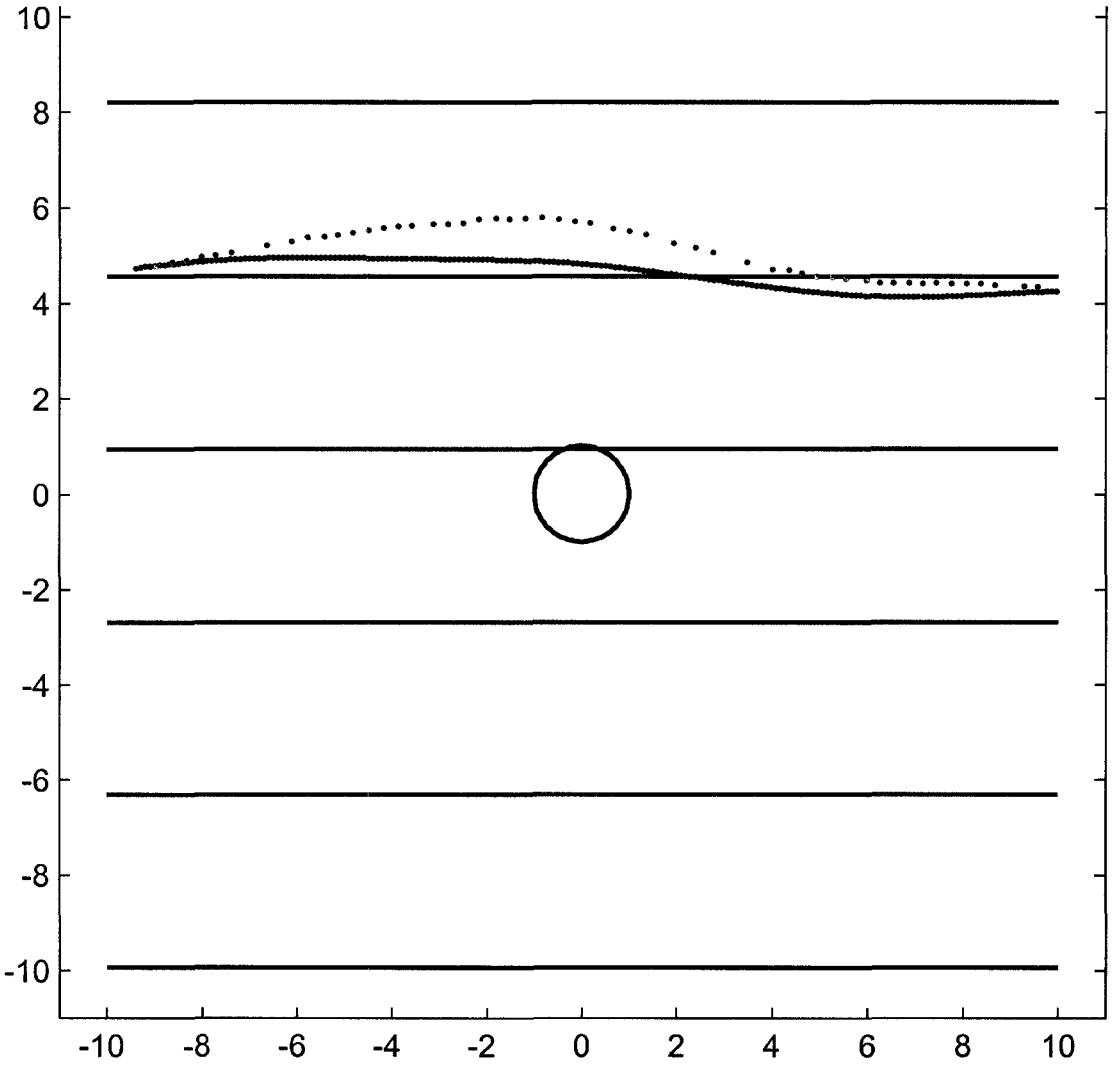

Figure 7.5: This experimental trajectory, referred to as C in the text, remains 4 to five radii from the wire. The simulated trajectory in this case has less curvature than the experimental path. The area between the two trajectories is 9.07.

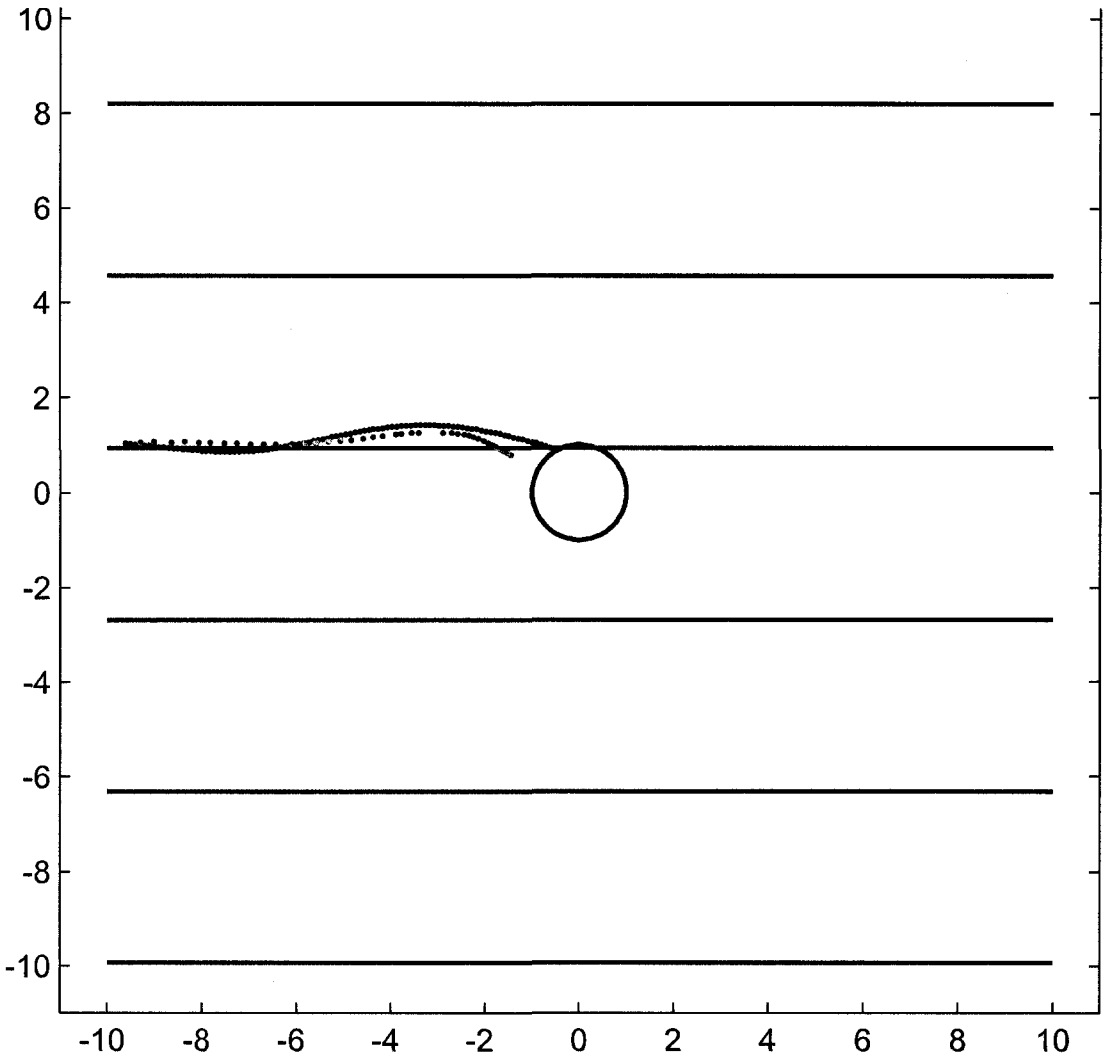

Figure 7.6: When only the acoustic wave reflected from the cylinder is used for acoustic force calculations, the simulated particle trajectory, more closely matches the curvature of A (from Figure 7.3). More importantly, the particle is now predicted to collide with the wire. The area between the two trajectories is now slightly larger compared to Figure 7.3, at1.16.

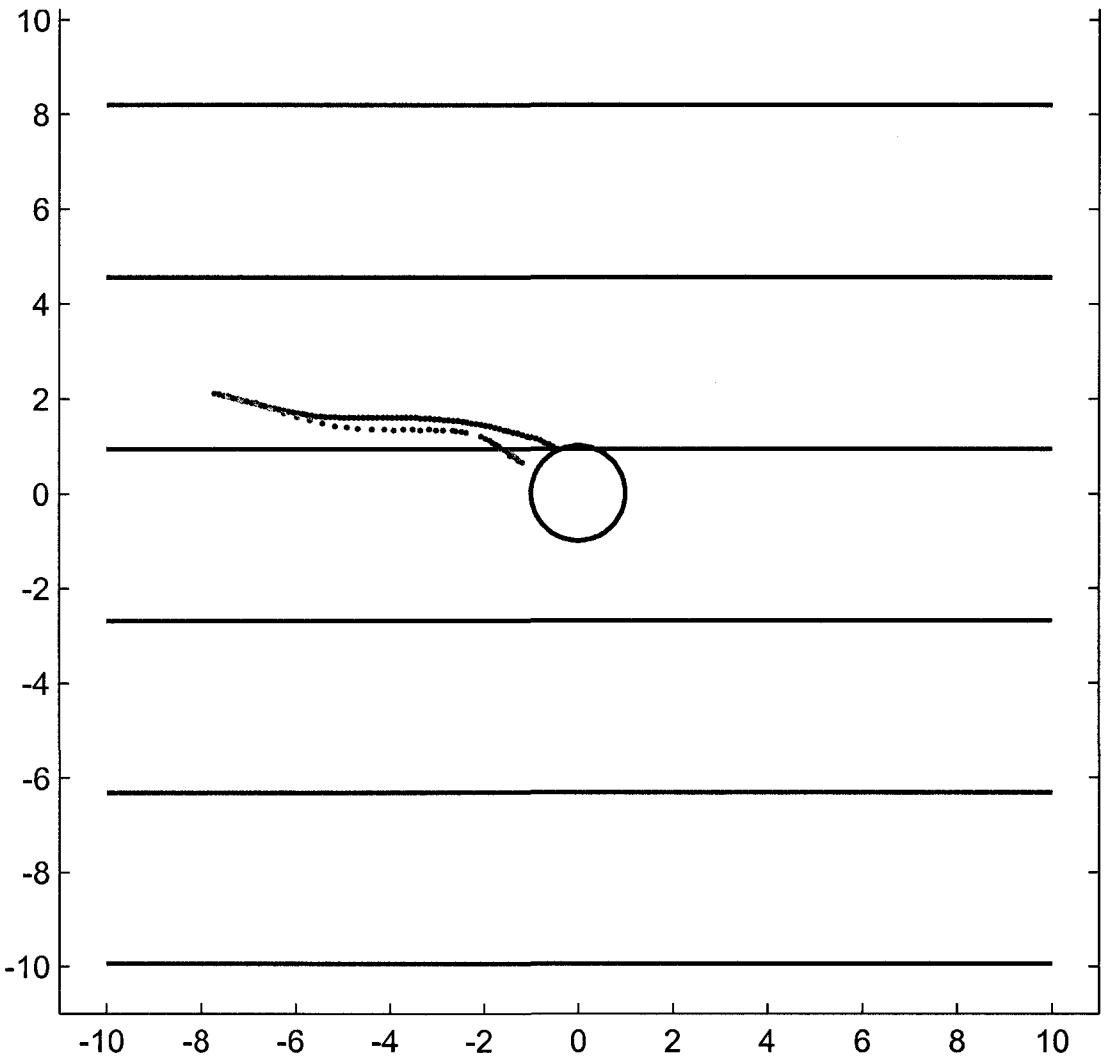

Figure 7.7: This plot shows the experimental trajectory B from Figure 7.4 along with simulation results where only the reflected wave is considered. As in the case for A, here the trajectory is predicted to collide with the wire, but the area between the two trajectories is slightly larger than in Figure 7.4, at 1.14.

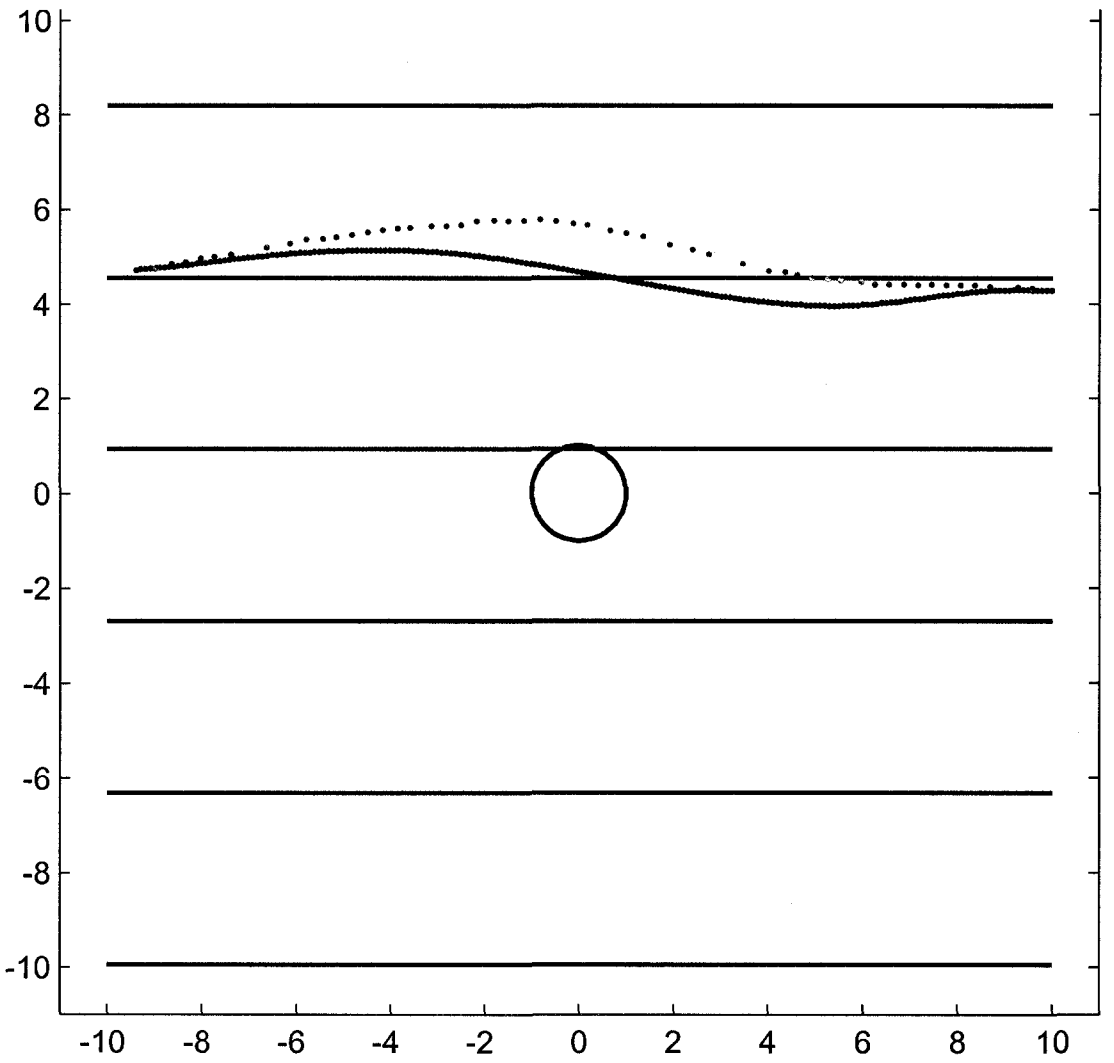

Figure 7.8: Trajectory C from Figure 7.5 is again depicted, along with simulation results that do not consider the incident plane wave in the acoustic forces. The curvature of the model trajectory is more pronounced in this case (and thus more similar to the experiment than Figure 7.5), but does not closely track the experimental model trajectory. The area between the two trajectories is 9.63.

7.2.3.3 Adjusting the Gor'kov Number

Since the Gor'kov number is a lumped parameter that indicates the effect of acoustic forces relative to flow forces, one would expect that alteration of the dimensionless number would profoundly change the calculated particle path in the single-fiber model. This is indeed the case, as *Gk* may be adjusted in order to allow the model data to more accurately predict the experimental particle trajectories.

In A, B, and C, the Gor'kov number was changed from the computed value of 0.81 in order to fit the data better, i.e., to decrease the area between the model trajectory and the experimental one. This resulted 1.10, 1.04, and 0.29, for *Gk* in A, B, and C, respectively, and gave improved model-experiment comparison areas of 1.00, 0.46, and 1.72. Plots of these results are shown in Figure 7.9, Figure 7.10, and Figure 7.11.

The acoustic energy density was increased to nearly the same value in A and B to provide a better fit, but decreased to allow the data to fit C well. Firstly, the fact that *Gk* needed to be changed may indicate that the original value (based on the acoustic energy density inside the chamber predicted in a model by Rusinko [39]) is not perfect. To put this in perspective, the original acoustic energy density used in the no-parameter fit was 0.25 J/m^3. The adjusted values for A, B, and C, were 0.34, 0.32, and 0.09 J/m^3, respectively. These values are of the same order of magnitude as the original value.

Two possible explanations of the above phenomena are possible with a more thorough understanding of the experimental conditions. Trajectories A and B were

taken from the same set of images, while, C was taken from a different experiment. Since A and B had nearly the same corrected energy density, it is possible that an experimental inconsistency, such as temperature fluctuation could have changed the energy density (by altering the resonant frequency slightly) inside the chamber.

Another explanation is that the single-fiber model does not properly predict the decreasing effectiveness of the acoustic field as the position of the particle is farther from the wire. Trajectories A and B were much closer to the wire than C.

In order to determine which of these scenarios is more likely, a trajectory from the same experiment as A and B, but farther from the wire, was examined. This trajectory (here fore referred to as D) is shown in Figure 7.12 along with the simulated trajectory using the original *Gk* of 0.81, and again in Figure 7.13 with the simulated trajectory using a best fit value for *Gk* of 0.065. This follows the same trend as trajectory C did, although in C, the value of *Gk* was only decreased to 0.29.

To make another comparison, a trajectory from the same experiment as C, but that passed closer to the wire, was analyzed. The plots of this trajectory (here fore referred to as E) with simulated particle paths are depicted in Figure 7.14 and Figure 7.15. The best fit for E was found by increasing the value of *Gk* to 1.30. Again, this follows the same trend as A and B, i.e., for these trajectories near the wire, the effect of the acoustic field in the model needed to be increased in order for it to match the experiment.

A summary of the parameter values and areas between trajectories is given in Table 7.2. From the preceding analysis, it is likely that the model does not adequately

account for the decreasing effect of the acoustic field as distance from the wire increases. The modeled effect of the acoustic field needed to be decreased significantly in the two trajectories that were far from the wire (C and D) in order to fit the experimental particle paths, but also needed to be increased by as much as 60% to match A, B, and E, which traveled more closely to the cylinder.

Table 7.2: Parameters and results of experimental-model comparisons. The starting position is the value of y (i.e., the vertical distance from the axis of the wire) in the plot at the initial point of the experimentally measured particle trajectory. Both *Gk* and area are dimensionless.

Experimental trajectory	***Starting position***	***Incident and Reflected wave***		***Reflected wave only***		***Best fit, only reflected wave***	
	y	*Gk*	*Area*	*Gk*	*Area*	*Gk*	*Area*
A *(experiment #1)*	1.0	0.81	0.71	0.81	1.16	1.10	1.00
B *(experiment #1)*	2.1	0.81	0.62	0.81	1.14	1.04	0.46
C *(experiment #2)*	4.7	0.81	9.07	0.81	9.63	0.29	1.72
D *(experiment #1)*	3.6			0.81	11.0	0.065	5.38
E *(experiment #2)*	0.0			0.81	1.69	1.30	1.42

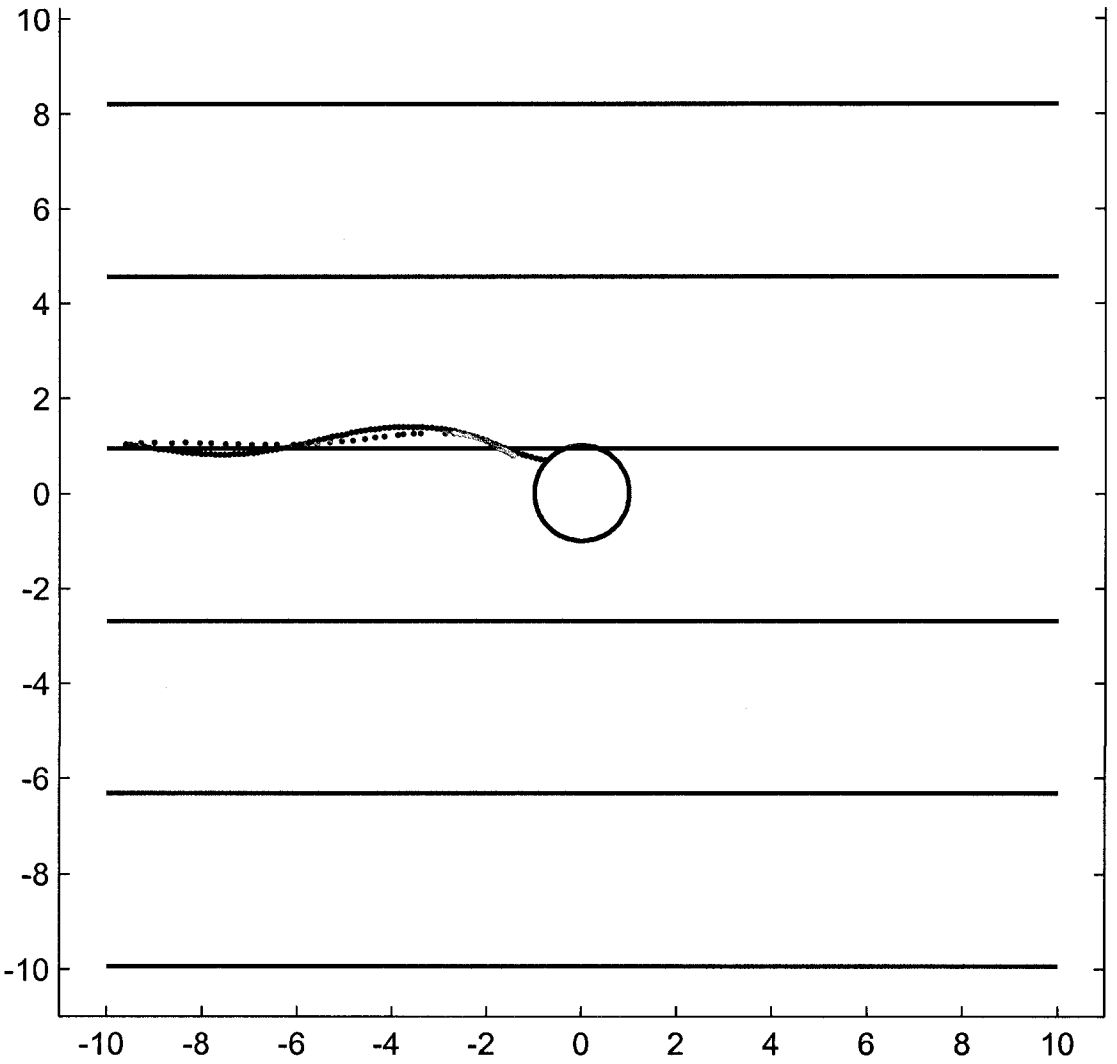

Figure 7.9: An improved fit for trajectory A was found by increasing *Gk* from 0.81 to 1.10, which decreased the area between trajectories to 1.00.

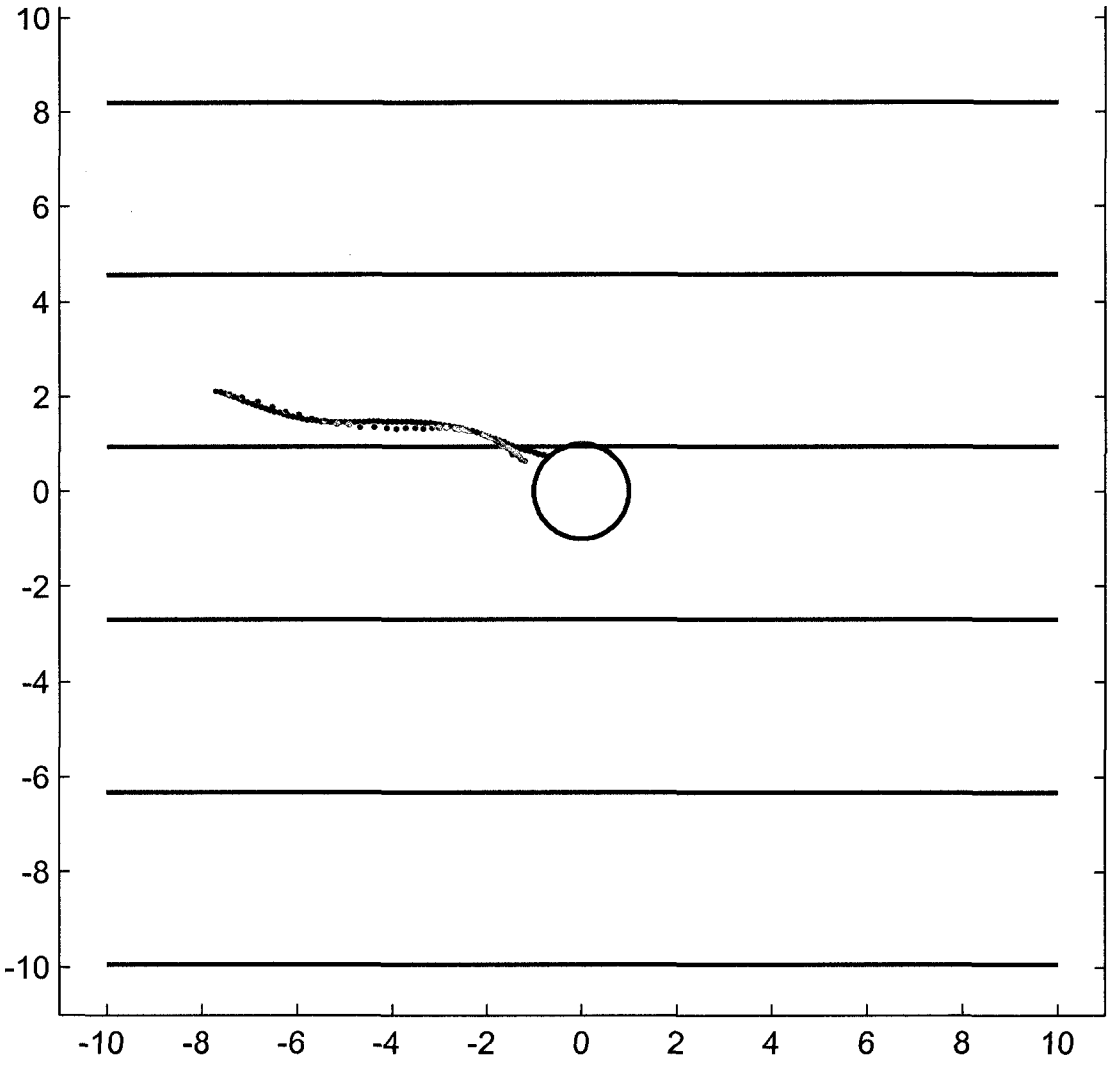

Figure 7.10: An improved fit for trajectory B was found by increasing *Gk* from 0.81 to 1.04, which decreased the area between trajectories to 0.46.

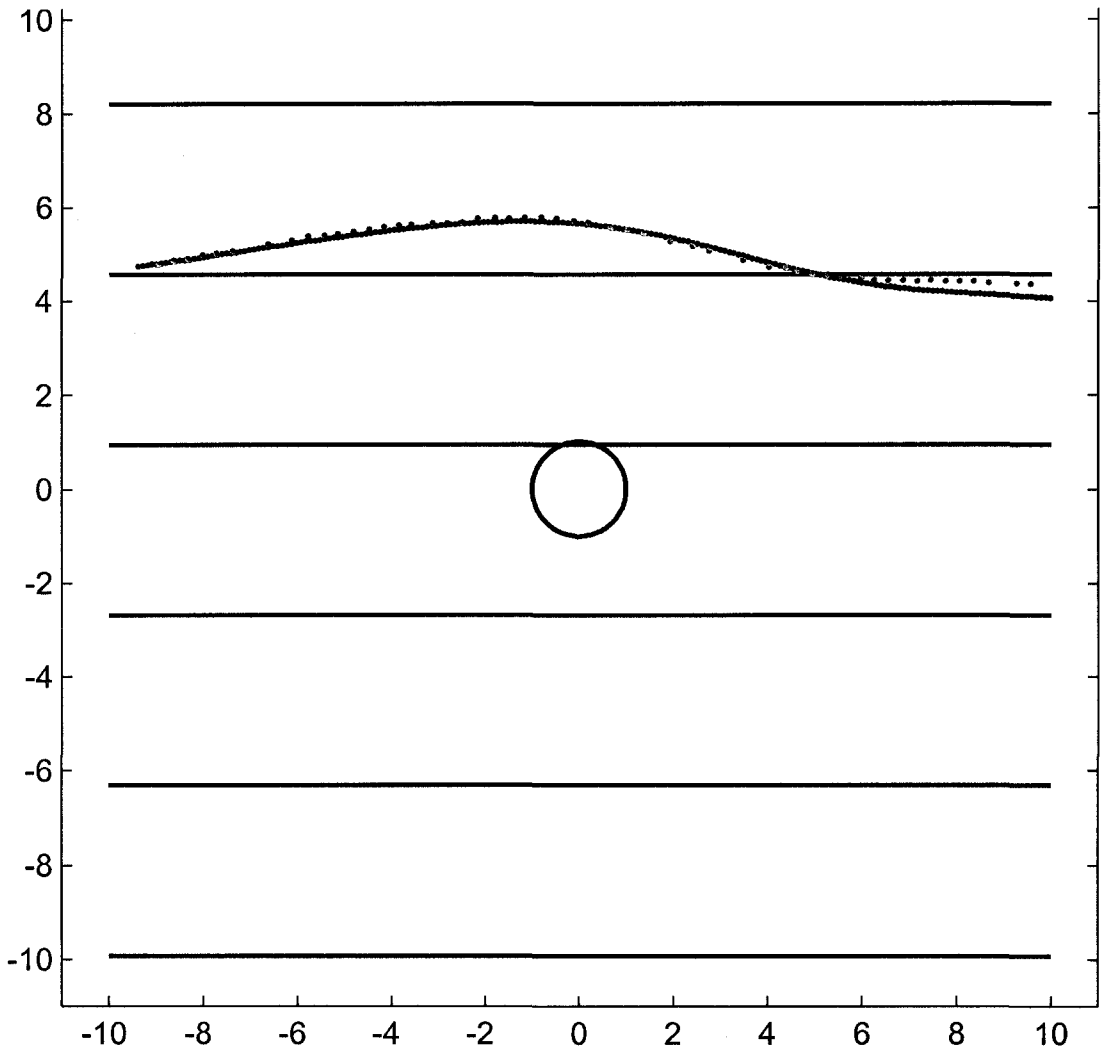

Figure 7.11: An improved fit for trajectory C was found by decreasing *Gk* from 0.81 to 0.29, which decreased the area between trajectories to 1.72 (from 9.63 in Figure 7.8).

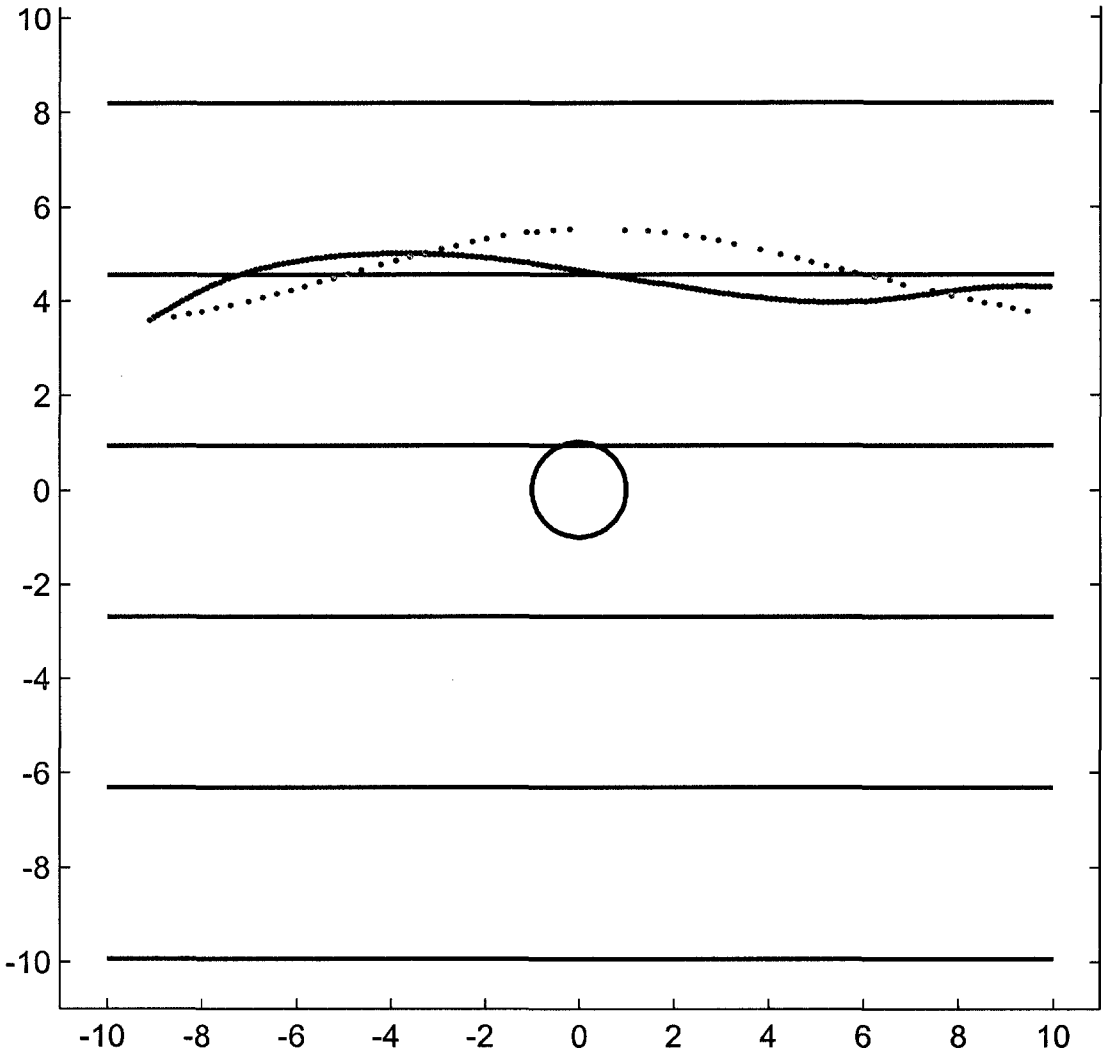

Figure 7.12: An additional trajectory (referred to as D in the text) from the same experiment as A and B, but in this case the particle is farther from the wire. The area between the model and the experimental paths for this case of $Gk = 0.81$ is 11.0.

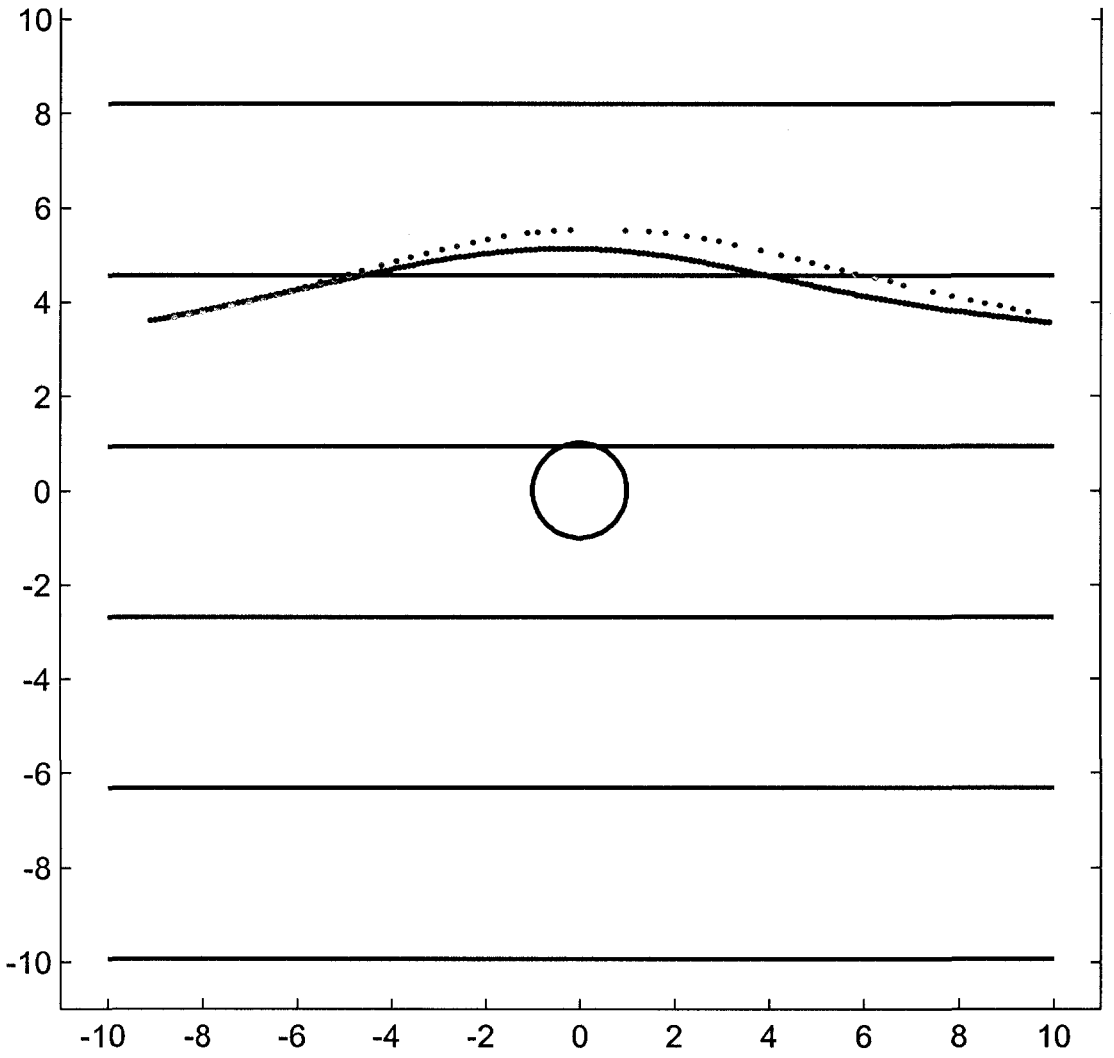

Figure 7.13: Trajectory D is shown again with a best fit of $Gk = 0.065$, decreased significantly from the original parameter value. The area between the trajectories is 5.38.

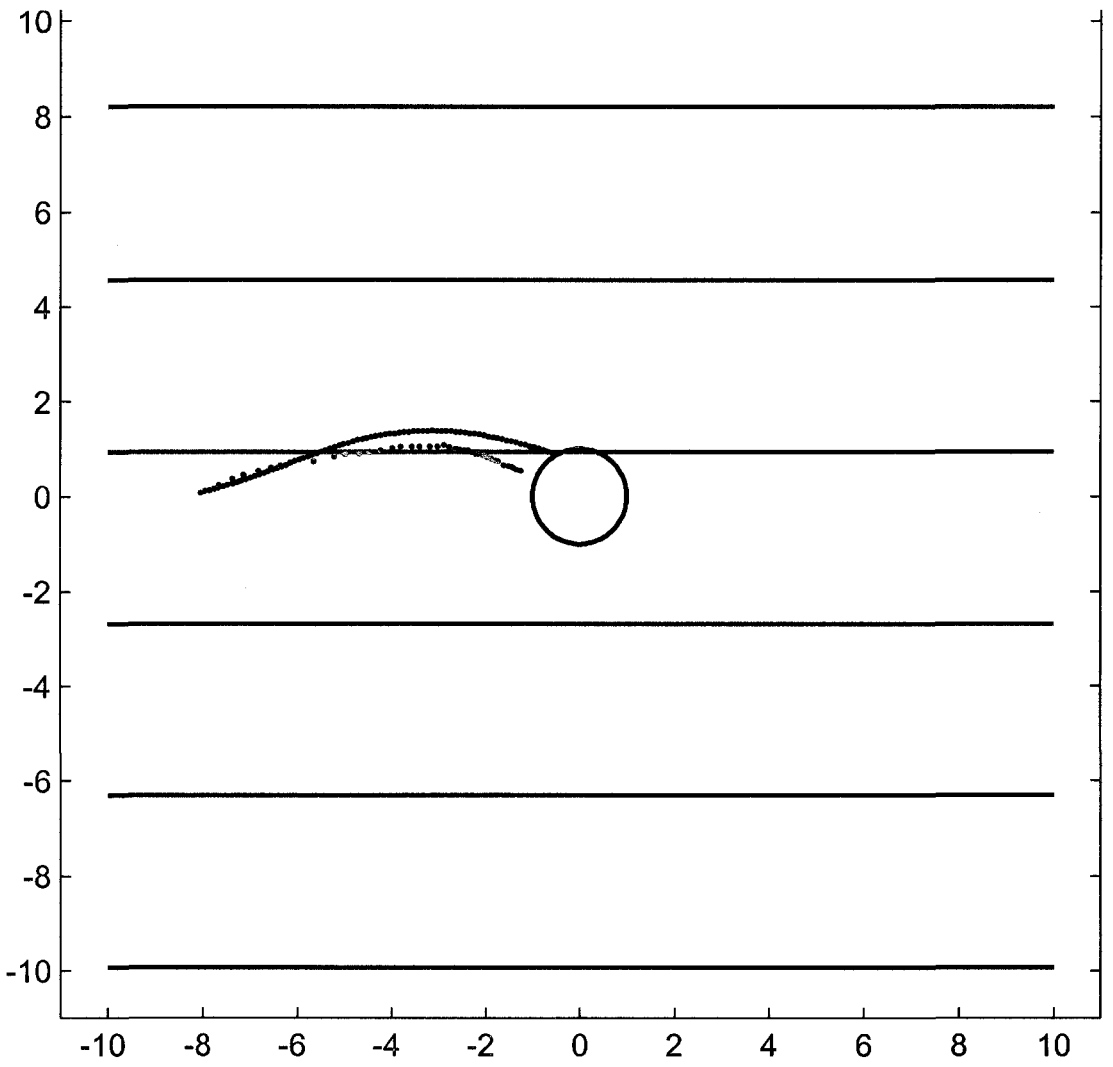

Figure 7.14: This experimental trajectory (E) was taken from the same experiment as C, but passes close to the wire. This is the no-parameter-adjustment fit, with $Gk = 0.81$. The area between the trajectories is 1.69.

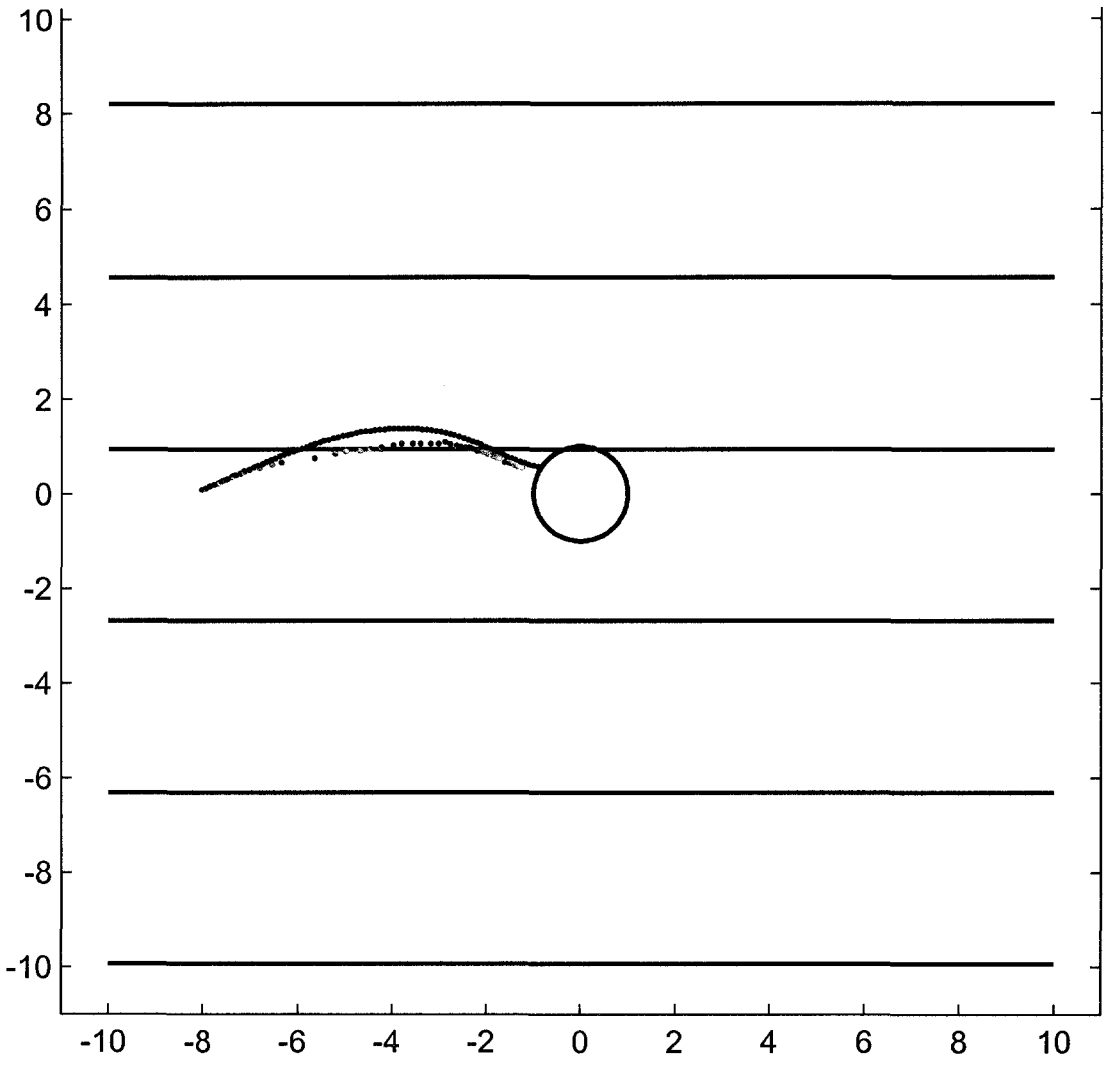

Figure 7.15: Increasing the Gor'kov number to 1.30 for the simulated trajectory decreases the area between it and experimental trajectory E to 1.42.

7.2.3.4 The Effect of Particle Size

The size distribution of the polystyrene particles used was not narrow; diameters ranged from 37 to 92 μm. A total of 80% of the particles had a diameter between 47 and 72 μm. Size plays a significant role in determining the force felt by a particle in an acoustic field, as evidenced by the definition of the Gor'kov number.

$$Gk = \frac{R_p^2 k E_{ac}}{\mu U_f} \tag{7.4}$$

With the nominal particle radius used in the initial model calculations, the value of *Gk* was 0.81. However, at the extreme ends of the 80% particle size range mentioned above, the Gor'kov number could be as low as 0.61 and as high as 1.44. This could explain some of the variability in the trajectory fitting in Section 7.2.3.4, but not the difference of model performance seen between particles that flow near the wire and ones that flow farther away from it.

7.3 Cross-Correlation Plots

Cross-correlation, described in Section 6.4.2, was used to view the experimental particle flow field as a series of vectors, like the simulated vector flow fields depicted in Section 5.1. Figure 7.16 shows the result of cross-correlation (red) of 30 frames of experimental video overlapping the model prediction (green). The model vectors appear to match the experimental ones generally, but there are differences. For example, the model vectors show more deviation from the horizontal than the experimental ones, i.e., many of the cross-correlated vectors are straight in

the flow direction, while the model predicts slightly more vertical movement. The model results presented here were calculated using both incident and reflected waves.

The more vertical movement that the model predicts may be the same phenomena experienced with the trajectory plots—that farther away from the wire, the model computes too large of an effect for the acoustic forces. Visually, most of the plot is "far" from the wire if "far" is considered more than 2 radii. To see this, the experimental cross-correlation results from Figure 7.16 were plotted with the model of flow around the wire in the absence of an acoustic field (Figure 7.17). Here the model predicts vectors with a gentler slope, matching the experimental vectors more effectively.

From experiment to experiment, the cross-correlation results did not differ significantly. Figure 7.18 is a plot of another set of vector data compared to the model; it is nearly identical to Figure 7.16.

A significant characteristic of the cross-correlation results of experimental particle flow in the presence of the acoustic field is the difference between vectors above and below the fiber in Figure 7.16 and Figure 7.18. Above the fiber, the particle flow follows an arc-like trajectory, while below the flow is almost strictly horizontal. An explanation for this could be related to the location of the transducer; in these plots, it was below the wire while the reflector was above. The acoustic field may have been stronger closer to the transducer. Indeed, examination of digital movies of the experiments shows a tighter line of particles near the pressure node of

the acoustic field. Since the particles were held in a tight line, the measured particle flow was almost solely in the direction perpendicular to the node.

The above explanation also pertains to the particle trajectory comparison in Section 7.2.3. Trajectories C and D were farther from the wire and also farther from the transducer; if the acoustic field did indeed decrease in intensity away from the transducer, this elucidates the need to reduce the Gor'kov number in the model to more closely match these results.

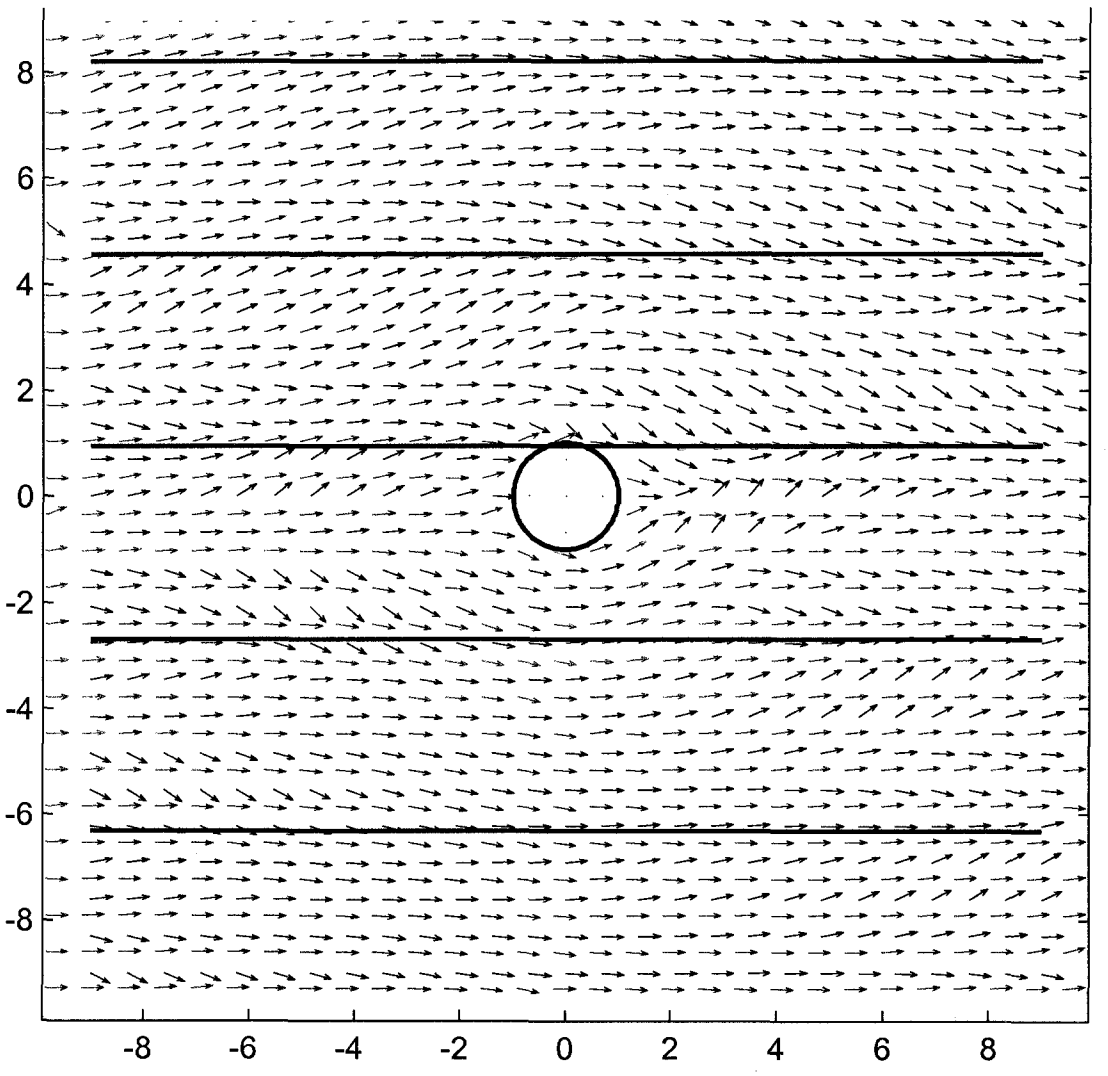

Figure 7.16: Cross-correlation of experimental video produced the red vector field plotted here; the green vector field is the particle velocity vector field predicted by the model using the original parameters from Table 7.1. Each arrow represents the particle velocity at a particular point (the base of the arrow).The vectors are normalized in order to increase visibility.

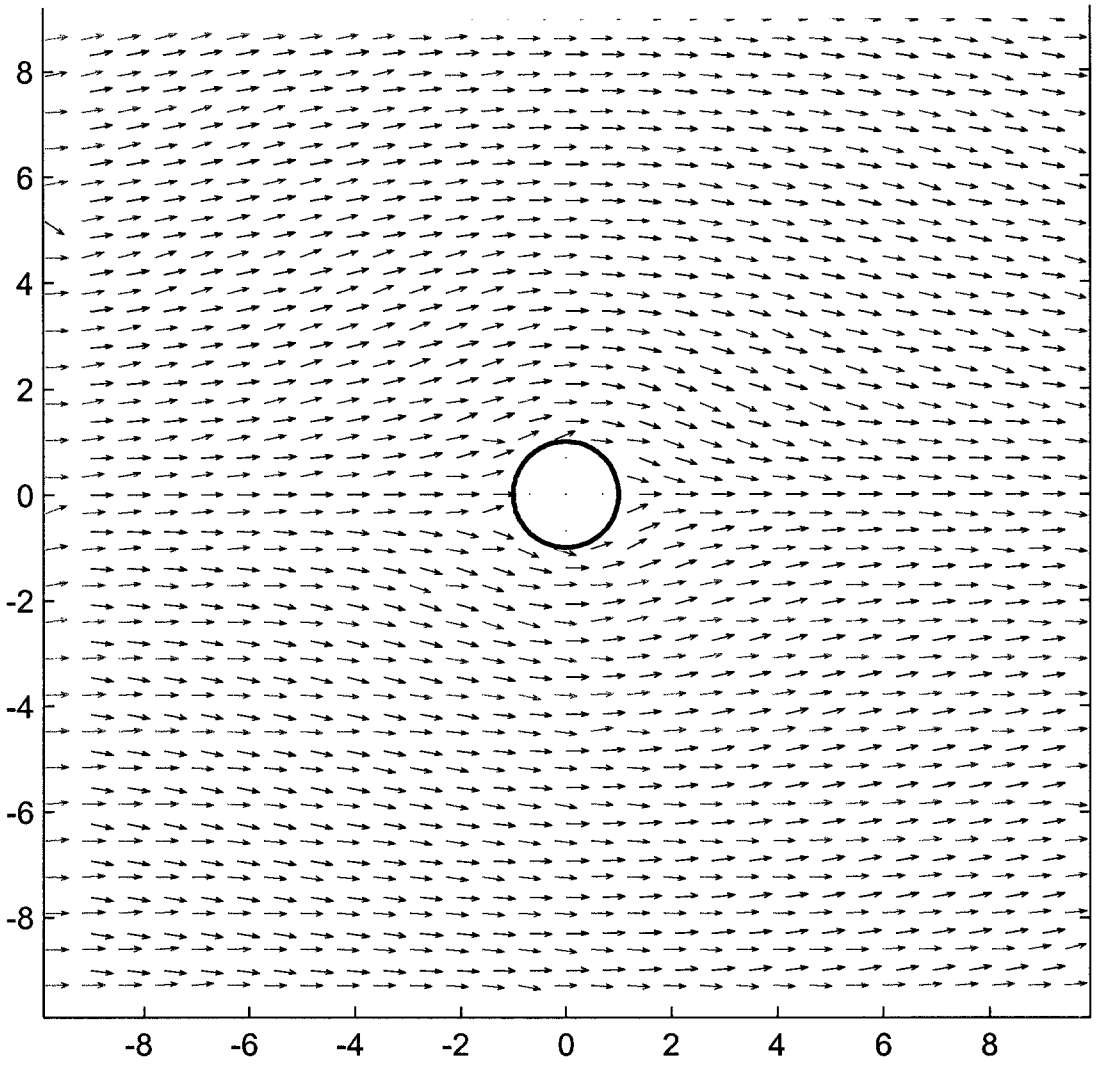

Figure 7.17: Here, the same experimental results shown in Figure 7.16 are plotted along with results calculated with no acoustic field. The model vectors here have a gentler slope than in Figure 7.16 and follow the experimental particle flows more closely.

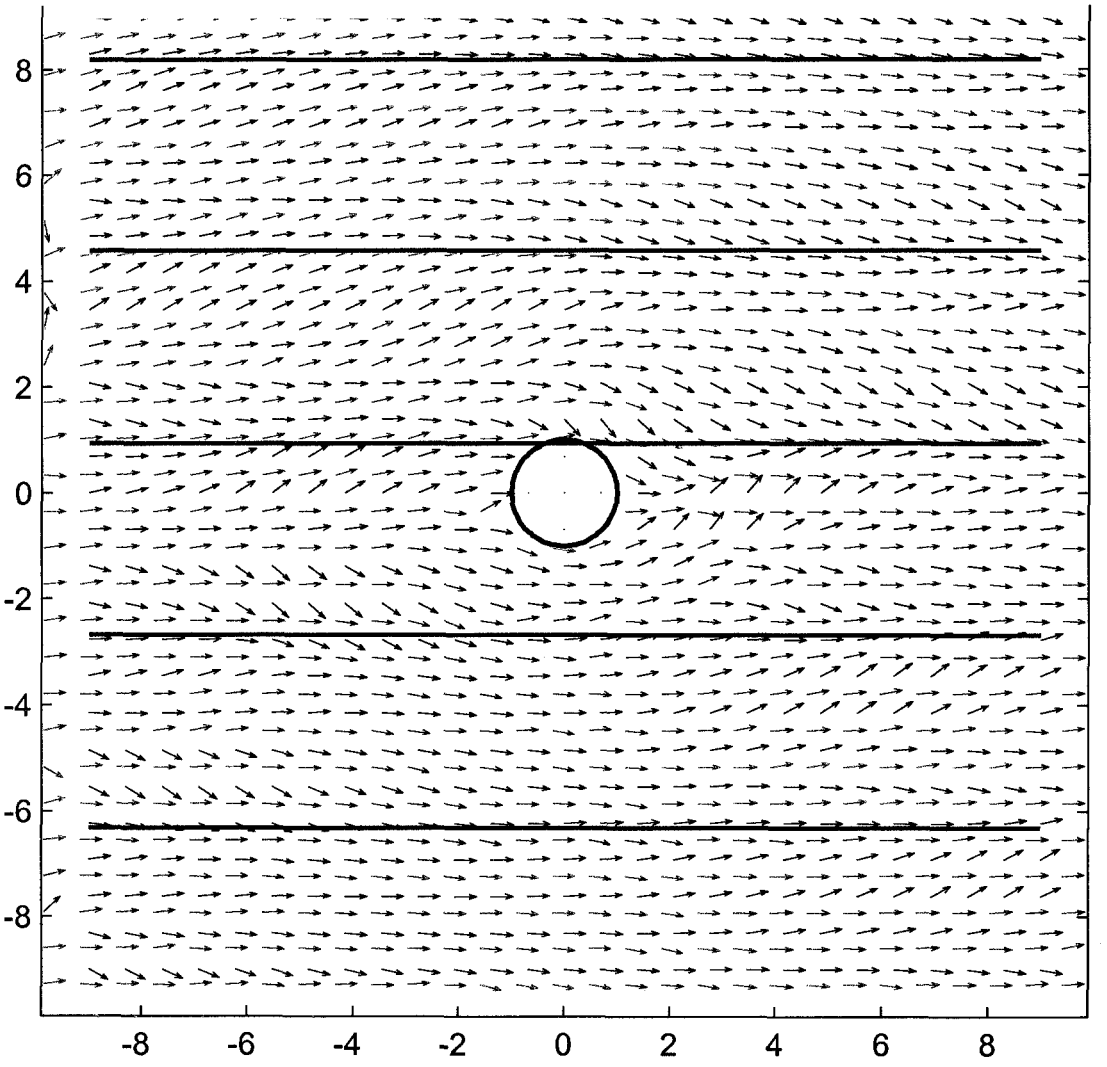

Figure 7.18: Cross-correlation from a different experiment with same conditions as the results in Figure 7.16. The experimental vector field shown here is nearly identical to the one shown in Figure 7.16.

7.4 Discussion of Error

Throughout this chapter and in the previous one, errors in the experiment and model were postulated and discussed. In this section, the main points of those discussions will be summarized.

Arguably the most significant source of error was that the energy density inside the chamber was estimated by a model. This model has been tested experimentally [39] and found to be accurate when it is well established that the experimental system is at maximum reflected power, i.e., the application of acoustic energy is most efficient. But the energy density inside the chamber sharply decreases when the conditions start to deviate from this most efficient point. Because of the short duration of acoustic activation involved in each experimental run, it could not be certain that the resonant frequency initially established remained at the same value. Changes in temperature of one or two degrees could affect the resonant frequency; repeated application of power to the transducer may have raised the temperature slightly.

Comparatively, experimental error in the particle position measurement is quite low. The 1024x1024 pixel size of the captured video frame was calibrated precisely with a 1/64 inch scale to give 182.4 pixels per mm, or 5.482 μm per pixel. Particle position could be measured to within an error of a few pixels; so the error in each spatial measurement was on the order of tens of microns.

Another source of error is comparable to the possibly inaccurate energy density measurement. The particle radius used in the calculations was the nominal

value of a distribution—80 % of the particles had a radius that fell in a range as wide as 10 μm, which gives a ± 20% error in the nominal particle radius of 27 μm.

It has been established in Section 7.2.3.3 that the effect of acoustic forces in the model does not properly scale with distance from the wire. It is possible that particle-particle and particle-wire hydrodynamic interactions not accounted for in the model play a more important role near the wire. Particles are more focused near the wire, and clump together; this may lead to model inaccuracies.

Additionally, buoyancy flows (described in Section 6.3) may have contributed to experimental error. Although no rotational flow was noted until about 8 seconds into each trial, it may have affected the flow profile slightly up to that point.

8 Integrated Model

8.1 Introduction

While the single-fiber model is an excellent tool to understand the underlying phenomena of the acoustic filtration process, it alone is not sufficient to predict the performance of an experimental filter system. A model that combines information from the single-fiber case and properties of the overall system would be able to predict particle breakthrough times and the general retention performance of the acoustic separator.

An approach taken by investigators of High Gradient Magnetic Separation (HGMS) provides the starting point for this analysis [40]. In HGMS, a steel mesh (similar to steel wool) is magnetized to collect small magnetically-susceptible particles from a suspension. This process has been examined microscopically [40] in a similar manner as the acoustic separation process in this research (Chapter 4). Once a capture radius has been defined (akin to the "capture window" discussed in Section 5.2), a multi-wire model is assembled to form a model of the entire separator [41].

In this chapter, the derivation of this model as it applies to the acoustic separation process is presented along with the numerical method of solution of the resulting differential equations. Finally, some example calculations of experimental systems are examined here.

8.2 Derivation of the Separator Equations

8.2.1 Coordinate System and Important Parameters

The phenomenological model will describe the loading behavior and time-dependent performance of an acoustic separation chamber. A schematic of the process is presented in Figure 8.1, with the coordinate system that will be used in the derivation.

The chamber has length L and a cross-sectional area of unity; x is the independent variable along this length. The linear approach velocity of the fluid is v_o; with the porosity of the mesh defined as ε_o, this velocity becomes v_o / ε_o inside the mesh. Two variables describe the concentration of particles in the system. First, $C(x,t)$ is used to denote the concentration of particles in suspension (not trapped in the separation medium), with units of particles per volume of fluid. The variable $N(x,t)$ denotes the particle retention density, or number of trapped particles per unit volume of the separator, where N_T is used to indicate the maximum of N inside a particular system (and $y = N/N_T$). With the concentration of the entering suspension defined as $C(0,t) = Co$, the derived model will predict how C and N change with position and time.

8.2.2 Conservation Equation

A material balance around one section of the volume can be calculated in order to obtain a differential equation relating C and N to position and time. Imagine a volume of thickness (and, since the cross-sectional area is defined as one, also

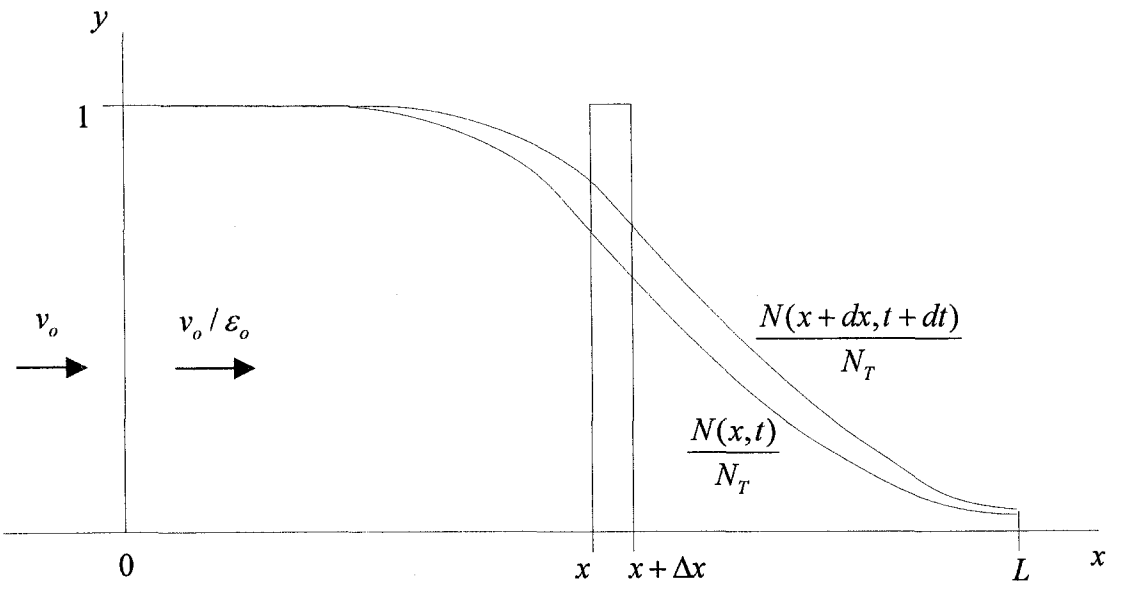

Figure 8.1: A schematic depicting the coordinate system for the overall model. The suspension flows in from the left at $x = 0$ and exits the chamber at $x = L$; $y = N/N_T$ is the normalized buildup of particles with $y = 1$ indicating a full mesh. The time variable is t.

volume) Δx at a distance x from the chamber entrance. Here, since the particles are relatively large, diffusion is neglected and the total number of particles inside the differential volume is a combination of particles in suspension and trapped in the mesh, $N + \varepsilon_o C$. If the porosity is assumed to remain constant, the material balance may be written as particle accumulation = particles in – particles out,

$$\frac{\partial}{\partial t}(N+\varepsilon_o C)\Delta x \quad = \quad (v_o/\varepsilon_o)\varepsilon_o C \quad - \quad (v_o/\varepsilon_o)\left[\varepsilon_o C + \frac{\partial}{\partial x}(\varepsilon_o C)\Delta x\right], \qquad (8.1)$$

which can be simplified to

$$\frac{\partial}{\partial t}(N+\varepsilon_o C)\Delta x \quad + \quad v_o \frac{\partial C}{\partial x} \quad = \quad 0. \qquad (8.2)$$

With the definition of displacement time,

$$\tau \quad = \quad t - \varepsilon_o x / v_o, \qquad (8.3)$$

Eq. (8.2) can be simplified by changing the variables to give the conservation equation.

$$\frac{\partial N}{\partial \tau} + v_o \frac{\partial C}{\partial x} = 0 \tag{8.4}$$

8.2.3 Rate Equation

8.2.3.1 Capture Probability

More information is needed to solve Eq. (8.4); the accumulation rate can be determined from a model based on the individual fiber capture window. First, it is noted that the increase in number of captured particles in the separator between x and $x + \Delta x$ during $\Delta \tau$ is

$$\left(\frac{\partial N}{\partial \tau}\right) \Delta x \Delta \tau . \tag{8.5}$$

The number of particles entering this volume is

$$\left(v_o / \varepsilon_o\right) \varepsilon_o C \Delta \tau . \tag{8.6}$$

The probability that a particle will be captured in the differential volume is Eq. (8.5) divided by Eq. (8.6).

$$p = \left(\frac{\partial N}{\partial \tau}\right) \frac{\Delta x}{v_o C} \tag{8.7}$$

8.2.3.2 Filter Performance

But this probability of capture is also given by the mechanism of capture and may be written as

$$p = 1 - \frac{N_{out}}{N_{in}} \tag{8.8}$$

Assume that each filter element (fiber) has a cross-sectional capture area per unit length of $A << 1$ and that each element acts individually. The probability of capture by the first element is A divided by the total area, which is 1. The probability of each element in succession can be computed.

$$\begin{aligned} &1^{st}\ element \quad p_1 = A \\ &2^{nd}\ element \quad p_2 = A(1-A) \\ &3^{rd}\ element \quad p_3 = A\left[1-A-A(1-A)\right] = A(1-A)^2 \\ &\vdots \\ &k^{th}\ element \quad p_k = A(1-A)^{k-1} \end{aligned} \tag{8.9}$$

This probability may be summed over total number of filter elements, n, to determine the total probability that a particle will be captured by the matrix, p_T.

$$p_T = \sum_{k=1}^{n} p_k = A\sum_{k=1}^{n}(1-A)^{k-1} = 1-(1-A)^n \tag{8.10}$$

Combining Eq. (8.8) and Eq. (8.10), and using

$$(1-A)^n \approx \exp(-nA) \tag{8.11}$$

for large n, the filter performance can be written as

$$p_T = 1 - \exp(-nA)\,. \tag{8.12}$$

If the fibers are assumed to be perpendicular to the flow and are arranged such that each has unit length (this approximation is valid if the fibers are contained the cross-sectional plane, reaching from one side dimension to the other), the capture cross-section is

$$A = 2R_{ca}R_c, \tag{8.13}$$

where R_{ca} is the dimensionless capture radius ($2R_{ca}$ is the width of the capture window as defined in Section 5.2) and R_c is the fiber radius. Also, the number of fibers in the mesh may be computed as

$$n = \frac{total\ volume\ of\ solids\ comprising\ the\ mesh}{volume\ of\ single\ fiber} = \frac{(1-\varepsilon_o)L}{\pi R_c^{\,2}}. \tag{8.14}$$

Since all the wires may not be oriented properly, a "randomness" parameter, <*f*>, is introduced and combined with the 2 in Eq. (8.13); for an ordered filter, <*f*>=2, and for a random acoustic filter <*f*> is 2/3. This is based on the simplified assumption that 1/3 of the fibers are oriented properly. With the preceding definition and equations, Eq. (8.12) can be rewritten.

$$p_T = 1-\exp\left(-\frac{<f>(1-\varepsilon_o)R_{ca}L}{\pi R_c}\right) \tag{8.15}$$

The above expression is for the entire volume of the separator; for the differential volume discussed in Section 8.2.3.1, Eq. (8.15) is

$$p_T = 1-\exp\left(-\frac{<f>(1-\varepsilon_o)R_{ca}\Delta x}{\pi R_c}\right) \approx \frac{<f>(1-\varepsilon_o)R_{ca}\Delta x}{\pi R_c}. \tag{8.16}$$

If Eq. (8.16) is combined with (8.7), the following definition of the derivative is obtained.

$$\frac{\partial N}{\partial \tau} = \frac{<f>(1-\varepsilon_o)R_{ca}L}{\pi R_c} v_o C \tag{8.17}$$

Here, deterioration of the capture radius with particle accumulation is simulated by a function *G*.

$$R_{ca} = R_{cao} G\left(N / N_T\right) \tag{8.18}$$

The capture radius of a bare fiber is R_{cao} and G is defined such that $G(0) = 1$ and $G(1) = 0$. A commonly used form for G [40] is

$$G\left(N / N_T\right) = G\left(y\right) = \left(1 - y\right)^{\gamma}. \tag{8.19}$$

The exponent γ depends on the general operating conditions, but is typically between 0.1 and 2.

With the definition

$$L_o = \frac{\pi R_c}{< f > \left(1 - \varepsilon_o\right) R_{cao} L}, \tag{8.20}$$

the rate equation (Eq. (8.17)) is

$$\frac{\partial N}{\partial \tau} = \frac{v_o}{L_o} GC. \tag{8.21}$$

8.3 Solution Method

Although the rate equation can be combined with the conservation equation to eliminate C, giving

$$\frac{\partial N}{\partial \tau} + L_o \frac{\partial}{\partial x}\left[\frac{1}{G}\frac{\partial N}{\partial \tau}\right] = 0, \tag{8.22}$$

the numerical solution is more straightforward if Eq. (8.4) and Eq. (8.21) are integrated separately.

$$\frac{\partial N(x,\tau)}{\partial \tau} + v_o \frac{\partial C(x,\tau)}{\partial x} = 0 \tag{8.4}$$

$$\frac{\partial N(x,\tau)}{\partial \tau} = \frac{v_o}{L_o} G(N) C(x,\tau) \tag{8.21}$$

The boundary condition along $x = 0$ is

$$C(x=0,\tau) = C_o, \tag{8.23}$$

where Co is the particle concentration in the feed. Along the x-axis ($\tau = 0$),

$$N(x,\tau=0) = 0, \tag{8.24}$$

i.e., there is no particle buildup at the start of the process.

The above set of differential equations was solved using a method suggested by Gerber [41]. First, Eq. (8.21) is solved for x=0 using the Runge Kutta method to give $N(0,\tau)$. The derivative $\frac{\partial N}{\partial \tau}(\tau)$ is evaluated and substituted into Eq. (8.4) to obtain $\frac{\partial C}{\partial x}(\tau)$. The suspension concentration for the next step in x is given by

$$C(0+\Delta x,\tau) = C(0,\tau) + \frac{\partial C}{\partial x}(\tau)\Delta x. \tag{8.25}$$

The process is repeated through the solution grid one slice at a time until the end of the separator is reached at $x = L$.

The above solution method is valid for the case of no suspension in the chamber at start-up, i.e., the suspension is fed into the separator at $t = 0$. Many experiments have been run where suspension is continuously flowing into the chamber and the acoustic field is turned on at $t = 0$. For this case, the boundary condition Eq. (8.23) remains valid, but there is another condition on C,

$$C(x,t=0) = C_o, \tag{8.26}$$

and Eq. (8.24) must be adjusted to

$$N(x,t=0)=0\,. \tag{8.27}$$

Using the definition of τ, Eq. (8.3), the boundary conditions are:

$$C(x=0,\tau)=C_o \tag{8.28}$$

$$C(x,\tau=-\varepsilon_o x/v_o)=C_o \tag{8.29}$$

$$N(x,\tau=-\varepsilon_o x/v_o)=0 \tag{8.30}$$

This problem is solved in the same manner as the previous set of boundary conditions, but the solution grid must be spaced properly, with

$$\Delta\tau=\varepsilon_o\Delta x/v_o\,. \tag{8.31}$$

Additionally, when C is computed with Eq. (8.25), the boundary condition specified in Eq. (8.29) is used for the first τ grid point, $\tau=-\varepsilon_o x/v_o$.

8.4 Results

8.4.1 Set 1: Gupta and Feke [2]

The model was used to simulate results by Gupta and Feke, published in a recent paper [2]. The conditions for an initial experiment are given in Table 8.1. First, the single-fiber model discussed in Chapters 4 and 5 was used to obtain the capture window for the particular environment (averaged over nodal position of the incident acoustic wave). The energy density input for this calculation was found using the same computer model as the experimental analysis in Chapter 7 [39].

After the capture window was determined, the overall model was solved to obtain concentration, $C(x,t)$, and particle buildup, $N(x,t)$, profiles. These were normalized using C_o and N_T, respectively. The maximum concentration of trapped particles in the chamber was estimated to be 15 volume % by Gupta [42].

Table 8.1: Parameters of an experiment by Gupta [2].

Feed suspension	0.5 wt% 325-mesh polystyrene
Flow rate	30 mL/min
Chamber dimensions	5.82 mm x 35 mm x 70 mm
Mesh composition	Polyester, 10 pores per inch
Power supplied to transducer	20 W
Frequency	1.103 GHz

A typical model result for N/N_T, normalized particle buildup in the separator, is shown in Figure 8.2 as a 3-d plot with the independent variables x and t. Note that there is some initial buildup due to the initial concentration of particles in suspension throughout the chamber. But the predominant feature is the progression of particle buildup travelling in the x direction, which is similar to Figure 8.1, if examined in a cross-section of constant time.

In Figure 8.3, the simulated output concentration for the conditions listed in Table 8.1 is presented as a function of time along with experimental data obtained by Gupta [2]. Figure 8.4 and Figure 8.5 show model and experimental results for a flow rate increased to 60 mL/min and a feed concentration increased to 1.0 wt%,

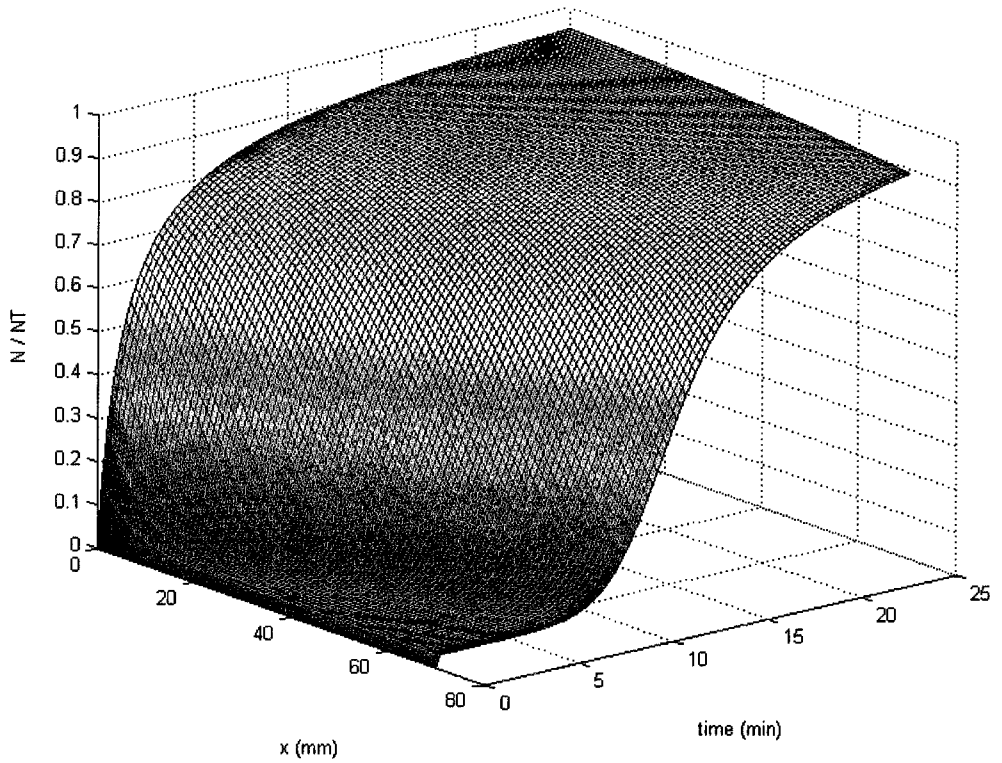

Figure 8.2: A three-dimensional plot of the normalized buildup of particles inside the chamber as predicted by the integrated model. When N/N_T reaches a value of 1, that portion of the chamber is full. The length of this chamber is 70 mm.

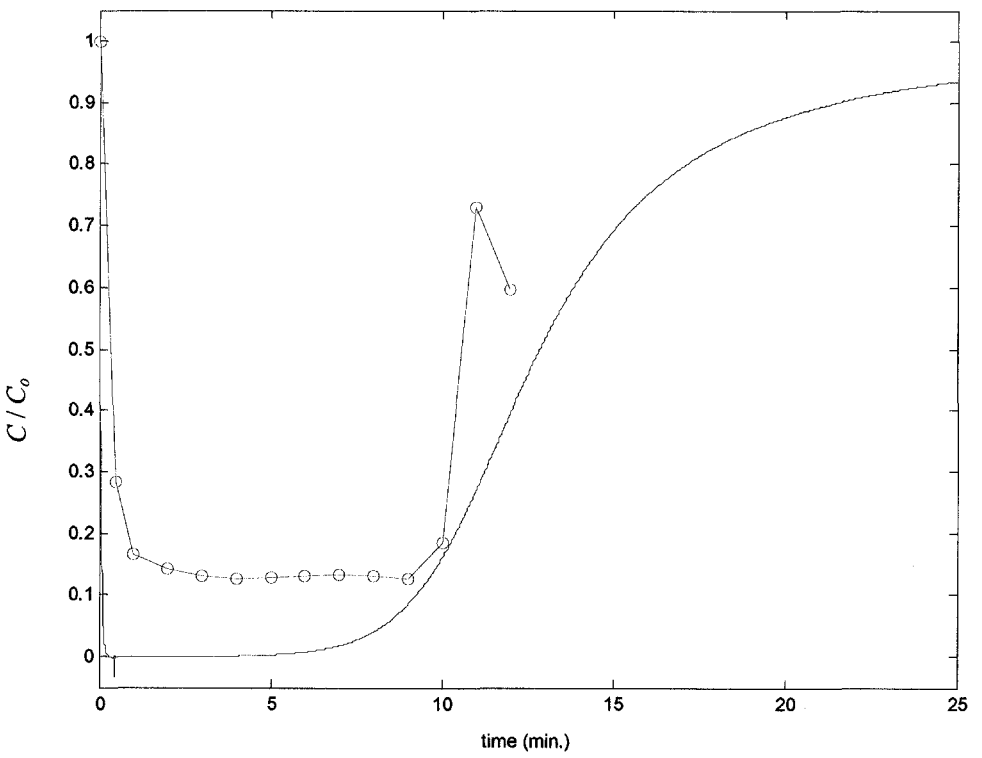

Figure 8.3: The normalized concentration at the separator exit for a flow rate of 30 mL/min and an inlet concentration of 0.5 wt%. Other conditions of the experiment are listed in Table 8.1. The red circles are experimental data [2] and the green line is the output of the integrated model. Without any parameter adjustments, breakthrough time is predicted quite well, but the actual concentration does not drop as significantly as the simulation calculates.

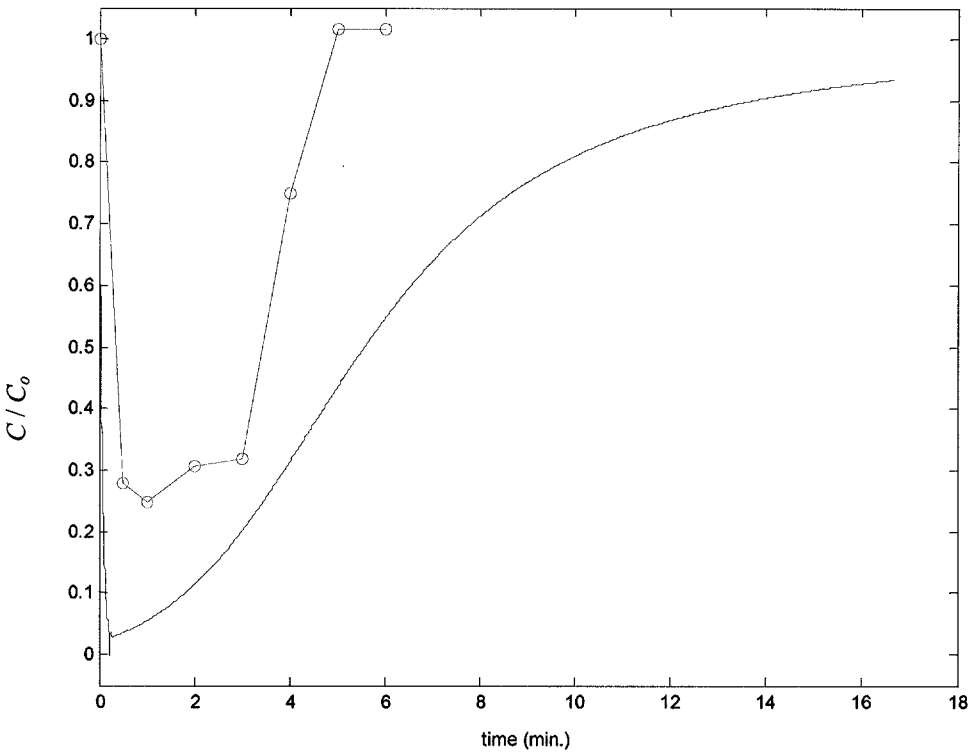

Figure 8.4: The normalized concentration at the separator exit for a flow rate of 60 mL/min and an inlet concentration of 0.5 wt%. Other conditions of the experiment are listed in Table 8.1. In this case, the experimental output concentrations (red) are again slightly higher than expected from model predictions (green).

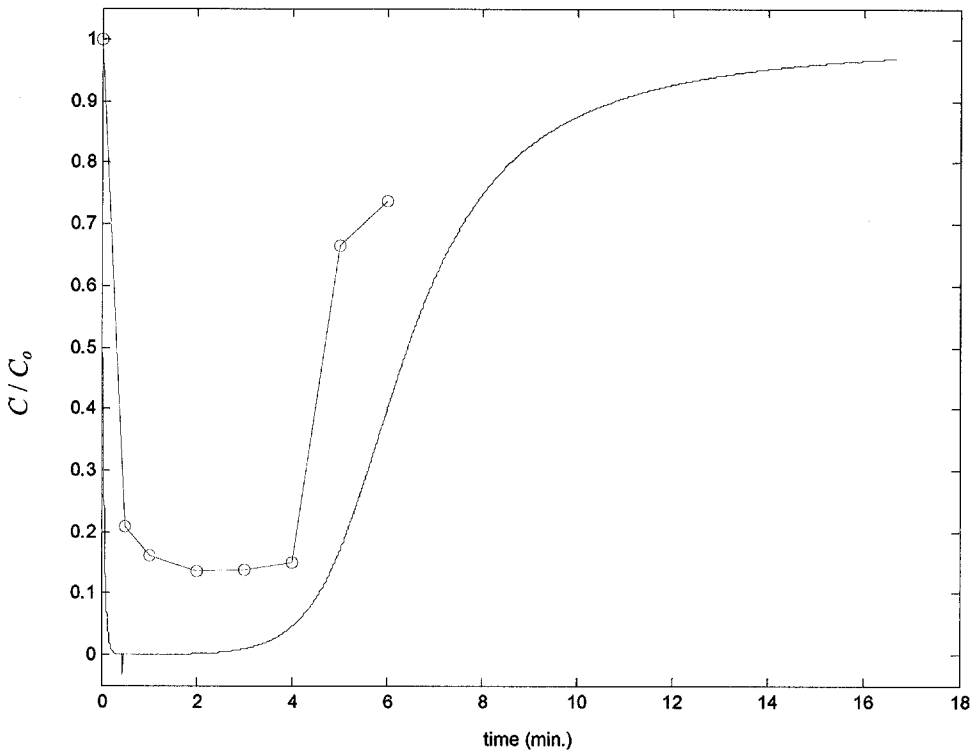

Figure 8.5: The normalized concentration at the separator exit for a flow rate of 30 mL/min and an inlet concentration of 1.0 wt%. Other conditions of the experiment are listed in Table 8.1. Again, the model predicts a lower concentration (green) than the experiment (red), but the breakthrough time is appropriately scaled from Figure 8.3.

respectively. For this model, the coefficient of the deterioration function, γ, was chosen to be 2, and 2/3 was used for the value of $<f>$. In Figure 8.3, the simulated normalized concentration, C/C_o, begins at 1 and sharply declines toward zero for the first 20 seconds. A discontinuity in the output is present at 0.5 minutes, which is the residence time of the suspension in the chamber. After 5 to 6 minutes with no particles exiting the separator, a gradual rise in the concentration appears before a sharp linear slope beginning near 10 minutes. The normalized concentration asymptotically approaches 1 as the time continues past 20 minutes.

One major difference between experimental and model results is that, after a short initial drop in concentration from C_o, the model shows 100% efficiency until breakthrough begins to occur. At best, Gupta's results show 85% efficiency; for the most part the maximum is 80%. However, the same trend is present, a sharp decline in exit concentration, followed by a plateau. After a period of time at the plateau concentration, the value begins to rise. In his experiments, Gupta noted the exit concentration over time for each set of conditions; a breakthrough point can be singled out when the plateau concentration begins to rise. Unfortunately no data was recorded after this ascent was noted.

The time to breakthrough is used as a comparison between model and experiment. Particularly, changes in experimental conditions give changes in breakthrough times, so if the simulation predicts the same changes, this is an indication of the applicability of the model. Table 8.2 lists breakthrough times from experiments and model calculations for different flow rates and feed concentrations.

Table 8.2: Breakthrough time comparison.

Flow Rate	Feed Concentration	Breakthrough Time	
		Experiment	*Model*
30 mL/min	0.5 wt%	10 min	9 min
60 mL/min	0.5 wt%	3 min	1.5 min
30 mL/min	1.0 wt%	4 min	4.5 min

The breakthrough times compare well between model and experiment; it is important to note that no model parameters were adjusted to fit the data in this case. As one might expect, doubling the feed concentration halves the time to breakthrough in both the experiment (approximately) and in the model. Since twice as many particles pass through the chamber in the same amount of time, the capacity of the filter is reached in half the time.

The effect of doubling the flow rate, however, is not as straightforward. One might expect again that the time to fill the capacity of the separator would be halved. According to both the experiment and the model, however, this is not the case. In Gupta's work, the "filtration time", or time to breakthrough, is reduced to 30% of the original value; in the model it is reduced to nearly 20% of the breakthrough time of the lower flow rate. This can be explained by examining what is happening microscopically. The single-fiber capture window was calculated to be 2.8 for a 30 mL/min flow rate, but was reduced to 0.98 when the flow was doubled to 60 mL/min. So, not only is the separator exposed to more particles per unit time, the effectiveness

of the filter is reduced by the increase in linear flow speed. Both of these factors affect the breakthrough time, and the model predicts this behavior quite appropriately.

8.4.2 Set 2: Grabenstetter [43]

The overall model was used to simulate another separation experiment that used a different chamber and support equipment than the work described in Section 8.4.1. The conditions of this experiment are given in Table 8.3. The energy density in the fluid was estimated using the previously mentioned model by Rusinko [43,39].

Table 8.3: Parameters of an experiment by Grabenstetter [43].

Feed suspension	0.21 wt% 74μm-diameter polystyrene
Flow rate	35 mL/min
Chamber dimensions	25.5 mm x 22.3 mm x 42.2 mm
Mesh composition	Polyester, 10 pores per inch
Energy density	0.02 J/m^3
Frequency	1.100 GHz

Integrated model results obtained using the solution procedure outlined in the preceding sections are shown in Figure 8.6 along with concentration data from the experiment. The model does predict efficiency less than 100%, i.e., the normalized exit concentration, C / C_o, only drops to 0.32 instead of zero, but in the experiment this value drops to 0.15. Also, the model shows a nearly linear increase in concentration with very shallow slope after the initial drop, while the actual

concentration plateaus at 0.15 before it rises with a much steeper slope as time progresses.

Since the maximum concentration of trapped particles in the ultrasonic separation chamber, N_T, was estimated by Gupta [42] for his particular system, the value of 15 volume % may not be appropriate here. Figure 8.7 shows model results with a maximum concentration of 5 volume %. In this case, the simulated C / C_o drops to the same value as in Figure 8.6, but the concentration increase is more similar to that of the experiment.

It is expected that N_T depends on operating conditions, particularly the strength of the applied acoustic field. Because it has a significant impact on the results of the integrated model, the maximum concentration of trapped particles in a given experimental system should be more thoroughly studied. If it is known how operating conditions affect this parameter, a more accurate value of N_T could be predicted for cases where no experiment data exist, such as with scale-up simulations.

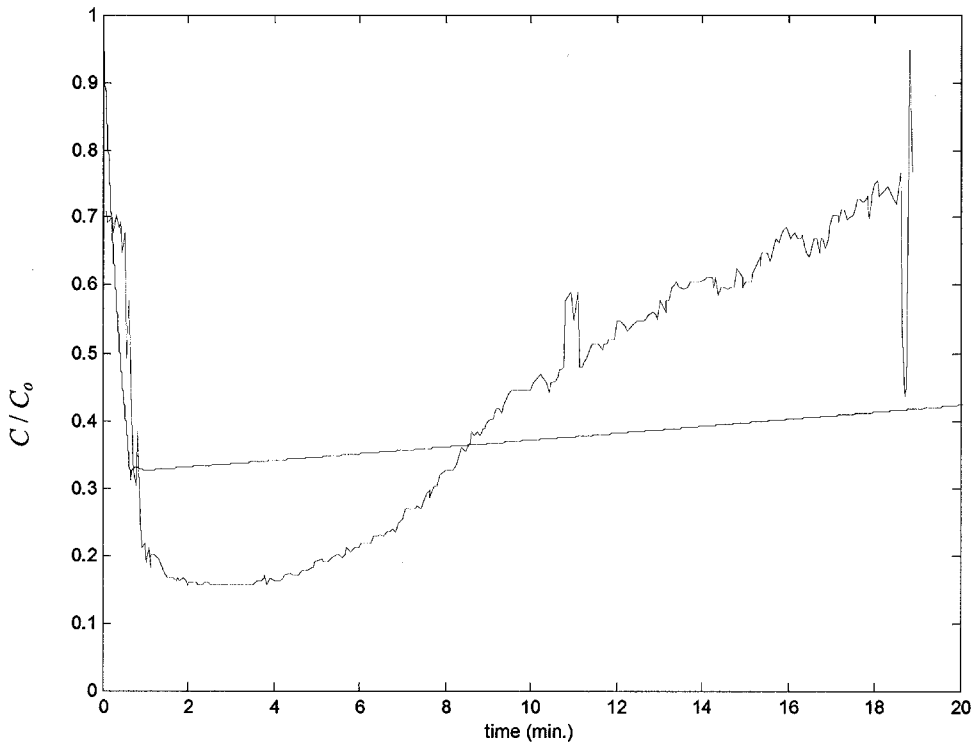

Figure 8.6: The normalized concentration at the exit of the separator is shown for both the integrated model (green) and the experiment (red) with conditions shown in Table 8.3 [43].

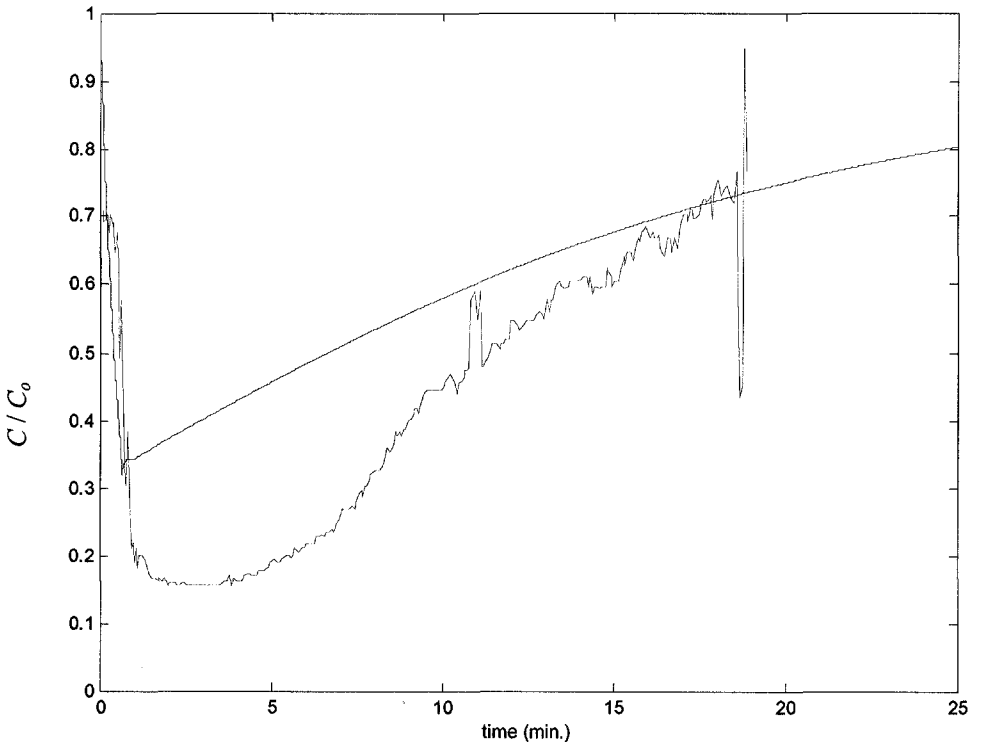

Figure 8.7: Decreasing the maximum concentration of trapped particles inside the acoustic chamber from 15 volume % to 5 volume % gives a model prediction (green) that predicts a rise in concentration more similar to the experiment (red) than Figure 8.6.

9 Summary and Conclusions

9.1 Summary

The main objective of this work was to gain a fundamental understanding of the underlying phenomena involved in the acoustically enhanced separations process. This entailed a modeling and an experimental study of the interaction of individual particles with single cylindrical collectors. A secondary goal was to develop a method that could predict performance based on this understanding of the particle-scale phenomena. Through the derivation of the single-fiber model and subsequent single-fiber experiments, the first goal of this research was met. The information from this study was used to move toward the second objective with the integrated model presented in Chapter 8.

Particle capture mechanisms were postulated, including a scenario where particles collide with and stick to elements of the mesh. The single-fiber model, which included drag and acoustic forces on a particle, predicted particle trajectories that impacted the fiber, a single element of the porous mesh present inside the acoustic separation chamber. Experimental observations were duplicated by the model, such as the focusing of particles to particular locations on the circumference of the fiber. Also shown by the model was evidence that a particle may become trapped in the fluid near a fiber solely by a balance between acoustic and drag forces.

Verification of the single-fiber model was accomplished by designing an experimental system to visualize the interaction between particles and a cylinder (fiber) that was subjected to a resonating ultrasonic field. A wire was suspended

inside an acrylic chamber such that a digital video camera could have a visual axis parallel to its length, i.e. the cross-section of the wire appeared as a circle in the image plane. Particle tracking techniques were used to analyze the images and record the position of particles as the fluid flowed around the wire in the presence of an acoustic field. These trajectories were compared with those determined by the single-fiber simulation.

Particle capture by the wire was observed in the experiment and the experimental trajectories roughly matched simulations without any model parameter adjustment. All of the parameters of the model were taken from actual measurements of the experimental system except the energy density of the acoustic field, which was estimated based on chamber dimensions and properties and applied power using a model by Rusinko [39]. The fit between single-fiber model and experimental trajectories was further improved via adjustments in the Gor'kov number, the relative intensity of acoustic forces to flow forces. It was found that near the wire (fiber), acoustic forces predicted by the single-fiber model were slightly higher in the experiment. At distances a few radii away from the fiber, the model overestimated the acoustic forces present significantly.

One of the assumptions of the single-fiber model was that the applied acoustic field is uniform in the chamber. Cross-correlation analysis of experimental particle images indicated that this may not be the case; the intensity of the acoustic field may have been smaller farther from the face of the transducer, i.e., where the model

overestimated the acoustic forces involved. This is consistent with the notion that there will be some attenuation in the sound field.

In order to use the particle trajectory information to predict the performance of an entire separation chamber, the concept of a capture window was defined. This is the area per unit length of a single fiber where particles will become trapped by the fiber; particles that flow through this plane will intersect the fiber and those that do not flow though the plane will flow around the filter element. Based on this idea of a capture window, a model that integrates the single-fiber case to predict the performance of the entire separation system was derived.

This overall model was used to predict the exit concentration versus time for a series of experiments completed by Gupta [2]. The time to breakthrough predicted by the model was near that of the experiment, and also scaled similarly as the experiment with respect to changes in flow rate and feed concentration. However, experimental exit concentrations were underestimated in this case. In a second experimental comparison to results from Grabenstetter [43], it was found that changes in the expected maximum trapped particle concentration allowed the model to fit the data more closely. Model parameter adjustment with additional experimental data may yield a better fit to these experiments.

9.2 Future Work

9.2.1 Single-Fiber Model and Experiment

Based upon the initial model development presented in this document, there are additional efforts that could improve the applicability of the single-fiber simulation and also the understanding of the acoustically aided filtration process. These tasks are outlined below.

- Experimentally examine the particle trajectories around a cylinder that exhibits more elastic properties than the stainless steel wire used here.
- Directly measure the intensity of the acoustic field near the wire inside the experimental chamber using a hydrophone or similar instrument.
- Include an additional fiber, i.e., create a two-fiber model that accounts for acoustic interaction between adjacent filter elements.

9.2.2 Integrated Model

Along the same lines as above, improvements in the overall model parameters will allow more accurate simulation of filtration experiments. With a model that predicts properly, ideas for improvement may be tested in minutes of computer time instead of weeks or months of laboratory time, enabling easy optimization of filtration performance. An accurate model would also be used as a tool to examine scale-up of the ultrasonically aided filtration process. Future efforts to improve the integrated model are outlined below.

- Run a series of controlled experiments to provide enough concentration data in order to accurately fit the parameters γ and $<f>$ of the overall model.
- More thoroughly investigate the maximum particle collection ability of a given filtration system (N_T in the overall model), and formulate a theory to define how this is affected by various operating parameters of the system.
- Incorporate the energy density model by Rusinko [39] along with the single-fiber and integrated model presented here to form a single complete ultrasonic filtration simulation where only physically measured parameters are necessary as input.

9.2.3 Other Ideas

In addition to model improvements mentioned above, other work in this area could lead to innovative devices or larger scale ultrasonic filters. Some ideas are listed below.

- Examine the possibility of a continuous ultrasonically enhanced filtration system, i.e., one that does not require a break in operation time in order to flush or regenerate the porous mesh. For example, a continuously rotating belt of mesh could somehow be incorporated.
- Investigate the acoustic properties of cells thoroughly in order to implement biological separation techniques currently studied [44] in the models described in this document.

Appendix

MATLAB Code for Single-Fiber Model

```
function ffngui(action)

% A MATLAB function to compute the trajectory of a particle
% in a flowing fluid around a cylinder in the presence of an
% acoustic field

% This function plots a grid of direction vectors for particles
% Placed in the flow.

switch action

    case 'run'

        % GET INPUT DATA

        % Fluid Properties

        % free flow velocity                [=] m/s
        Handle = findobj(gcbf,'Tag','FluidVelocity');
        Uf = str2num(get(Handle,'String'));

        % density of fluid                  [=] kg/m^3
        Handle = findobj(gcbf,'Tag','FluidDensity');
        rhof = str2num(get(Handle,'String'));

        % viscosity of fluid                [=] kg/(m s)
        Handle = findobj(gcbf,'Tag','FluidViscosity');
        mu = str2num(get(Handle,'String'));

        % logitudinal sound speed in fluid [=] m/s
        Handle = findobj(gcbf,'Tag','FluidSoundSpeed');
        cf = str2num(get(Handle,'String'));

        % flow angle in pi radians
        Handle = findobj(gcbf,'Tag','FlowAngle');
        flowangle = pi*str2num(get(Handle,'String'));


        % Particle Properties

        % density of particle                   [=] kg/m^3
        Handle = findobj(gcbf,'Tag','ParticleDensity');
        rhop = str2num(get(Handle,'String'));

        % radius of spherical particle          [=] m
        Handle = findobj(gcbf,'Tag','ParticleRadius');
        Rp = str2num(get(Handle,'String'));

        % logitudinal sound speed in particle [=] m/s
        Handle = findobj(gcbf,'Tag','ParticleLongitudinal');
        cp = str2num(get(Handle,'String'));


        % Fiber (Cylinder) Properties
```

```
% density of cylinder                [=] kg/m^3
Handle = findobj(gcbf,'Tag','FiberDensity');
rhoc = str2num(get(Handle,'String'));

% radius of cylinder                  [=] m
Handle = findobj(gcbf,'Tag','FiberRadius');
Rc = str2num(get(Handle,'String'));

% logitudinal sound speed in cylinder [=] m/s
Handle = findobj(gcbf,'Tag','FiberLongitudinal');
c1 = str2num(get(Handle,'String'));

% shear sound speed in cylinder       [=] m/s
Handle = findobj(gcbf,'Tag','FiberTransverse');
c2 = str2num(get(Handle,'String'));


% Acoustic Field Properties

% frequency of sound waves          [=] Hz
Handle = findobj(gcbf,'Tag','Frequency');
freq = str2num(get(Handle,'String'));

w = 2*pi*freq;  % angular frequency                [=] rad/s
k = w/cf;       % wavenumber in fluid              [=] 1/m

% energy density of acoustic field [=] J/m^3
Handle = findobj(gcbf,'Tag','EnergyDensity');
Eac = str2num(get(Handle,'String'));
%Eac = Gkn*mu*Uf/k/Rp^2;

% distance between nodal plane (velocity potential)
%                        and cylinder axis          [=] m
Handle = findobj(gcbf,'Tag','NodeOffset');
hinput = str2num(get(Handle,'String'));
h = -hinput*cf/freq;

% Calculate Incident Wave? (1=yes 0=no)
Handle = findobj(gcbf,'Tag','IncidentWave');
incident = get(Handle,'Value');

% Calculate Reflected Wave? (1=yes 0=no)
Handle = findobj(gcbf,'Tag','ReflectedWave');
reflected = get(Handle,'Value');


% Gravity Options

% Calculate Gravity? (1=yes 0=no)
Handle = findobj(gcbf,'Tag','Gravity');
gravity = get(Handle,'Value');

% gravity angle in pi radians
Handle = findobj(gcbf,'Tag','GravAngle');
gravangle = pi*str2num(get(Handle,'String'));


% Plot Options

% Range
Handle = findobj(gcbf,'Tag','Range');
gridsize = str2num(get(Handle,'String'));

% Number of Points
Handle = findobj(gcbf,'Tag','GridPoints');
points = str2num(get(Handle,'String'));
```

```
% Completion Time
Handle = findobj(gcbf,'Tag','Completion');
set(Handle,'String','Estimated Completion Time');


terms=100;

Gk=Rp^2*k*Eac/(mu*Uf);
Re=2*rhof*Uf*Rc/mu;




% Get the functions an and bn (where dn=an+i*bn) A=[an bn]

clear x1 x2 x3 n dn ddn J1 dJ1 ddJ1 J2 dJ2 ddJ2 J3 dJ3 H dH An Bn Cn Dn Fn dn
a b;

x1=w*Rc/c1;
x2=w*Rc/c2;
x3=k*Rc;

% compute the required bessel functions for an and bn

n   = [0:terms+2];
dn  = [0:terms+1];
ddn = [0:terms  ];

J1   = besselj(n,x1);
dJ1  = dn/x1.*J1(1:terms+2) - J1(2:terms+3);
ddJ1 = -ddn/x1^2.*J1(1:terms+1) + ddn/x1.*dJ1(1:terms+1) - dJ1(2:terms+2);
J1   = J1(1:terms+1);
dJ1  = dJ1(1:terms+1);

J2   = besselj(n,x2);
dJ2  = dn/x2.*J2(1:terms+2) - J2(2:terms+3);
ddJ2 = -ddn/x2^2.*J2(1:terms+1) + ddn/x2.*dJ2(1:terms+1) - dJ2(2:terms+2);
J2   = J2(1:terms+1);
dJ2  = dJ2(1:terms+1);

J3   = besselj(n,x3);
dJ3  = dn/x3.*J3(1:terms+2) - J3(2:terms+3);
J3   = J3(1:terms+1);
dJ3  = dJ3(1:terms+1);

H    = besselh(n,x3);
dH   = dn/x3.*H(1:terms+2) - H(2:terms+3);
H    = H(1:terms+1);
dH   = dH(1:terms+1);

% calculate the constants an and bn

n=[0:terms];

An=-(x1*dJ1)./(J1-x1*dJ1);
Bn=(2*n.^2.*J2)./(n.^2.*J2-x2*dJ2+x2^2*ddJ2);
Cn=-(0.5*x2^2-x1^2)*(J1-ddJ1)./(J1-x1*dJ1);
Dn=2*n.^2.*(J2-x2*dJ2)./(n.^2.*J2-x2*dJ2+x2^2*ddJ2);

Fn=0.5*rhof/rhoc*x2^2*(An-Bn)./(Cn-Dn);

dn=-(Fn.*J3-x3*dJ3)./(Fn.*H-x3*dH);

A=[real(dn);imag(dn)];
```

```
% CALCULATE THE DIRECTION VECTORS

factor=round(points/2);

counter=0;
totalpoints=(points+1)^2;

tic;

for a = 1:(points+1)
    for b= 1:(points+1)

        counter=counter+1;

        x=(a-factor-1)/points*2*gridsize;
        y=(b-factor-1)/points*2*gridsize;
        X1(a,b)=x;
        Y1(a,b)=y;

        if sqrt(x^2+y^2)>1

            % If the point is outside the fiber, the direction vectors are
calculated.
            % Otherwise, the direction vectors are set to zero.


            % EVALUATE dx AND dy AT x,y:
            % --------------------------


            clear delta v r B an bn;

            r=sqrt(x^2+y^2);
            THETAF=atan2(y,x)-flowangle;
            theta=atan2(-x,y);
            v=k*r*Rc;

            if (incident+reflected)>0

                % If calculating an acoustic effect (either incident or
reflected)
                % otherwise, the direction vectors are set only by the flow
solution


                n=0;
                W=0;
                X=0;

                dWdv=0;
                dWdtheta=0;
                dXdv=0;
                dXdtheta=0;

                ddWdv=0;
                ddWdtheta=0;
                ddXdv=0;
                ddXdtheta=0;

                ddWdvdtheta = 0;
                ddXdvdtheta = 0;


                % compute the required bessel functions

                J=zeros(terms+2,1);
                Y=zeros(terms+2,1);
```

```
for n = 1 : (terms+2);
    J(n)=besselj(n,v);
    Y(n)=bessely(n,v);
end

% if the reflected wave is being calculated, compute the terms
in the summation
% otherwise, the solution is for incident wave only, which is
much simpler

if reflected

    % calculate the first (n=0) term in the summation for W
and V
    % (and their derivatives) for the case of including the
reflected wave

    B=exp(-i*k*h)+exp(i*k*h);
    an=A(1,1);
    bn=A(2,1);

    W = B*((incident+an)*besselj(0,v)+bn*bessely(0,v));
    X = B*(bn*besselj(0,v)-an*bessely(0,v));

    dWdv = - B*((incident+an)*J(1) + bn*Y(1));
    dXdv = - B*(bn*J(1) - an*Y(1));

    ddWdv = - B*((incident+an)*(1/v*J(1)-J(2)) + bn*(1/v*Y(1)-
Y(2)));
    ddXdv = - B*(bn*(1/v*J(1)-J(2)) - an*(1/v*Y(1)-Y(2)));


    % calculate the next terms in the summation for W and V
    % (and their derivatives) for the case of including the
reflected wave

    for n = 1:terms

        B=2*(-i)^n*(exp(-i*k*h)+(-1)^n*exp(i*k*h));

        an=A(1,n+1);
        bn=A(2,n+1);

        Bc = B*cos(n*theta);
        Bs = B*sin(n*theta);

        dJ = n/v*J(n) - J(n+1);
        dY = n/v*Y(n) - Y(n+1);

        ddJ = -n/v^2*J(n) + n/v*dJ - (n+1)/v*J(n+1) + J(n+2);
        ddY = -n/v^2*Y(n) + n/v*dY - (n+1)/v*Y(n+1) + Y(n+2);

        Wt = Bc*((1+an)*J(n)+bn*Y(n));
        Xt = Bc*(bn*J(n)-an*Y(n));

        dWdv     = dWdv     +   Bc*((1+an)*dJ + bn*dY);
        dWdtheta = dWdtheta - n*Bs*((1+an)*J(n) + bn*Y(n));
        dXdv     = dXdv     +   Bc*(bn*dJ - an*dY);
        dXdtheta = dXdtheta - n*Bs*(bn*J(n) - an*Y(n));

        ddWdv     = ddWdv     + Bc*((1+an)*ddJ + bn*ddY);
        ddWdtheta = ddWdtheta - n^2*Bc*((1+an)*J(n) +
bn*Y(n));

        ddXdv     = ddXdv     + Bc*(bn*ddJ - an*ddY);
        ddXdtheta = ddXdtheta - n^2*Bc*(bn*J(n) - an*Y(n));
```

```
                ddWdvdtheta = ddWdvdtheta - n*Bs*((1+an)*dJ + bn*dY);
                ddXdvdtheta = ddXdvdtheta - n*Bs*(bn*dJ - an*dY);

                W = W + Wt;
                X = X + Xt;

                Wdiff = abs(Wt/W);
                Xdiff = abs(Xt/X);

                if (Wdiff>0)
                    if (Wdiff<1e-50) & (Xdiff<1e-50)
                        break;
                    end
                end
            end

        else

            % calculate the first (n=0) term in the summation for W
and V
            % (and their derivatives) for the case of only including
the incident wave

            B=exp(-i*k*h)+exp(i*k*h);

            W = B*besselj(0,v);

            dWdv = - B*J(1);

            ddWdv = - B*(1/v*J(1)-J(2));

            % calculate the next terms in the summation for W and V
            % (and their derivatives) for the case of only including
the incident wave

            for n = 1:terms

                B=2*(-i)^n*(exp(-i*k*h)+(-1)^n*exp(i*k*h));

                Bc = B*cos(n*theta);
                Bs = B*sin(n*theta);

                dJ = n/v*J(n) - J(n+1);
                ddJ = -n/v^2*J(n) + n/v*dJ - (n+1)/v*J(n+1) + J(n+2);

                Wt = Bc*J(n);

                dWdv     = dWdv     +   Bc*dJ;
                dWdtheta = dWdtheta - n*Bs*J(n);

                ddWdv     = ddWdv     + Bc*ddJ;
                ddWdtheta = ddWdtheta - n^2*Bc*J(n);

                ddWdvdtheta = ddWdvdtheta - n*Bs*dJ;

                W = W + Wt;

                Wdiff = abs(Wt/W);

                if (Wdiff>0)
                    if (Wdiff<1e-50)
                        break;
                    end
                end
            end
        end
```

```
                    dPdv      = 2*W*dWdv+2*X*dXdv;
                    dPdtheta = 2*W*dWdtheta+2*X*dXdtheta;

                    dVdv      = 2*dWdv*ddWdv + 2*dXdv*ddXdv - (2/v^3)*(dWdtheta^2 +
dXdtheta^2) + (2/v^2)*(dWdtheta*ddWdvdtheta + dXdtheta*ddXdvdtheta);
                    dVdtheta = 2*dWdv*ddWdvdtheta + 2*dXdv*ddXdvdtheta +
(2/v^2)*(dWdtheta*ddWdtheta + dXdtheta*ddXdtheta);

                    f1 = 1 - (cf^2*rhof)/(cp^2*rhop);
                    f2 = 2 * (rhop-rhof)/(2*rhop+rhof);

                    dUdv      = f1/6*dPdv      - f2/4*dVdv;
                    dUdtheta = f1/6*dPdtheta - f2/4*dVdtheta;


                    dxsound = 2*Gk/3*(dUdv*sin(theta)+dUdtheta*cos(theta)/v);
                    dysound = -2*Gk/3*(dUdv*cos(theta)-dUdtheta*sin(theta)/v);

                else
                    dxsound = 0;
                    dysound = 0;

                end

                dxflow = (log(r)-0.5*(1-1/r^2)*cos(2*(THETAF)))/(2.002-log(Re));
                dyflow = -(0.5*(1-1/r^2)*sin(2*(THETAF)))/(2.002-log(Re));

                if gravity
                    dxgrav = 1/Uf*2/9*Rp^2/mu*(rhop-rhof)*9.81*cos(gravangle);
                    dygrav = 1/Uf*2/9*Rp^2/mu*(rhop-rhof)*9.81*sin(gravangle);
                else
                    dxgrav = 0;
                    dygrav = 0;
                end


                dx=dxsound+dxgrav+dxflow*cos(flowangle)-dyflow*sin(flowangle);
                dy=dysound+dygrav+dyflow*cos(flowangle)+dxflow*sin(flowangle);


                % --------------------------

                % Estimated And Elapsed Time Calculation

                elapsedtime=toc/60;
                estimatedtime=elapsedtime/counter*totalpoints;


                % Display Estimated and Total Time

                Handle = findobj(gcbf,'Tag','ElapsedTime');
                set(Handle,'String',round(elapsedtime*100)/100);

                Handle = findobj(gcbf,'Tag','CompletionTime');
                set(Handle,'String',round(estimatedtime*100)/100);

                % --------------------------

                Fx(a,b)=dx;
                Fy(a,b)=dy;
                Fxu(a,b)=dx/sqrt(dx^2+dy^2);
                Fyu(a,b)=dy/sqrt(dx^2+dy^2);
            else
                Fx(a,b)=0;
                Fy(a,b)=0;
                Fxu(a,b)=0;
```

```
                Fyu(a,b)=0;
            end
        end

    end

    % set the button label
    Handle = findobj(gcbf,'Tag','ShowMagnitude');
    set(Handle,'String','show magnitude');

    scale=1.1;

    % plot the flow field
    quiver(X1,Y1,Fxu,Fyu,0.5,'g');


    % plot the data from file
    % get filename
    Handle = findobj(gcbf,'Tag','datafile');
    filename = ['c:\xcap\data\',char(get(Handle,'String'))];
    AAA=dlmread(filename);

    normlength=sqrt(AAA(:,4).^2+AAA(:,3).^2);

        [sizex sizey]=size(normlength);

        for m=1:sizex
            if (normlength(m)>0)
                    AAA(m,4)=AAA(m,4)/normlength(m);
                    AAA(m,3)=AAA(m,3)/normlength(m);

            end
        end

    hold on;
    quiver(-(AAA(:,2)./0.005482-500)/46.51,(AAA(:,1)/0.005482-530)/46.51,-
AAA(:,4),AAA(:,3),0.5,'r');



    % plot fiber as a circle
    hold on;
    th = (0:128)/128*2*pi;
    circx = cos(th);
    circy = sin(th);
    plot(circx,circy,'k','LineWidth',1.5);
    axis square;

    if (incident + reflected) > 0
        % plot lines to show nodes
        wavl=cf/freq/Rc;
        for n=0:5
            line1=(hinput + (2*n+1)/4)*wavl;
            line2=(hinput - (2*n+1)/4)*wavl;
            if (line1<gridsize*scale) & (line1>(-gridsize*scale))
                plot([-gridsize gridsize],[line1 line1],'--b','LineWidth',1.5);
            end
            if (line2<gridsize*scale) & (line2>(-gridsize*scale))
                plot([-gridsize gridsize],[line2 line2],'--b','LineWidth',1.5);
            end
        end
    end

    axis([-gridsize*scale,gridsize*scale,-gridsize*scale,gridsize*scale]);
    hold off;

    % save data as Lotus spreadsheet file
```

```
    wk1write('xn.wk1',X1);
    wk1write('yn.wk1',Y1);
    wk1write('fxn4.wk1',Fx);
    wk1write('fyn4.wk1',Fy);


case 'magnitude'

    % logitudinal sound speed in fluid [=] m/s
    Handle = findobj(gcbf,'Tag','FluidSoundSpeed');
    cf = str2num(get(Handle,'String'));

    % frequency of sound waves          [=] Hz
    Handle = findobj(gcbf,'Tag','Frequency');
    freq = str2num(get(Handle,'String'));
    w = 2*pi*freq;  % angular frequency                [=] rad/s
    k = w/cf;       % wavenumber in fluid              [=] 1/m

    % Calculate Incident Wave? (1=yes 0=no)
    Handle = findobj(gcbf,'Tag','IncidentWave');
    incident = get(Handle,'Value');

    % Calculate Reflected Wave? (1=yes 0=no)
    Handle = findobj(gcbf,'Tag','ReflectedWave');
    reflected = get(Handle,'Value');


    % radius of cylinder                  [=] m
    Handle = findobj(gcbf,'Tag','FiberRadius');
    Rc = str2num(get(Handle,'String'));

    % distance between nodal plane (velocity potential)
    %                       and cylinder axis          [=] m
    Handle = findobj(gcbf,'Tag','NodeOffset');
    hinput = str2num(get(Handle,'String'));
    h = -hinput*cf/freq;

    % Range
    Handle = findobj(gcbf,'Tag','Range');
    gridsize = str2num(get(Handle,'String'));

    % load data
    X1 = wk1read('xn.wk1');
    Y1 = wk1read('yn.wk1');
    Fx = wk1read('fxn4.wk1');
    Fy = wk1read('fyn4.wk1');

    % get the button label
    Handle = findobj(gcbf,'Tag','ShowMagnitude');
    label = get(Handle,'String');

    % if showing magnitude, plot the data unaltered
    % if showing the normalized plot, normalize first!
    if strcmp(label,'show normalized')

        Fxplot=Fx;
        Fyplot=Fy;

        normlength=sqrt(Fx.^2+Fy.^2);

        [sizex sizey]=size(normlength);

        for m=1:sizex
            for n=1:sizey
                if (normlength(m,n)>0)
                    Fxplot(m,n)=Fx(m,n)/normlength(m,n);
                    Fyplot(m,n)=Fy(m,n)/normlength(m,n);
```

```
            end

        end
    end


    % plot the flow field
    quiver(X1,Y1,Fxplot,Fyplot,.5);

    set(Handle,'String','show magnitude');
else
    Fxplot=Fx;
    Fyplot=Fy;

    % plot the flow field
    quiver(X1,Y1,Fxplot,Fyplot);

    set(Handle,'String','show normalized');
end

scale=1.1;


% plot fiber as a circle
hold on;
th = (0:128)/128*2*pi;
circx = cos(th);
circy = sin(th);
plot(circx,circy,'k','LineWidth',1.5);
axis square;

if (incident + reflected) > 0
    % plot lines to show nodes
    wavl=cf/freq/Rc;
    for n=0:5
        line1=(hinput + (2*n+1)/4)*wavl;
        line2=(hinput - (2*n+1)/4)*wavl;
        if (line1<gridsize*scale) & (line1>(-gridsize*scale))
            plot([-gridsize gridsize],[line1 line1],'--r','LineWidth',1.5);
        end
        if (line2<gridsize*scale) & (line2>(-gridsize*scale))
            plot([-gridsize gridsize],[line2 line2],'--r','LineWidth',1.5);
        end
    end
end

axis([-gridsize*scale,gridsize*scale,-gridsize*scale,gridsize*scale]);
hold off;


case 'trajectory'

    % GET INPUT DATA

    % Fluid Properties

    % free flow velocity                [=] m/s
    Handle = findobj(gcbf,'Tag','FluidVelocity');
    Uf = str2num(get(Handle,'String'));

    % density of fluid                  [=] kg/m^3
    Handle = findobj(gcbf,'Tag','FluidDensity');
    rhof = str2num(get(Handle,'String'));

    % viscosity of fluid                [=] kg/(m s)
    Handle = findobj(gcbf,'Tag','FluidViscosity');
```

```
mu = str2num(get(Handle,'String'));

% logitudinal sound speed in fluid [=] m/s
Handle = findobj(gcbf,'Tag','FluidSoundSpeed');
cf = str2num(get(Handle,'String'));

% flow angle in pi radians
Handle = findobj(gcbf,'Tag','FlowAngle');
flowangle = pi*str2num(get(Handle,'String'));


% Particle Properties

% density of particle                [=] kg/m^3
Handle = findobj(gcbf,'Tag','ParticleDensity');
rhop = str2num(get(Handle,'String'));

% radius of spherical particle       [=] m
Handle = findobj(gcbf,'Tag','ParticleRadius');
Rp = str2num(get(Handle,'String'));

% logitudinal sound speed in particle [=] m/s
Handle = findobj(gcbf,'Tag','ParticleLongitudinal');
cp = str2num(get(Handle,'String'));


% Fiber (Cylinder) Properties

% density of cylinder                [=] kg/m^3
Handle = findobj(gcbf,'Tag','FiberDensity');
rhoc = str2num(get(Handle,'String'));

% radius of cylinder                 [=] m
Handle = findobj(gcbf,'Tag','FiberRadius');
Rc = str2num(get(Handle,'String'));

% logitudinal sound speed in cylinder [=] m/s
Handle = findobj(gcbf,'Tag','FiberLongitudinal');
c1 = str2num(get(Handle,'String'));

% shear sound speed in cylinder      [=] m/s
Handle = findobj(gcbf,'Tag','FiberTransverse');
c2 = str2num(get(Handle,'String'));


% Acoustic Field Properties

% frequency of sound waves         [=] Hz
Handle = findobj(gcbf,'Tag','Frequency');
freq = str2num(get(Handle,'String'));

w = 2*pi*freq;  % angular frequency              [=] rad/s
k = w/cf;       % wavenumber in fluid            [=] 1/m

% energy density of acoustic field [=] J/m^3
Handle = findobj(gcbf,'Tag','EnergyDensity');
Eac = str2num(get(Handle,'String'));
%Eac = Gkn*mu*Uf/k/Rp^2;

% distance between nodal plane (velocity potential)
%                        and cylinder axis        [=] m
Handle = findobj(gcbf,'Tag','NodeOffset');
hinput = str2num(get(Handle,'String'));
h = -hinput*cf/freq;

% Calculate Incident Wave? (1=yes 0=no)
Handle = findobj(gcbf,'Tag','IncidentWave');
```

```
incident = get(Handle,'Value');

% Calculate Reflected Wave? (1=yes 0=no)
Handle = findobj(gcbf,'Tag','ReflectedWave');
reflected = get(Handle,'Value');

% Gravity Options

% Calculate Gravity? (1=yes 0=no)
Handle = findobj(gcbf,'Tag','Gravity');
gravity = get(Handle,'Value');

% gravity angle in pi radians
Handle = findobj(gcbf,'Tag','GravAngle');
gravangle = pi*str2num(get(Handle,'String'));


% Plot Options

% Range
Handle = findobj(gcbf,'Tag','Range');
gridsize = str2num(get(Handle,'String'));

% Number of Points
Handle = findobj(gcbf,'Tag','GridPoints');
points = str2num(get(Handle,'String'));

% Starting X value
Handle = findobj(gcbf,'Tag','TrajX');
x = str2num(get(Handle,'String'));

% Starting Y value
Handle = findobj(gcbf,'Tag','TrajY');
y = str2num(get(Handle,'String'));

% Completion Time
Handle = findobj(gcbf,'Tag','Completion');
set(Handle,'String','Maximum Completion Time');



terms=100;

Gk=Rp^2*k*Eac/(mu*Uf);
Re=2*rhof*Uf*Rc/mu;

totalpoints=2500;
tic;


% Get the functions an and bn (where dn=an+i*bn) A=[an bn]

clear x1 x2 x3 n dn ddn J1 dJ1 ddJ1 J2 dJ2 ddJ2 J3 dJ3 H dH An Bn Cn Dn Fn dn
a b;

x1=w*Rc/c1;
x2=w*Rc/c2;
x3=k*Rc;

% compute the required bessel functions for an and bn

n   = [0:terms+2];
dn  = [0:terms+1];
ddn = [0:terms  ];

J1   = besselj(n,x1);
```

```
        dJ1  = dn/x1.*J1(1:terms+2) - J1(2:terms+3);
        ddJ1 = -ddn/x1^2.*J1(1:terms+1) + ddn/x1.*dJ1(1:terms+1) - dJ1(2:terms+2);
        J1   = J1(1:terms+1);
        dJ1  = dJ1(1:terms+1);

        J2   = besselj(n,x2);
        dJ2  = dn/x2.*J2(1:terms+2) - J2(2:terms+3);
        ddJ2 = -ddn/x2^2.*J2(1:terms+1) + ddn/x2.*dJ2(1:terms+1) - dJ2(2:terms+2);
        J2   = J2(1:terms+1);
        dJ2  = dJ2(1:terms+1);

        J3   = besselj(n,x3);
        dJ3  = dn/x3.*J3(1:terms+2) - J3(2:terms+3);
        J3   = J3(1:terms+1);
        dJ3  = dJ3(1:terms+1);

        H    = besselh(n,x3);
        dH   = dn/x3.*H(1:terms+2) - H(2:terms+3);
        H    = H(1:terms+1);
        dH   = dH(1:terms+1);

        % calculate the constants an and bn

        n=[0:terms];

        An=-(x1*dJ1)./(J1-x1*dJ1);
        Bn=(2*n.^2.*J2)./(n.^2.*J2-x2*dJ2+x2^2*ddJ2);
        Cn=-(0.5*x2^2-x1^2)*(J1-ddJ1)./(J1-x1*dJ1);
        Dn=2*n.^2.*(J2-x2*dJ2)./(n.^2.*J2-x2*dJ2+x2^2*ddJ2);

        Fn=0.5*rhof/rhoc*x2^2*(An-Bn)./(Cn-Dn);

        dn=-(Fn.*J3-x3*dJ3)./(Fn.*H-x3*dH);

        A=[real(dn);imag(dn)];


        % CALCULATE THE DIRECTION VECTORS

        counter=0;

        while (abs(x) <= gridsize) & (abs(y) <= gridsize) & (sqrt(x^2+y^2) > 1) &
(counter<=totalpoints)

            hold on;

            plot(x,y,'g.');

            counter=counter+1;


            % --------------------------
            % EVALUATE dx AND dy AT x,y:
            % --------------------------


            clear delta v r B an bn;

            r=sqrt(x^2+y^2);
            THETAF=atan2(y,x)-flowangle;
            theta=atan2(-x,y);
            v=k*r*Rc;

            if (incident+reflected)>0

                % If calculating an acoustic effect (either incident or reflected)
                % otherwise, the direction vectors are set only by the flow solution
```

```
n=0;
W=0;
X=0;

dWdv=0;
dWdtheta=0;
dXdv=0;
dXdtheta=0;

ddWdv=0;
ddWdtheta=0;
ddXdv=0;
ddXdtheta=0;

ddWdvdtheta = 0;
ddXdvdtheta = 0;


% compute the required bessel functions

J=zeros(terms+2,1);
Y=zeros(terms+2,1);

for n = 1 : (terms+2);
    J(n)=besselj(n,v);
    Y(n)=bessely(n,v);
end

% if the reflected wave is being calculated, compute the terms in the
summation
% otherwise, the solution is for incident wave only, which is much
simpler

if reflected

    % calculate the first (n=0) term in the summation for W and V
    % (and their derivatives) for the case of including the reflected
wave

    B=exp(-i*k*h)+exp(i*k*h);
    an=A(1,1);
    bn=A(2,1);

    W = B*((incident+an)*besselj(0,v)+bn*bessely(0,v));
    X = B*(bn*besselj(0,v)-an*bessely(0,v));

    dWdv = - B*((incident+an)*J(1) + bn*Y(1));
    dXdv = - B*(bn*J(1) - an*Y(1));

    ddWdv = - B*((incident+an)*(1/v*J(1)-J(2)) + bn*(1/v*Y(1)-Y(2)));
    ddXdv = - B*(bn*(1/v*J(1)-J(2)) - an*(1/v*Y(1)-Y(2)));


    % calculate the next terms in the summation for W and V
    % (and their derivatives) for the case of including the reflected
wave

    for n = 1:terms

        B=2*(-i)^n*(exp(-i*k*h)+(-1)^n*exp(i*k*h));

        an=A(1,n+1);
        bn=A(2,n+1);

        Bc = B*cos(n*theta);
        Bs = B*sin(n*theta);
```

```
                dJ = n/v*J(n) - J(n+1);
                dY = n/v*Y(n) - Y(n+1);

                ddJ = -n/v^2*J(n) + n/v*dJ - (n+1)/v*J(n+1) + J(n+2);
                ddY = -n/v^2*Y(n) + n/v*dY - (n+1)/v*Y(n+1) + Y(n+2);

                Wt = Bc*((1+an)*J(n)+bn*Y(n));
                Xt = Bc*(bn*J(n)-an*Y(n));

                dWdv     = dWdv     +   Bc*((1+an)*dJ + bn*dY);
                dWdtheta = dWdtheta - n*Bs*((1+an)*J(n) + bn*Y(n));
                dXdv     = dXdv     +   Bc*(bn*dJ - an*dY);
                dXdtheta = dXdtheta - n*Bs*(bn*J(n) - an*Y(n));

                ddWdv     = ddWdv     + Bc*((1+an)*ddJ + bn*ddY);
                ddWdtheta = ddWdtheta - n^2*Bc*((1+an)*J(n) + bn*Y(n));
                ddXdv     = ddXdv     + Bc*(bn*ddJ - an*ddY);
                ddXdtheta = ddXdtheta - n^2*Bc*(bn*J(n) - an*Y(n));

                ddWdvdtheta = ddWdvdtheta - n*Bs*((1+an)*dJ + bn*dY);
                ddXdvdtheta = ddXdvdtheta - n*Bs*(bn*dJ - an*dY);

                W = W + Wt;
                X = X + Xt;

                Wdiff = abs(Wt/W);
                Xdiff = abs(Xt/X);

                if (Wdiff>0)
                    if (Wdiff<1e-50) & (Xdiff<1e-50)
                        break;
                    end
                end
            end

        else

            % calculate the first (n=0) term in the summation for W and V
            % (and their derivatives) for the case of only including the
incident wave

            B=exp(-i*k*h)+exp(i*k*h);

            W = B*besselj(0,v);

            dWdv = - B*J(1);

            ddWdv = - B*(1/v*J(1)-J(2));

            % calculate the next terms in the summation for W and V
            % (and their derivatives) for the case of only including the
incident wave

            for n = 1:terms

                B=2*(-i)^n*(exp(-i*k*h)+(-1)^n*exp(i*k*h));

                Bc = B*cos(n*theta);
                Bs = B*sin(n*theta);

                dJ = n/v*J(n) - J(n+1);
                ddJ = -n/v^2*J(n) + n/v*dJ - (n+1)/v*J(n+1) + J(n+2);

                Wt = Bc*J(n);

                dWdv     = dWdv     +   Bc*dJ;
```

```
                        dWdtheta = dWdtheta - n*Bs*J(n);

                        ddWdv      = ddWdv      + Bc*ddJ;
                        ddWdtheta = ddWdtheta - n^2*Bc*J(n);

                        ddWdvdtheta = ddWdvdtheta - n*Bs*dJ;

                        W = W + Wt;

                        Wdiff = abs(Wt/W);

                        if (Wdiff>0)
                            if (Wdiff<1e-50)
                                break;
                            end
                        end
                    end
                end


                dPdv     = 2*W*dWdv+2*X*dXdv;
                dPdtheta = 2*W*dWdtheta+2*X*dXdtheta;

                dVdv     = 2*dWdv*ddWdv + 2*dXdv*ddXdv - (2/v^3)*(dWdtheta^2 +
dXdtheta^2) + (2/v^2)*(dWdtheta*ddWdvdtheta + dXdtheta*ddXdvdtheta);
                dVdtheta = 2*dWdv*ddWdvdtheta + 2*dXdv*ddXdvdtheta +
(2/v^2)*(dWdtheta*ddWdtheta + dXdtheta*ddXdtheta);

                f1 = 1 - (cf^2*rhof)/(cp^2*rhop);
                f2 = 2 * (rhop-rhof)/(2*rhop+rhof);

                dUdv     = f1/6*dPdv     - f2/4*dVdv;
                dUdtheta = f1/6*dPdtheta - f2/4*dVdtheta;


                dxsound = 2*Gk/3*(dUdv*sin(theta)+dUdtheta*cos(theta)/v);
                dysound = -2*Gk/3*(dUdv*cos(theta)-dUdtheta*sin(theta)/v);

            else
                dxsound = 0;
                dysound = 0;
            end


            dxflow = (log(r)-0.5*(1-1/r^2)*cos(2*(THETAF)))/(2.002-log(Re));
            dyflow = -(0.5*(1-1/r^2)*sin(2*(THETAF)))/(2.002-log(Re));

            if gravity
                dxgrav = 1/Uf*2/9*Rp^2/mu*(rhop-rhof)*9.81*cos(gravangle);
                dygrav = 1/Uf*2/9*Rp^2/mu*(rhop-rhof)*9.81*sin(gravangle);
            else
                dxgrav = 0;
                dygrav = 0;
            end


            dx=dxsound+dxgrav+dxflow*cos(flowangle)-dyflow*sin(flowangle);
            dy=dysound+dygrav+dyflow*cos(flowangle)+dxflow*sin(flowangle);

            x=x+0.0025*gridsize/sqrt(dx^2+dy^2)*dx;
            y=y+0.0025*gridsize/sqrt(dx^2+dy^2)*dy;


            % -------------------------

            % Estimated And Elapsed Time Calculation
```

```
        elapsedtime=toc/60;
        estimatedtime=elapsedtime/counter*totalpoints;


        % Display Estimated and Total Time

        Handle = findobj(gcbf,'Tag','ElapsedTime');
        set(Handle,'String',round(elapsedtime*100)/100);

        Handle = findobj(gcbf,'Tag','CompletionTime');
        set(Handle,'String',round(estimatedtime*100)/100);

        % --------------------------


    end

    hold off;


case 'calcgorkov'

    % free flow velocity                [=] m/s
    Handle = findobj(gcbf,'Tag','FluidVelocity');
    Uf = str2num(get(Handle,'String'));

    % viscosity of fluid                [=] kg/(m s)
    Handle = findobj(gcbf,'Tag','FluidViscosity');
    mu = str2num(get(Handle,'String'));

    % radius of spherical particle        [=] m
    Handle = findobj(gcbf,'Tag','ParticleRadius');
    Rp = str2num(get(Handle,'String'));

    % logitudinal sound speed in fluid [=] m/s
    Handle = findobj(gcbf,'Tag','FluidSoundSpeed');
    cf = str2num(get(Handle,'String'));

    % frequency of sound waves          [=] Hz
    Handle = findobj(gcbf,'Tag','Frequency');
    freq = str2num(get(Handle,'String'));
    w = 2*pi*freq;  % angular frequency                [=] rad/s
    k = w/cf;       % wavenumber in fluid              [=] 1/m

    % energy density of acoustic field [=] J/m^3
    Handle = findobj(gcbf,'Tag','EnergyDensity');
    Eac = str2num(get(Handle,'String'));

    % Gorkov number
    Gk=Rp^2*k*Eac/(mu*Uf);
    Handle = findobj(gcbf,'Tag','GorkovNumber');
    set(Handle,'String',Gk);



case 'calcenergy'

    % free flow velocity                [=] m/s
    Handle = findobj(gcbf,'Tag','FluidVelocity');
    Uf = str2num(get(Handle,'String'));

    % viscosity of fluid                [=] kg/(m s)
    Handle = findobj(gcbf,'Tag','FluidViscosity');
    mu = str2num(get(Handle,'String'));
```

```
    % radius of spherical particle        [=] m
    Handle = findobj(gcbf,'Tag','ParticleRadius');
    Rp = str2num(get(Handle,'String'));

    % logitudinal sound speed in fluid [=] m/s
    Handle = findobj(gcbf,'Tag','FluidSoundSpeed');
    cf = str2num(get(Handle,'String'));

    % frequency of sound waves         [=] Hz
    Handle = findobj(gcbf,'Tag','Frequency');
    freq = str2num(get(Handle,'String'));
    w = 2*pi*freq;  % angular frequency                [=] rad/s
    k = w/cf;       % wavenumber in fluid              [=] 1/m

    % Gorkov number
    Handle = findobj(gcbf,'Tag','GorkovNumber');
    Gk = str2num(get(Handle,'String'));

    % energy density of acoustic field [=] J/m^3
    Eac = Gk*mu*Uf/k/Rp^2;
    Handle = findobj(gcbf,'Tag','EnergyDensity');
    set(Handle,'String',Eac);


case 'calcreynolds'

    % free flow velocity               [=] m/s
    Handle = findobj(gcbf,'Tag','FluidVelocity');
    Uf = str2num(get(Handle,'String'));

    % viscosity of fluid               [=] kg/(m s)
    Handle = findobj(gcbf,'Tag','FluidViscosity');
    mu = str2num(get(Handle,'String'));

    % density of fluid                 [=] kg/m^3
    Handle = findobj(gcbf,'Tag','FluidDensity');
    rhof = str2num(get(Handle,'String'));

    % radius of cylinder                 [=] m
    Handle = findobj(gcbf,'Tag','FiberRadius');
    Rc = str2num(get(Handle,'String'));

    % Reynolds number
    Re=2*rhof*Uf*Rc/mu;
    Handle = findobj(gcbf,'Tag','ReynoldsNumber');
    set(Handle,'String',Re);


case 'calcvelocity'

    % Reynolds number
    Handle = findobj(gcbf,'Tag','ReynoldsNumber');
    Re = str2num(get(Handle,'String'));

    % viscosity of fluid               [=] kg/(m s)
    Handle = findobj(gcbf,'Tag','FluidViscosity');
    mu = str2num(get(Handle,'String'));

    % density of fluid                 [=] kg/m^3
    Handle = findobj(gcbf,'Tag','FluidDensity');
    rhof = str2num(get(Handle,'String'));

    % radius of cylinder                 [=] m
    Handle = findobj(gcbf,'Tag','FiberRadius');
    Rc = str2num(get(Handle,'String'));
```

```
        % free flow velocity                [=] m/s
        Uf=Re*mu/2/rhof/Rc;
        Handle = findobj(gcbf,'Tag','FluidVelocity');
        set(Handle,'String',Uf);


    case 'fiberprop'

        % fibername is a vector with the name of each material
        % fiberdata contains the data from each material
        %   each row of fiberdata corresponds to the same row (material) in fibername
        %   the first column of fiberdata is the density in kg/m3
        %   the second column is the logitudinal sound speed in m/s
        %   the third column is the transverse sound speed in m/s

        %   fibername={'foamex';'s. steel';'aluminum';'nylon';'water'};

        fiberdata=[1230 2430 1200; 2700 6420 3040; 7900 5790 3100; 1120 2600 1100;
1000 1480 1480];

        Handle = findobj(gcbf,'Tag','FiberProp');
        material = get(Handle,'Value');

        % Change properties

        % density of cylinder                [=] kg/m^3
        Handle = findobj(gcbf,'Tag','FiberDensity');
        set(Handle,'String',fiberdata(material,1));

        % logitudinal sound speed in cylinder [=] m/s
        Handle = findobj(gcbf,'Tag','FiberLongitudinal');
        set(Handle,'String',fiberdata(material,2));

        % shear sound speed in cylinder       [=] m/s
        Handle = findobj(gcbf,'Tag','FiberTransverse');
        set(Handle,'String',fiberdata(material,3));

    case 'particleprop'

        % particlename is a vector with the name of each material
        % particledata contains the data from each material
        %   each row of fiberdata corresponds to the same row (material) in fibername
        %   the first column of fiberdata is the density in kg/m3
        %   the second column is the logitudinal sound speed in m/s

        %   particlename={'polystyrene';'ploye thylene';'silica'};

        particledata=[1050 2300; 900 1950; 2200 5700];

        Handle = findobj(gcbf,'Tag','ParticleProp');
        material = get(Handle,'Value');

        % Change properties

        % density of cylinder                [=] kg/m^3
        Handle = findobj(gcbf,'Tag','ParticleDensity');
        set(Handle,'String',particledata(material,1));

        % logitudinal sound speed in cylinder [=] m/s
        Handle = findobj(gcbf,'Tag','ParticleLongitudinal');
        set(Handle,'String',particledata(material,2));


    case 'fluidprop'

        % fluidname is a vector with the name of each material
```

```
% fluiddata contains the data from each material
%   each row of fiberdata corresponds to the same row (material) in fibername
%   the first column of fiberdata is the density in kg/m3
%   the second column is the logitudinal sound speed in m/s
%   the third column is the viscosity in kg/(m s)

%   fluidname={'water';'mineral oil';'glycerol'};

fluiddata=[1000 1480 0.001; 825 1440 0.002; 1260 1904 0.005];

Handle = findobj(gcbf,'Tag','FluidProp');
material = get(Handle,'Value');
fluiddata(material);

% Change properties

% density of cylinder                [=] kg/m^3
Handle = findobj(gcbf,'Tag','FluidDensity');
set(Handle,'String',fluiddata(material,1));

% logitudinal sound speed in cylinder [=] m/s
Handle = findobj(gcbf,'Tag','FluidSoundSpeed');
set(Handle,'String',fluiddata(material,2));

% shear sound speed in cylinder      [=] m/s
Handle = findobj(gcbf,'Tag','FluidViscosity');
set(Handle,'String',fluiddata(material,3));



end
```

MATLAB Code for Integrated Model

```
function [X, T, N, C]=overallnew(data)

%  This MATLAB function computes the concentration of particles
%  in the acoustic separation device,
%  N [=] particles/vol,
%  for a given position along
%  the length of the chamber, X [=] m,
%  and time, T [=] s
%  C [=] particles/vol
%  is the concentration of particles in the suspension

%  ---------------
%  Initialize Data
%  ---------------

% Overall Model Parameters

% capture radius deterioration coeff [=] dimensionless
% 0 <= gam <= 2
gam = data(1);

% randomness factor for mesh fibers  [=] dimensionless
f = data(2);


% Experimental System Properties

% length of chamber                  [=] m
Length = data(3);

%  Cross-sectional area of chamber   [=] m^2
Area = data(4);

% maximum particle concentration     [=] vol %
Concmax = data(5);

% porosity of mesh                   [=] kg/m^3
eo = data(6);

% free flow linear velocity of fluid [=] m/s
Uf = data(7);


% Particle Properties

% density of particle                 [=] kg/m^3
rhop = data(8);

% radius of spherical particle        [=] m
Rp = data(9);


% Fiber (Cylinder) Properties

% radius of cylinder                  [=] m
Rc = data(10);


% concentration of inlet              [=] kg/m^3
Conc = data(11);
```

```
% capture length from model           [=] fiber radiii
CAP = data(12);

% maximum time                        [=] s
Tmax = data(13);


% -----------------
% Convert variables
% -----------------

% The dimensionless scale for the solution is based on a unit
% cross-sectional area
scale = sqrt(Area);

% scaled entrance velocity of suspension
vo = Uf/scale;

% chamber length
L=Length/scale;

% fiber radius
a = Rc/scale;

% capture "radius"
Rcao = CAP/2;

% initial concentration of suspension [=] particles / vol(scaled)
Co = Conc/rhop/(4/3*pi*Rp^3)*scale^3;

% maximum concentration of trapped particles [=] particles / vol(scaled)
Nt = Concmax/(4/3*pi*Rp^3)*scale^3;


% Characteristic capture length
Lo = pi*a/(f*(1-eo)*Rcao);

To = Lo*Nt/(Co*vo);

% Create solution space
tpoints = 5001;
tstep = Tmax/(tpoints-1);
xstep = tstep*vo/eo;
xpoints = ceil(L/xstep)+1;

T = 0 : tstep : Tmax;

X = zeros(1,xpoints);

for counter = 2: xpoints
    X(counter) = X(counter-1) + xstep;
end


C = zeros(xpoints,tpoints);
C(:,1)=Co;
C(1,:)=Co;

N = zeros(tpoints,xpoints);

dNdT = zeros(1,tpoints);
tic;
for xpoint = 1 : xpoints

    fprintf('%d of %d.  Time = %0.5g min\n',xpoint,xpoints,toc/60);

    % solve dN/dT = vo/Lo G C to obtain N(T) for a given x
```

```
    const =  vo/Lo*C(xpoint,:)';
    [t,N(:,xpoint)] = ode45(@magsep2, T, 0, [], const, Nt, gam, T);

    % evaluate dN/dT
    dNdT(1)=(-3*N(1,xpoint)+4*N(2,xpoint)-N(3,xpoint))/2/tstep;
    for ii = 2:(tpoints-1)
        dNdT(ii)=(N(ii+1,xpoint)-N(ii-1,xpoint))/2/tstep;
    end
    dNdT(tpoints)=(3*N(tpoints,xpoint)-4*N(tpoints-1,xpoint)+N(tpoints-
2,xpoint))/2/tstep;

    % use dN/dT in dN/dT + vo dC/dX = 0 to find dC/dX
    dCdx = -1/vo*dNdT;

    % use dC/dX to find next C
    for ii = 2 : tpoints
        C(xpoint+1,ii)=C(xpoint,ii-1)+dCdx(ii-1)*xstep;
    end
end

% normalize concentrations
N=N./Nt;
C=C./Co;

figure;
plot(T/60,C(xpoints,:));
```

References

1. M.Y. Corapcioglu (ed.), *Advances in Porous Media*, Elesevier Science Publishers, New York (1991).

2. S. Gupta, D.L. Feke, *A.I.Ch.E. Journal*, **44**(5), 1005-1014 (1998).

3. T.D. Rossing, N.H. Fletcher, *Principles of Vibration and Sound*, Springer-Verlag, New York (1995).

4. R. Yosioka, G Kawasima, *Acoustica,* **5**, 167 (1955).

5. T.L. Tolt, D. L. Feke, *Proc. I.E.C.E.C.* **4**, 327 (1988).

6. T.L. Tolt, D.L. Feke, *Journal of the Acoustical Society of America* **91**(6), 3152 (1992).

7. T.L. Tolt, D.L. Feke, *Chemical Engineering Science* **48**, 527-540 (1993).

8. Z.I. Mandralis, D.L. Feke, *AIChE Journal* **39**(2), 197-206 (1993).

9. Z.I. Mandralis, W. Bolek, W. Burger, E. Benes, D.L. Feke, *Ultrasonics* **32**(2), 113-121, (1994).

10. Z.I. Mandralis, D.L. Feke, *Chemical Engineering Science* **48**(23), 3897-3905 (1993).

11. S. Gupta, D.L. Feke, I. Manas-Zloczower, *Chemical Engineering Science* **50**(20), 3275-3284 (1995).

12. D.A. Johnson, D.L. Feke, *Sepn. Technol.* **5**, 251-258 (1995).

13. S. Gupta, D.L. Feke, *Ultrasonics* **35**, 131-139 (1997).

14. D.H. Hill, D.L. Feke, *Separation Science and Technology*, **35**(9), 1363-75 (2000).

15. J.S. Fine, M.S. Thesis, Case Western Reserve University (1999).

16. G. Pangu, M.S. Thesis, Case Western Reserve University (2003).

17. W. Viessman, Jr., M.J. Hammer, *Water Supply and Pollution Control*, Harper Collins, New York (1993).

18. G. Whitworth, M.A. Grundy, W.T. Coakley, *Ultrasonics* **29**, 439 (1991).

19. A. Frank, W. Bolek, M. Groschl, W. Burger, E. Benes, *Proc. Ultrasonics Intl. Conf.*, 519 (1993).

20. H. Bohm, P. Anthony, M.R. Davey, L.G. Briarty, J.B. Power, K.C. Lowe, E. Benes, M. Groschl, *Ultrasonics* **38**, 629 (2000).

21. S. Radel, A.J. McLoughlin, L. Gheradini, O. Doblhoff-Dier, E. Benes, *Ultrasonics* **38**, 633 (2000).

22. K. Yasuda, S.S. Haupt, S. Umemura, T. Yagi, M. Nishida, Y. Shibata, *J. of Acoust. Soc. Am.* **102**(1), 642 (1997).

23. R. Allman, W.T. Coakley, *Bioseparation* **4**, 29 (1994).

24. O. Doblhoff-Dier, T. Gaida, H. Katinger, W. Burger, M. Groschl, E. Benes, *Biotechnology Progress* **10**, 428 (1994).

25. M.S. Limaye, J.J. Hawkes, W.T. Coakley, *Journal of Microbiological Methods* **27**(2-3), 211 (1996).

26. J.J. Hawkes, W.T. Coakley, *Enzyme and Microbial Technology* **19**(1), 57 (1996).

27 K. Yasuda, *Sensors and Actuators B-Chemical* **64**(1-3), 128 (2000).

28. R.A. Barnes, P. Jenkins,W.T. Coakley, *Arch. Dis. Childhood* **78**, 58 (1998).

29. C.M. Cousins, P. Holownia, J.J. Hawkes, M.S. Limaye, C.P. Price, P. Keay, W.T. Coakley, *Ultrasound Med Biol* **26**, 881 (2000).

30. R. Darby, *Chemical Engineering Fluid Mechanics*, Marcel Dekker, New York (1996).

31. H. Lamb, *Hydrodynamics, 6th ed.*, Cambridge Univ. Press, London (1932).

32. M. Van Dyke, *Perturbation Methods in Fluid Mechanics*, Parabolic Press, Stanford, California (1975).

33. L.P. Gor'kov, *Sov. Phys. Dokl.* **6**, 773 (1962).

34. M. Barmatz, P. Collas, *J. Acoust. Soc. Am.* 77,928 (1985).

35. T. Hasegawa, K. Saka, N. Inoue, K. Matsuzawa, *J. Acoust. Soc. Am.* **83**, 1770 (1988).

36. J. Faran, *J. Acoust. Soc. Am.* **23**, 405 (1951).

37. S. Gupta, Ph.D. Thesis, Case Western Reserve University (1997).

38. S.E. Schwarz, W.G. Oldham, *Electrical Engineering: An Introduction*, Oxford University Press, New York (1993).

39. D. Rusinko, M.S. Thesis, Case Western Reserve University (2001).

40. R. Gerber, R.R. Birss, *High Gradient Magnetic Separation*, John Wily & Sons, New York (1983).

41. R. Gerber, M.H. Watmough, *IEEE Trans. Mag.* **18**(6), 1671 (1982).

42. D.L. Feke, Personal Communication.

43. P.J. Grabenstetter, J.M. Belovich, *Biotechnology Progress* (in preparation).

44. J.M. Belovich, Z. Wang, Personal Communication.

Bibliography

R. Allman, W.T. Coakley, *Bioseparation* **4**, 29 (1994).

M. Barmatz, P. Collas, *J. Acoust. Soc. Am.* **77**,928 (1985).

R.A. Barnes, P. Jenkins,W.T. Coakley, *Arch. Dis. Childhood* **78**, 58 (1998).

J.M. Belovich, Z. Wang, Personal Communication.

H. Bohm, P. Anthony, M.R. Davey, L.G. Briarty, J.B. Power, K.C. Lowe, E. Benes, M. Groschl, *Ultrasonics* **38**, 629 (2000).

M.Y. Corapcioglu (ed.), *Advances in Porous Media*, Elesevier Science Publishers, New York (1991).

C.M. Cousins, P. Holownia, J.J. Hawkes, M.S. Limaye, C.P. Price, P. Keay, W.T. Coakley, *Ultrasound Med Biol* **26**, 881 (2000).

R. Darby, *Chemical Engineering Fluid Mechanics*, Marcel Dekker, New York (1996).

O. Doblhoff-Dier, T. Gaida, H. Katinger, W. Burger, M. Groschl, E. Benes, *Biotechnology Progress* **10**, 428 (1994).

J. Faran, *J. Acoust. Soc. Am.* **23**, 405 (1951).

D.L. Feke, Personal Communication.

J.S. Fine, M.S. Thesis, Case Western Reserve University (1999).

A. Frank, W. Bolek, M. Groschl, W. Burger, E. Benes, *Proc. Ultrasonics Intl. Conf.*, 519 (1993).

R. Gerber, M.H. Watmough, *IEEE Trans. Mag.* **18**(6), 1671 (1982).

R. Gerber, R.R. Birss, *High Gradient Magnetic Separation*, John Wily & Sons, New York (1983).

P.J. Grabenstetter, J.M. Belovich, *Biotechnology Progress* (in preparation).

L.P. Gor'kov, *Sov. Phys. Dokl.* **6**, 773 (1962).

S. Gupta, D.L. Feke, I. Manas-Zloczower, *Chemical Engineering Science* **50**(20), 3275-3284 (1995).

S. Gupta, Ph.D. Thesis, Case Western Reserve University (1997).

S. Gupta, D.L. Feke, *Ultrasonics* **35**, 131-139 (1997).

S. Gupta, D.L. Feke, *A.I.Ch.E. Journal*, **44**(5), 1005-1014 (1998).

T. Hasegawa, K. Saka, N. Inoue, K. Matsuzawa, *J. Acoust. Soc. Am.* **83**, 1770 (1988).

J.J. Hawkes, W.T. Coakley, *Enzyme and Microbial Technology* **19**(1), 57 (1996).

D.H. Hill, D.L. Feke, *Separation Science and Technology*, **35**(9), 1363-75 (2000).

D.A. Johnson, D.L. Feke, *Sepn. Technol.* **5**, 251-258 (1995).

M.S. Limaye, J.J. Hawkes, W.T. Coakley, *Journal of Microbiological Methods* **27**(2-3), 211 (1996).

H. Lamb, *Hydrodynamics, 6th ed.*, Cambridge Univ. Press, London (1932).

Z.I. Mandralis, D.L. Feke, *AIChE Journal* **39**(2), 197-206 (1993).

Z.I. Mandralis, D.L. Feke, *Chemical Engineering Science* **48**(23), 3897-3905 (1993).

Z.I. Mandralis, W. Bolek, W. Burger, E. Benes, D.L. Feke, *Ultrasonics* **32**(2), 113-121, (1994).

G. Pangu, M.S. Thesis, Case Western Reserve University (2003).

S. Radel, A.J. McLoughlin, L. Gheradini, O. Doblhoff-Dier, E. Benes, *Ultrasonics* **38**, 633 (2000).

T.D. Rossing, N.H. Fletcher, *Principles of Vibration and Sound*, Springer-Verlag, New York (1995).

D. Rusinko, M.S. Thesis, Case Western Reserve University (2001).

S.E. Schwarz, W.G. Oldham, *Electrical Engineering: An Introduction*, Oxford University Press, New York (1993).

T.L. Tolt, D. L. Feke, *Proc. I.E.C.E.C.* **4**, 327 (1988).

T.L. Tolt, D.L. Feke, *Journal of the Acoustical Society of America* **91**(6), 3152 (1992).

T.L. Tolt, D.L. Feke, *Chemical Engineering Science* **48**, 527-540 (1993).

M. Van Dyke, *Perturbation Methods in Fluid Mechanics*, Parabolic Press, Stanford, California (1975).

W. Viessman, Jr., M.J. Hammer, *Water Supply and Pollution Control*, Harper Collins, New York (1993).

G. Whitworth, M.A. Grundy, W.T. Coakley, *Ultrasonics* **29**, 439 (1991).

K. Yasuda, *Sensors and Actuators B-Chemical* **64**(1-3), 128 (2000).

K. Yasuda, S.S. Haupt, S. Umemura, T. Yagi, M. Nishida, Y. Shibata, *J. of Acoust. Soc. Am.* **102**(1), 642 (1997).

R. Yosioka, G Kawasima, *Acoustica,* **5**, 167 (1955).